Hypoplastic modelling of grain stiffness degradation in granular material

Zur Erlangung des akademischen Grades eines
Doktors der technischen Wissenschaften
ausgeführte Dissertation

eingereicht an der
Fakultät für Bauingenieurwissenschaften
der Technischen Universität Graz

von

Linke Li

Berichter: ao.Univ.Prof. Dr.-Ing. Erich Bauer
Univ.Prof. Dr.-Ing. Wei Wu

Graz, December 2018

Affidavit

I declare that I have authored this thesis independently, that I have not used other than the declared sources/resources, and that I have explicitly indicated all material which has been quoted either literally or by content from the sources used. The text document uploaded to TUGRAZonline is identical to the present doctoral thesis.

07. 12. 2018

Date

Signature

Eidesstattliche Erklärung

Ich erkläre an Eides statt, dass ich die vorliegende Arbeit selbstständig verfasst, andere als die angegebenen Quellen/Hilfsmittel nicht benutzt, und die den benutzten Quellen wörtlich und inhaltlich entnommenen Stellen als solche kenntlich gemacht habe. Das in TUGRAZonline hochgeladene Textdokument ist mit der vorliegenden Dissertation identisch.

07. 12. 2018

Datum

Unterschrift

Acknowledgements

This work is done during my staying in the Institute of Applied Mechanics of the Technical University of Graz. This research was funded by the Chinese Scholarship Council(CSC).

I wish to express my deepest thanks to Ao.Univ.-Prof. Dipl.-Ing. Dr.techn. Erich Bauer, the supervisor of my PhD study, for his enthusiastic introduction to the research work related to hypoplasticity, for numerous fruitful discussions with him and for his generous helping over the last years.

Besides my supervisor, my special appreciation goes to Univ.-Prof. Dr.-Ing. Wei Wu for his important and useful feedback. I also thank Ms. Jingxiu Wang and other friends from the Institute of Geotechnical Engineering of the University of Natural Resources and Life Sciences, for their kind support during my study.

I would like to express my sincere appreciation to Ass.Prof. Carlos Ovalle from the Pontifical Catholic University of Chile for providing laboratory test results and valuable discussions.

I would like to thank Univ.-Prof. Dipl.-Ing. Dr. Dimitrios Kolymbas, Sarah-Jane Loretz-Theodorine, Dr. Barbara Schneider-Muntau, Dr. Gertraud Medicus and other colleagues from the University of Innsbruck.

I also thank Univ.-Prof. Dr.-Ing. Martin Schanz, Ass.Prof. Dipl.-Ing. Dr.techn. Helmut Knoblauch, Ao.Univ.-Prof. Dipl.-Ing. Dr.techn. M.Sc. tit.Univ.-Prof. Helmut Schweiger, Ass.Prof. Dipl.-Ing. Dr.techn. Evelyn Krall, Oberrat Dipl.-Ing. Otto Leibniz, for providing support during my staying in Graz.

To my lovely colleagues from the Institute of Applied Mechanics of the Technical University of Graz, Evelyn Feyertag, Ao.Univ.-Prof. Dipl.-Ing. Dr.techn. Peter Dietmaier, Relindis Rott, Anita Haider, Dominks Pölz, Mohammadkeya Khosravi, Saeed Safikhani, Michael Leitner and Benjamin Gotthardt, thank you very much for the pleasant working atmosphere.

Last but not the least, special thanks to my family: my parents, my brother and my son Alexander, for their spiritual support throughout the time of my study. My deepest appreciation to my wife Huizi, for the invaluable personal support!

Abstract

For granular materials like sand, gravel and rockfills the incremental stiffness is not a material constant and mainly depends on the current void ratio, stress state, friction angle, loading history and strain rate. Under high stresses grain breakage takes place which may also have an effect on the mechanical response. For coarse-grained and moisture sensitive materials, the incremental stiffness can also be influenced by the change of moisture content, i.e. the incremental stiffness decreases for the wet material. The degradation of the strength of the grains is a complex phenomenon which is affected by different factors, e.g. composition of minerals, state of weathering, and the hydro-chemical reaction of the stressed material. The stiffness degradation of the grain skeleton is a time-dependent process. For modelling the stiffness degradation a hypoplastic constitutive model by Bauer is considered. In this thesis the number of the constitutive parameters required is reduced which is convenient for practical application. This so-called simplified model has only 9 parameters to model the behaviour of a moisture sensitive material for a wide range of pressures under both dry and wet states.

First, some well-known compression relations are analysed and compared with the compression relation by Bauer. Second, the consistency condition for the implementation of the compression relation into the proposed hypoplastic constitutive model is derived. Third, the calibration equations of the simplified model are outlined. For highly nonlinear constitutive equations, the calibration of the parameters is from mathematical point of view an inverse problem and usually a challenging task. To demonstrate the performance of the model a special case study of the parameter determination for a shale quartzite sand is carried out. In particular, the experimental data by C. Ovalle are used. For applying a direct calibration procedure, however, some essential data are missing or only available for a rather small range of pressures. It is shown in this thesis that with a special calibration strategy the missing parameters can be determined. The comparison of the experimental data with the numerical results indicates that the calibration procedure proposed also permits a good estimation of the parameters from the reduced set of experimental data. It is also demonstrated that the simplified hypoplastic model can simulate the stiffness degradation of the material under different loading conditions.

Zusammenfassung

Bei körnigen Materialien wie Sand, Kies und Steinschüttungen ist die inkrementelle Steifigkeit keine Materialkonstante und hängt hauptsächlich von der aktuellen Porenzahl, dem Spannungszustand, dem Reibungswinkel, der Belastungsgeschichte und der aktuellen Deformationsgeschwindigkeit ab. Unter hohen Drücken kann der Bruch von Körnern die mechanischen Eigenschaften beeinflussen. Bei grobkörnigen und feuchtigkeitsempfindlichen Materialien kann die inkrementelle Steifigkeit auch durch eine Änderung des Feuchtigkeitsgehalts beeinflusst werden. In diesem Fall ist die inkrementelle Steifigkeit für das feuchte Material kleiner. Die Festigkeitsabnahme der Körner ist ein komplexes Phänomen, das durch verschiedene Faktoren wie zum Beispiel der Zusammensetzung der Mineralien, dem Verwitterungszustand und der hydrochemische Reaktion des Materials beeinflusst wird. Die Steifigkeitsabnahme vom Korngerüst ist ein zeitabhängiger Prozess. Zur Modellierung des Steifigkeitsabhahme wird ein hypoplastisches konstitutives Modell von Bauer betrachtet. In dieser Arbeit wird die Anzahl der erforderlichen konstitutiven Parameter reduziert, was auch einen Vorteile für die praktische Anwendung bedeutet. Dieses sogenannte vereinfachte Modell hat nur 9 Parameter, um das Verhalten eines feuchtigkeitsempfindlichen Materials für einen weiten Bereich von Drücken sowohl im trockenen als auch im feuchten Zustand zu modellieren.

Zunächst werden einige bekannte Kompressionsgesetze analysiert und mit dem Kompressionsgesetz von Bauer verglichen. Die Konsistenzbedingung für die Implementierung der Kompressionsbeziehung in das vorgeschlagene hypoplastische konstitutive Modell wird hergeleitet. Und die Kalibrierungsgleichungen des vereinfachten Modells formuliert. Für ausgeprägt nichtlineare konstitutive Gleichungen ist die Kalibrierung der Parameter aus mathematischer Sicht ein inverses Problem und häufig eine herausfordernde Aufgabe. Um die Leistungsfähigkeit des Modells zu demonstrieren, wird eine spezielle Fallstudie der Parameterbestimmung für einen Schiefer Quarzit Sand durchgeführt. Hierzu werden die experimentellen Daten von C. Ovalle verwendet. Für die Anwendung einer direkten Kalibrierung fehlen jedoch wesentliche Daten oder sind nur für einen relativ kleinen Druckbereich verfügbar. In dieser Arbeit wird gezeigt, dass mit einer speziellen Kalibrierungsstrategie die fehlenden Parameter bestimmt werden können. Der Vergleich der experimentellen Daten mit den numerischen Ergebnissen zeigt, dass mit dem vorgeschlagenen Kalibrierungsverfahren die Parameter auch aus dem eingeschränkten Datensatz gut abgeschätzt werden können. Es wird auch gezeigt, dass das vereinfachte hypoplastische Modell die Steifigkeitsabnahme des Materials unter verschiedenen Belastungsbedingungen simulieren kann.

Contents

Notation

In this work, symbolic notations are considered for denoting tensors, with boldface letters. In particular, bold lower-case letters are used to denote first-order tensor (vector), bold upper-case fonts are used to represent second-order tensor. Bold calligraphy fonts are used to denote fourth-order tensors. Only the Cartesian co-ordinate system with the base vectors (e_i, $i = 1,2,3$) is concerned for index notation and matrix representation. Therefore, tensors can be represented in the following forms, e.g. Bauer [9]

$\mathbf{a}$	$=$	$a_i\,\mathbf{e}_i$	– first-order tensor
$\mathbf{A}$	$=$	$A_{ij}\,\mathbf{e}_i \otimes \mathbf{e}_j$	– second-order tensor
$\mathcal{A}$	$=$	$A_{ijkl}\,\mathbf{e}_i \otimes \mathbf{e}_j \otimes \mathbf{e}_k \otimes \mathbf{e}_l$	– fourth-order tensor
$[\mathbf{a}]$			– matrix representation of vector $\mathbf{a}$
$[\mathbf{A}]$			– matrix representation of tensor $\mathbf{A}$

The main operation symbols used are:

$\cdot$	– dot product (or scalar product or inner product)
$\times$	– cross product (or vector product)
$\otimes$	– dyad of vectors
$:$	– double contraction of two tensors

Then, the main operations used are:

$\mathbf{a} \cdot \mathbf{b}$	$=$	$a_i\,b_i$
$\mathbf{a} \otimes \mathbf{b}$	$=$	$a_i\,b_i\,\mathbf{e}_i \otimes \mathbf{e}_j$
$\mathbf{A} \cdot \mathbf{b}$	$=$	$A_{ij}\,b_j\,\mathbf{e}_i$
$\mathbf{A} \cdot \mathbf{B}$	$=$	$A_{ij}\,B_{jl}\,\mathbf{e}_i \otimes \mathbf{e}_l$
$\mathbf{A} : \mathbf{B}$	$=$	$A_{ij}\,B_{ij}$
$\mathcal{A} : \mathbf{B}$	$=$	$A_{ijkl}\,B_{ij}\,\mathbf{e}_i \otimes \mathbf{e}_j$

List of standard notations:

δ_{ij}	the Kronecker delta
$\mathbf{I}$	second-order unit tensor
$\mathbf{x}$	current configuration for a material particle, $\mathbf{x} = x_i \mathbf{e}_i$
$\mathbf{X}$	reference configuration for a material particle, $\mathbf{X} = X_i \mathbf{e}_i$
$\mathbf{u}$	displacement of a material particle, $\mathbf{u} = \mathbf{x} - \mathbf{X}$
$\dot{\mathbf{u}}$	velocity of a material particle, $\dot{\mathbf{u}} = du/dt$
$\mathbf{F}$	deformation gradient, $F_{ij} = \partial x_i / \partial X_j$
$\mathbf{L}$	velocity gradient, $L_{ij} = \partial \dot{u}_i / \partial x_j$
$\mathbf{D}$	stretching tensor, $\mathbf{D} = \left(\mathbf{L} + \mathbf{L}^T\right)/2$
$\mathrm{tr}(\cdot)$	trace of a tensor
$\boldsymbol{\epsilon}$	logarithmic strain tensor, compression negative
$\boldsymbol{\varepsilon}$	engineering strain tensor, compression positive
ϵ_v	logarithmic volumetric strain, compression negative
ε_v	engineering volumetric strain, compression positive
$\mathbf{W}$	spin tensor, $\mathbf{W} = \left(\mathbf{L} - \mathbf{L}^T\right)/2$
$\mathbf{T}$	stress tensor
$\dot{\mathbf{T}}$	time derivative of stress tensor
$\mathring{\mathbf{T}}$	Jaumann stress rate, $\mathring{\mathbf{T}} = \dot{\mathbf{T}} + \mathbf{TW} - \mathbf{WT}$
$\hat{\mathbf{T}}$	normalized stress tensor, $\hat{\mathbf{T}} = \mathbf{T}/\mathrm{tr}(\mathbf{T})$
$\mathbf{T}^*$	deviatoric stress tensor, $\mathbf{T}^* = \mathbf{T} - \mathrm{tr}(\mathbf{T})/3$
$\hat{\mathbf{T}}^*$	normalized deviatoric stress tensor, $\hat{\mathbf{T}}^* = \hat{\mathbf{T}} - \mathbf{I}/3$
h_s	solid hardness of the grain skeleton
φ_{mob}	mobilized friction angle
φ_c	critical friction angle
φ_p	peak friction angle
p	mean stress, $p = -\mathrm{tr}(\mathbf{T})/3$
e	void ratio of a grain assembly
e_i	pressure dependent maximum void ratio for a granular media with grain contact
e_o	pressure dependent void ratio for a granular under ideal oedometric condition
e_c	pressure dependent critical void ratio of a grain assembly
e_d	pressure dependent minimum void ratio of a grain assembly
e_{i0}	maximum void ratio at stress free state, $p \approx 0$
e_{c0}	critical void ratio at stress free state, $p \approx 0$
e_{d0}	minimum void ratio at stress free state, $p \approx 0$
f_s	stiffness factor (Gudehus [22], Bauer [6])
f_d	density factor(Gudehus [22], Bauer [6])
$\check{f}_s$	stiffness factor of the simplified version proposed in this thesis
$\check{f}_d$	density factor of the simplified version proposed in this thesis
K_0	earth pressure coefficient at rest

1 Introduction

1.1 Motivation

Granular material is a matter in its own right. In different branches of engineering such as agricultural, soil and material science, the size of the grains can be extremely diverse. In soil mechanics, the granular materials are typically referred to as clay, sand, loess and rockfill, with particle sizes vary from micrometers to meters. Generally, the mineral composition, shape and surface roughness of the particles differ significantly from one material type to another. Although with different properties, these materials exhibit certain common features when it comes to their granular skeleton, i.e. a grain assembly with grain contacts and void space. The void space can either be empty or filled with fluids and gas. From experiments it is known that the mechanical behaviour also depends on the arrangement of the grains within the grain skeleton. Moreover for partly saturated soil the range of grain sizes may also have an influence on the amount of capillary forces. Especially in dam engineering, coarse-grained rockfills are frequently used where the effect of capillary forces can be neglected compared to the high forces at contact points. For weathered and moisture sensitive rockfills after wetting, additional densifications were observed, e.g. Howson [30], Sowers et al. [82], Holestöl et al. [29], Leonards and Altschaeffl [55], Kast et al. [39], Kast [38], Oldecop and Alonso [71] and Ovalle et al. [74].

Lee et al. [54] found that Antioch sand, which consisted of weathered particles, shows a significant susceptibility to crushing when wetted. Results of drained triaxial compression tests indicate that the moisture content has a strong effect on the strength and the volume change behaviour (Fig. 1.1a).

Nobari and Duncan [70] showed for a Pyramid material the influence of the moisture content on the stress-strain and volume behaviour (Fig. 1.1b). After wetting of an initially dry specimen, the vertical stress decreased significantly and with continuing vertical compression the stress-strain and volume change curves eventually closely approached the one of the initially wet specimen.

Jennings and Burland [35] reported about the effect of wetting of air dried silt specimen in oedometric compression tests: when the initially dry specimen was wetted under certain boundary conditions either an additional densification or stress relaxation takes place (Fig. 1.2).

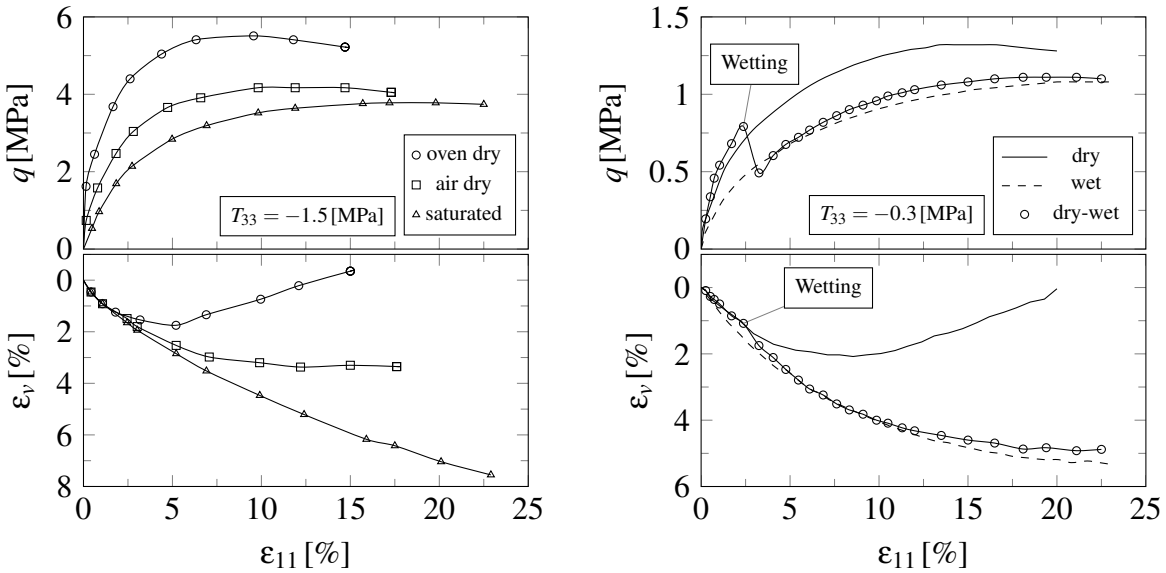

(a) Antioch sand (after Lee et al. [54])

(b) Pyramid material (after Nobari and Duncan [70])

Figure 1.1: Influence of moisture content and wetting effect on stress-strain behaviour and volume strain behaviour in triaxial tests

These additional densifications or settlements may have a significant importance for the long-term behaviour of geotechnical structures, e.g. Alonso and Cardoso [2]. The numerical simulation and theoretical investigation of stiffness degradation induced by wetting is a main aim of the present thesis. Herein the concept of the degradation of the solid hardness introduced by Bauer [8] is the basis for the developing of a simplified model in this work. In the course of this study, it is realized that for the case the experimental data available do not give all information required for a direct calibration, a special strategy must be developed to get the missing information. To this end a special calibration procedure is proposed to determine the parameters of the constitutive model considered.

1.2 Outline of the study

In this thesis, a reference model for wetting deformation developed by Bauer [8] is simplified to reduce the number of constitutive parameters. A specific calibration strategy is proposed to determine the constitutive parameters based on the experimental data by Ovalle [73] and Ovalle et al. [74]. The outline of this study is as follows:

In Chapter 2, the developments in hypoplasticity are briefly summarized and the reference equations used in this work are given.

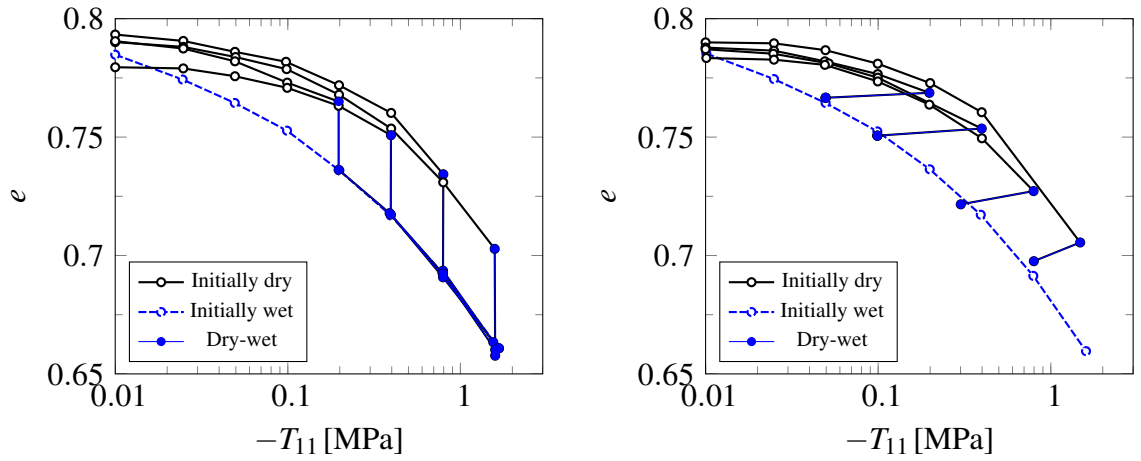

(a) Creep (b) Stress relaxation

Figure 1.2: Oedomteric compression of silt with different moisture contents: (a) influence of vertical stress on creep deformation after wetting; (b) stress relaxation after wetting. (Figures are slightly modified from Jennings and Burland [35].)

In Chapter 3, the properties of different compression laws are discussed in the light of experimental data. In particular the compression laws by Janbu (1963), Pestana (1995) and Bauer (1996) are analysed.

A simplified hypoplastic model for stiffness degradation is proposed in Chapter 4. In particular, the consistent implementation of compression relation by Bauer into the constitutive equation is given. The direct calibration procedure and constitutive equations for element tests are outlined for the case all experimental data required for determination of the constitutive constants are available.

For the case some essential data are not available, the direct calibration procedure cannot be applied. In order to overcome the deficiency, so-called special calibration strategy is proposed and applied to experimental data by Ovalle [73] and Ovalle et al. [74], which is in Chapter 5. Finally, the numerical results of element tests are compared with the experimental data.

2 Review of Hypoplasticity

2.1 Developments in Hypoplasticity

In soil mechanics, granular materials are often modelled using the framework of elasto-plasticity. Terms, like elastic and plastic behaviour, plastic potential, yield function, are used in elastic-plastic constitutive models. Another concept of constitutive modelling is based on hypoplasticity which was introduced in the 1970s by Kolymbas [40]. In the basic concept of hypoplasticity, a distinction between purely elastic and plastic parts is not needed, and a single incrementally nonlinear isotropic tensor function is sufficient to capture inelastic material properties. In a more enhanced model by Niemunis and Herle [69] a so called elastic strain is introduced.

Hypoplasticity is developed within the framework of rational mechanics [87]. In particular, in hypoplastic models, the objective stress rate $\mathring{\mathbf{T}}$ is described in the simplest form by a function of stretching tensor $\mathbf{D}$ and the stress tensor $\mathbf{T}$. In general, hypoplastic models can be written as the sum of a linear term $\mathcal{L}(\mathbf{T}) : \mathbf{D}$ and a nonlinear term $\mathbf{N}(\mathbf{T})\,\|\mathbf{D}\|$:

$$\mathring{\mathbf{T}} = \mathcal{L}(\mathbf{T}) : \mathbf{D} + \mathbf{N}(\mathbf{T})\,\|\mathbf{D}\| \tag{2.1}$$

Herein, $\mathcal{L}(\mathbf{T})$ denotes a fourth-order tensor function depending on $\mathbf{T}$, and $\mathbf{N}(\mathbf{T})$ stands for a second-order tensor function. The form of $\mathcal{L}(\mathbf{T})$ and $\mathbf{N}(\mathbf{T})$ should be confined according to the representation theorem by Wang [90] and general experimental findings. More details can be referred to Wu [95] and Wu and Bauer [97].

Kolymbas [41] proposed a hypoplastic constitutive model with four terms:

$$\mathring{\mathbf{T}} = \frac{c_1}{2}(\mathbf{TD} + \mathbf{DT}) + c_2\,\mathrm{tr}(\mathbf{TD})\mathbf{I} + c_3\mathbf{T}\|\mathbf{D}\| + c_4\frac{\mathbf{T}^2}{\mathrm{tr}\,\mathbf{T}}\|\mathbf{D}\| \tag{2.2}$$

where $c_i\,(i = 1, \cdots, 4)$ are dimensionless constants. $\|\mathbf{D}\|$ denotes the Euclidean norm of the stretching tensor, $\|\mathbf{D}\| = \sqrt{\mathrm{tr}\,\mathbf{D}^2}$.

Wu [95] introduced an improved version based on the Eq. (2.2):

$$\mathring{\mathbf{T}} = c_1\,(\mathrm{tr}\,\mathbf{T})\,\mathbf{D} + c_2\frac{\mathrm{tr}\,(\mathbf{TD})\,\mathbf{T}}{\mathrm{tr}\,\mathbf{T}} + c_3\frac{\mathbf{T}^2}{\mathrm{tr}\,\mathbf{T}}\|\mathbf{D}\| + c_4\frac{\mathbf{T}^{*2}}{\mathrm{tr}\,\mathbf{T}}\|\mathbf{D}\| \tag{2.3}$$

Herein, $\mathbf{T}^* = \mathbf{T} - \mathrm{tr}\,(\mathbf{T})\,\mathbf{I}/3$ is the deviatoric stress tensor.

Based on the Eq. (2.3), Tejchman and Wu [84] investigated the shear band formation in granular materials during biaxial compression tests; Wang [94] proposed an extended constitutive equation and implemented it in tunnelling simulation; Lin et al. [57] extended the model into a micropolar version for shear band simulation; Xu et al. [99] introduced an model for frozen soil; Guo et al. [25] proposed a constitutive model for debris flow materials and has been successfully implemented into the smoothed particle hydrodynamics code by Peng et al. [75]; Wang [91] and Wang et al. [93] proposed a unified model combining critical state hypoplastic model and a viscous model.

Wu and Bauer [96] extended Eq. (2.3) by taking into account pyknotropy which denotes the influence of density on the mechanical response [42, 43]

$$\mathring{\mathbf{T}} = \mathcal{L}(\mathbf{T}) : \mathbf{D} + \mathbf{N}(\mathbf{T}) \|\mathbf{D}\| I_e \tag{2.4}$$

Herein a density index I_e defined by

$$I_e = (1-a)\frac{e-e_d}{e_c-e_d} + a \tag{2.5}$$

In Eq. (2.5) the critical void ratio e_c and the minimum void ratio e_d are pressure dependent quantities and a is a constitutive parameter.

Gudehus [22] and Bauer [6] proposed a comprehensive hypoplastic model by incorporating barotropy and pyknotropy in a consistent way. The general form of the constitutive equation reads:

$$\mathring{\mathbf{T}} = f_s \left[\mathcal{L}\left(\hat{\mathbf{T}}\right) : \mathbf{D} + f_d \mathbf{N}\left(\hat{\mathbf{T}}\right) \|\mathbf{D}\| \right] \tag{2.6}$$

with the specific form

$$\mathring{\mathbf{T}} = f_b f_e \left\{ \left[a_1^2 \mathcal{I} + \left(\hat{\mathbf{T}} \otimes \hat{\mathbf{T}}\right) \right] : \mathbf{D} + f_d a_1 \left(\hat{\mathbf{T}} + \hat{\mathbf{T}}^*\right) \|\mathbf{D}\| \right\} \tag{2.7}$$

Herein, $\mathcal{I}$ stands for the fourth-order unit tensor, a_1 is a dimensionless scalar factor and related to the stress limit condition. $\hat{\mathbf{T}}$ is the normalized stress tensor, $\hat{\mathbf{T}} = \mathbf{T}/\operatorname{tr}\mathbf{T}$ and $\hat{\mathbf{T}}^*$ denotes the normalized deviatoric stress tensor, i.e. $\hat{\mathbf{T}}^* = \hat{\mathbf{T}} - \mathbf{I}/3$. f_b stands for barotropy factor, and f_e and f_d denote pyknotropy factors. The combination of f_b and f_e is called stiffness factor, i.e. $f_s = f_b f_e$.

The pyknotropy factor f_d is a function related to the current value of the void ratio e, the void ratios e_c, e_d and the material parameter α

$$f_d = \left(\frac{e-e_d}{e_c-e_d}\right)^{\alpha} \tag{2.8}$$

Another pyknotropy factor f_e reads:

$$f_e = \left(\frac{e_c}{e}\right)^{\beta} \tag{2.9}$$

with the material parameter β. The stiffness factor f_b can be derived by considering the consistency condition (Gudehus [22]).

The compression equation of maximum void ratio suggested by Bauer [6]

$$e_i = e_{i0} \exp\left\{-\left(\frac{3p}{h_s}\right)^n\right\} \tag{2.10}$$

is included in Eq. (2.6) and Eq. (2.7) in which $p = -\operatorname{tr}\mathbf{T}/3$ is the mean pressure. e_{i0} denotes the initial maximum void ratio at stress free state, $p = 0$. h_s is the so-called solid hardness and n is parameter related to the compression curve as outlined in Chapter 3.

Based on the compression equation for e_i, similar relations for e_c and e_d were postulated by Gudehus [22]:

$$\frac{e_i}{e_{i0}} = \frac{e_c}{e_{c0}} = \frac{e_d}{e_{d0}} = \exp\left\{-\left(\frac{3p}{h_s}\right)^n\right\} \tag{2.11}$$

herein e_{i0}, e_{c0} and e_{d0} are the initial values of the maximum void ratio, critical void ratio and minimum void ratio at stress free state.

von Wolffersdorff [89] proposed a slightly different version which includes the stress limit condition by Matsuoka-Nakai:

$$\mathring{\mathbf{T}} = f_b f_e f_s^* \left\{ \left[F^2\mathcal{I} + a^2\left(\hat{\mathbf{T}} \otimes \hat{\mathbf{T}}\right)\right] : \mathbf{D} + f_d a F \left(\hat{\mathbf{T}} + \hat{\mathbf{T}}^*\right) \|\mathbf{D}\| \right\} \tag{2.12}$$

Compared to the model by Gudehus [22] and Bauer [6], Eq. (2.12) takes into account an additional part $f_s^* = 1/\operatorname{tr}\left(\hat{\mathbf{T}}^2\right)$. Factor a is dimensionless and related to critical friction angle. F is a function of normalized deviatoric stress $\hat{\mathbf{T}}^*$. Note that here the factor f_b is different from the one in Eq. (2.7). A more sophisticated model was developed by Niemunis and Herle [69], using so-called inter-granular strain concept, to take into account for instance the history of cyclic loading. Based on the work by von Wolffersdorff, Herle and Kolymbas [28] proposed a model for soils with low friction angles. Considering the work of Herle and Kolymbas [28], Mašín [59] proposed a model for clays.

In 2000 Bauer [7] embedded Casagrande's critical states and factor f_s^* proposed by von Wolffersdorff [89] into Eq. (2.6). The extended equation can be written as:

$$\mathring{\mathbf{T}} = f_b f_e f_s^* \left\{ \left[\hat{a}^2\mathcal{I} + \left(\hat{\mathbf{T}} \otimes \hat{\mathbf{T}}\right)\right] : \mathbf{D} + f_d \hat{a} \left(\hat{\mathbf{T}} + \hat{\mathbf{T}}^*\right) \|\mathbf{D}\| \right\} \tag{2.13}$$

For simulation of shear bands using finite element method, Tejchman and Bauer [83] proposed a micro-polar hypoplastic constitutive model. Huang [31] implemented the micro-polar model into Finite Element code Abaqus. More enhanced versions of the micro-polar model can be found by Huang et al. [32]. Bauer [10] extended the model to take into account the influence of the loading path on grain crushing.

Kolymbas [45] proposed a constitutive model called *Barodesy*, which can be considered as an alternative development of hypoplasticity. The general equation of barodesy reads:

$$\dot{\mathbf{T}} = \|\mathbf{T}\| \cdot \left(a_1 \mathbf{R} + a_2 \hat{\mathbf{T}}\right) \cdot \|\mathbf{D}\| \tag{2.14}$$

Herein, function $\mathbf{R}$ is derived from two rules by Goldscheider [21] which are related to the asymptotic behaviour of proportional loading paths.

$$\mathbf{R} = \mathrm{tr}\hat{\mathbf{D}}\mathbf{I} + c_1 \exp\left(c_2 \hat{\mathbf{D}}\right) \tag{2.15}$$

Moreover, $\mathbf{R}$ is the direction tensor, which has the direction of the asymptotic stress path in the stress space associated to $\hat{\mathbf{D}} = \mathbf{D}/\|\mathbf{D}\|$. c_1, c_2, a_1 and a_2 are material parameters. Kolymbas [46] suggested a general barodetic equation by modifying Eq. (2.14) into

$$\dot{\mathbf{T}} = h\left(f\hat{\mathbf{R}} + g\hat{\mathbf{T}}\right)\|\mathbf{D}\| \tag{2.16}$$

with $h = c_3\|\mathbf{T}\|^{c_4}$. f and g are scalar functions which take into account critical states, barotropy and pyknotropy. It is suggested to use different functions of f and g for different materials such as sand and clay. Latter, a barodetic model for clay is also proposed by Medicus et al. [62]. More details can be referred to Medicus [61].

Since the concept of hypoplastic models was introduced in 1970s, a great number of different versions were proposed. For more details about developments in hypoplasticity, one can refer to Kolymbas [44], Wu and Kolymbas [98], Kolymbas [46] and Kolymbas and Medicus [48].

2.2 Reference model for stiffness degradation

For developing the simplified model for stiffness degradation in Chapter 4 a reference model by Bauer [8] is used, which is outlined in the following.

The stiffness degradation induced by wetting or weathering can be described as a time-dependent process. The key parameter h_s which is related to the stiffness factor f_s in the hypoplastic model proposed by Gudehus [22] and Bauer [6] was extended into a time-dependent quantity to take into account the time dependent process of stiffness degradation.

For modelling wetting induced degradation of the incremental stiffness, a time dependent reduction of the solid hardness was proposed by Bauer [8]

$$h_{st} = h_{sw} + (h_{sd} - h_{sw}) \exp\left\{-\frac{t}{c}\right\} \tag{2.17}$$

Herein, the h_{sd} and h_{sw} are the solid hardness for the dry and wet grain skeleton, respectively. Parameter c is a constant with the dimension of time. The parameter h_s in Eq. (2.10)

is replaced by the time dependent quantity h_{st} in Eq. (2.17). Thus the enhanced compression law reads:

$$e_i = e_{i0} \exp\left\{-\left(\frac{3p}{h_{st}}\right)^n\right\} \tag{2.18}$$

Bauer [8] extended Eq. (2.13) with an additional term depending on mean pressure and deviatoric stress

$$\mathring{\mathbf{T}} = f_s\left\{\hat{a}^2\mathbf{D} + \mathrm{tr}\left(\hat{\mathbf{T}}\mathbf{D}\right)\hat{\mathbf{T}} + f_d\hat{a}\left(\hat{\mathbf{T}} + \hat{\mathbf{T}}^*\right)\|\mathbf{D}\|\right\} + \frac{\dot{h}_{st}}{h_{st}}\left\{\frac{1}{3}\mathrm{tr}\left(\mathbf{T}\right)\mathbf{I} + \kappa\mathbf{T}^*\right\} \tag{2.19}$$

In the additional term in Eq. (2.19), the scalar κ controls the effects of deviatoric stress on the volume strain behaviour as also discussed in Bauer et al. [11]. Function $\hat{a}$ is related to the stress limitation condition with respect to the critical friction angle φ_c, the Lode angle θ and the components of normalized stress deviator $\hat{\mathbf{T}}^*$, the form discussed by Bauer [7] reads:

$$\hat{a} = \frac{\sin\varphi_c}{3-\sin\varphi_c}\left\{\sqrt{\frac{8/3 - 3\|\hat{\mathbf{T}}^*\|^2 + \sqrt{3/2}\|\hat{\mathbf{T}}^*\|^3\cos 3\theta}{1+\sqrt{3/2}\|\hat{\mathbf{T}}^*\|\cos 3\theta}} - \|\hat{\mathbf{T}}^*\|\right\} \tag{2.20}$$

with

$$\|\hat{\mathbf{T}}^*\| = \sqrt{\mathrm{tr}\left(\hat{\mathbf{T}}^{*2}\right)} \tag{2.21}$$

and

$$\cos 3\theta = -\frac{\sqrt{6}\,\mathrm{tr}\left(\hat{\mathbf{T}}^{*3}\right)}{\mathrm{tr}^3\left(\hat{\mathbf{T}}^{*2}\right)^{3/2}} \tag{2.22}$$

For isotropic states, Eq. (2.20) for $\hat{a}$ reduces to $\hat{a}_i$:

$$\hat{a}_i = \sqrt{\frac{8}{3}}\frac{\sin\varphi_c}{3-\sin\varphi_c}. \tag{2.23}$$

According to the postulation by Gudehus [22], the minimum limit void ratio e_d and the critical void ratio have the same pressure dependency as the maximum limit void ratio e_i

$$\frac{e_i}{e_{i0}} = \frac{e_c}{e_{c0}} = \frac{e_d}{e_{d0}} = \exp\left\{-\left(\frac{3p}{h_{st}}\right)^n\right\} \tag{2.24}$$

In contrast to the constitutive model by Gudehus [22] and Bauer [6], the stiffness factor in Eq. (2.19) also includes the term f_s^* proposed by von Wolffersdorff [89]. Factor f_s reads

$$f_s = f_e f_b f_s^* \tag{2.25}$$

A brief summary of some samples of parameter set related to the reference equations is tabulated in Table 2.1.

Table 2.1: Parameter sets of reference equations

Material	φ_c	h_{sd}	h_{sw}	n	e_{i0}	e_{c0}	e_{d0}	α	β	c	κ
	[°]	[MPa]	[MPa]	[-]	[-]	[-]	[-]	[-]	[-]	[d]	[-]
Granite [8]	42	75	25.5	0.6	0.85	0.39	0.2	0.125	1.05	12	0
Gravel sand [20]	35.5	95	30	0.45	0.81	0.62	0.37	0.2	1.05	3	/
Sandstone [11]	40	47	11.5	0.3	0.59	0.48	0.2	0.18	2.5	3	0.7

3 Compression behaviour, limit void ratios and critical void ratio

In this chapter the modelling of the compression behaviour of granular materials is investigated for different compression laws frequently used in soil mechanics.

3.1 Behaviour of unweathered materials

In soil mechanics, granular materials are often represented as continuous media. This continuous description includes solid particles and the voids, which can be filled with fluids and gases (Fig. 3.1).

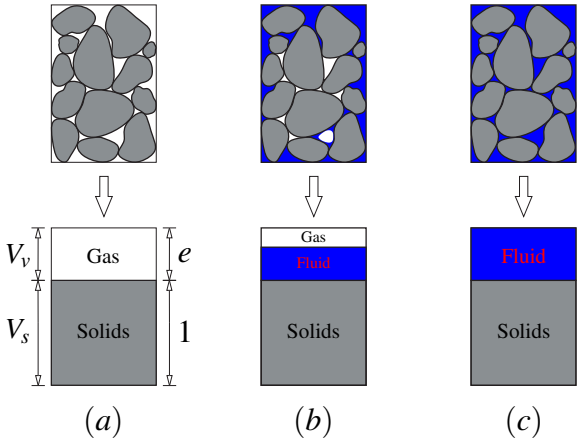

Figure 3.1: Discrete structure of granular materials and corresponding continuum description

A granular body with a total volume, V, consists of the volume of solids, V_s, and the volume of voids, V_v. The ratio of the volume of voids to the volume of solids is called void ratio, $e = V_v/V_s$. For the unit volume of solids, the volume of the granular body is the so-called specific volume, $1+e$. Two assumptions in conventional soil mechanics are still taken into account:

- Solids[1] is incompressible

[1] In soil mechanics, the solids are referred to soil particles.

- Granular body can be considered as a continuum[2]

Therefore, the change of total volume of the granular body is only related to the change of the void ratio. In continuum mechanics, the relation between void ratio and volume strain, ϵ_v, can be derived from, e.g., Gudehus [22]

$$\dot{e} = (1+e)\,\mathrm{tr}\mathbf{D} \tag{3.1}$$

with the stretching rate $\mathbf{D} = \left(\mathbf{L}+\mathbf{L}^T\right)/2$. $\mathbf{L}$ stands for the velocity gradient. Eq. (3.1) yields:

$$1+e = (1+e_0)\exp(\epsilon_v) \tag{3.2}$$

herein e_0 represents the initial void ratio at reference configuration where the volume strain equals to zero. Eq. (3.2) shows that void ratio is a quantity which takes into account the influence of the initial void ratio, e_0, on the volume change. This is the reason that void ratio is preferred to describe the volume change in this study. More specific, most *volume strain–stress* relations are presented in the *void ratio–stress* space, i.e. *e-p* diagram.

3.1.1 Experimental results obtained under isotropic compression

Under isotropic compression the volume of the grain skeleton reduces with increase in mean pressure (Fig. 3.2). The main factors affecting the compressibility of granular bodies are determined by two aspects, namely the grain size distribution of material and the structure of the grain skeleton. Under certain pressure level grain crushing takes place which is strongly related to the strength of particles and grain size distribution. Different materials exhibit different compressibilities. Normally consolidated peat (Fig. 3.2b) is softer than consolidated clay (Fig. 3.2a), and consolidated clay is softer than sand. Even for the samples with same material, the compressibilities can be different because of the different initial void ratios.

3.1.2 Experimental results obtained under oedometric compression

Similar compression behaviour of granular material can be observed from oedometric compression experiments. As shown in Fig. 3.4 the oedometric compression curves of different sands have similar shape as the isotropic compression curves showed in Fig. 3.3a. Under monotonic loading condition, the void ratio decreases as the vertical stress increasing. With the developing of vertical stress, the influence of initial density on the compression curve becomes less and the compression curves starting from different initial densities approach to a unique one. After reached a certain stress level, the effect of initial density almost vanishes.

[2]Note that the continuum here refers to the simple grain skeleton.

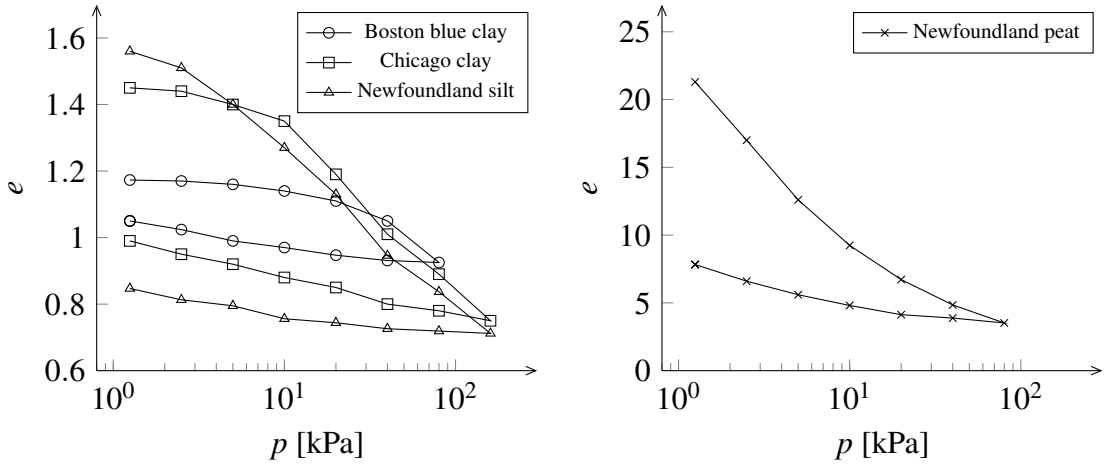

Figure 3.2: Compressibility of various soils in semi-logarithmic diagram (after Butterfield [15])

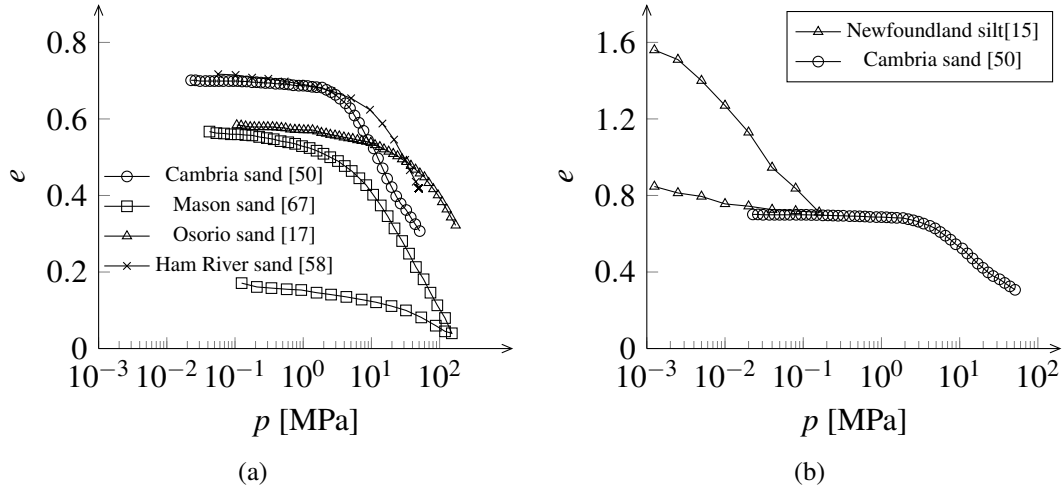

Figure 3.3: Compressibility of sands and silt under isotropic compression tests

3.1.3 Limit void ratios

Due to different particle size distribution, different possible void ratio ranges are possible. An example of granular assemblies of 2-D idealized particles is illustrated in Fig. 3.5.

In particular Fig. 3.5a shows the loosest state of the idealized 2-D particles, Fig. 3.5b for the densest state. The Fig. 3.5c illustrate a packing of honeycomb state and the granulate flow state is illustrated in Fig. 3.5d. Moreover, the honeycomb state with large macro voids is rather unstable and also granular flow state are not within the scope of this study.

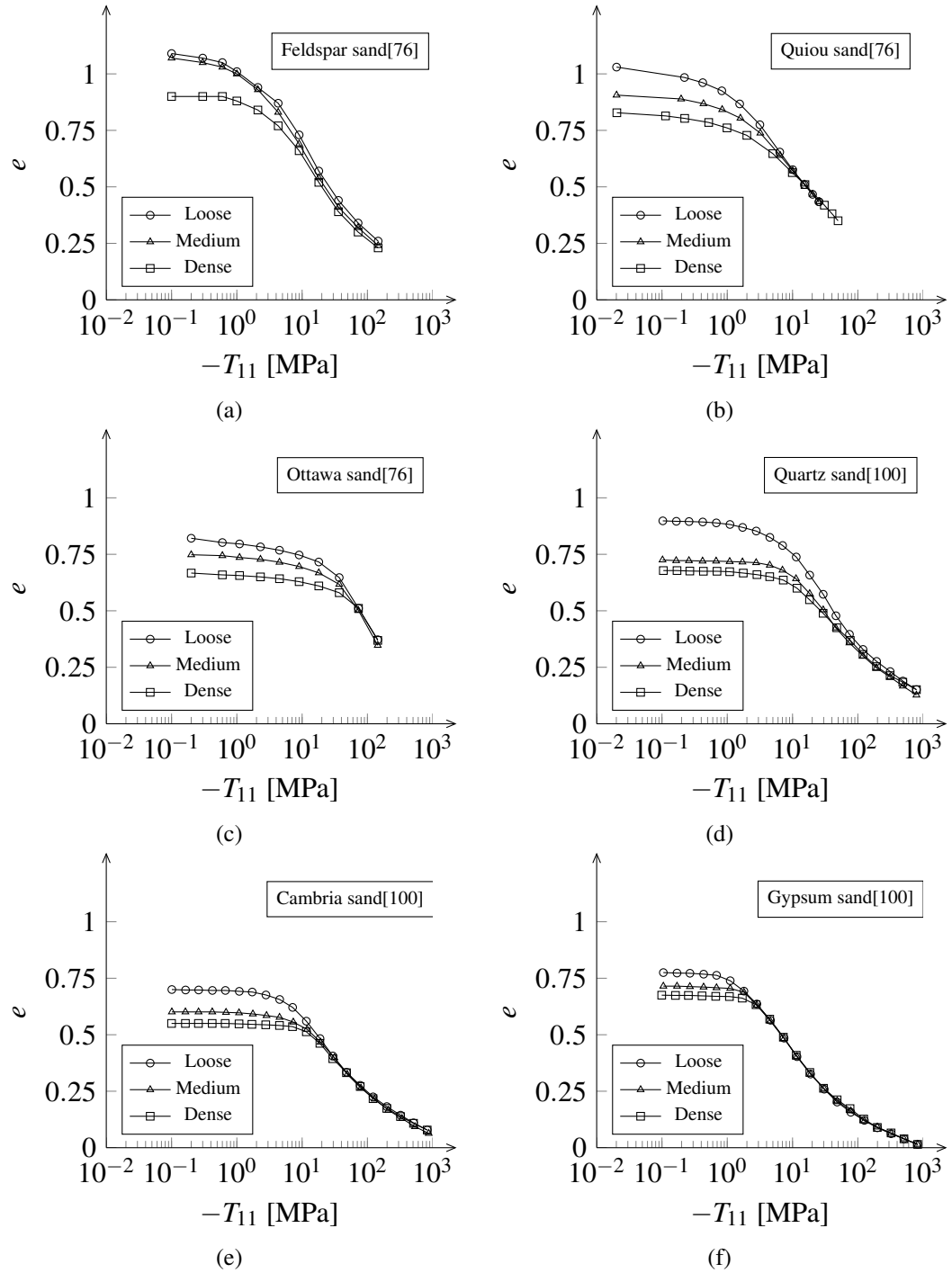

Figure 3.4: Compressibility of sands from high pressure oedometric compression tests

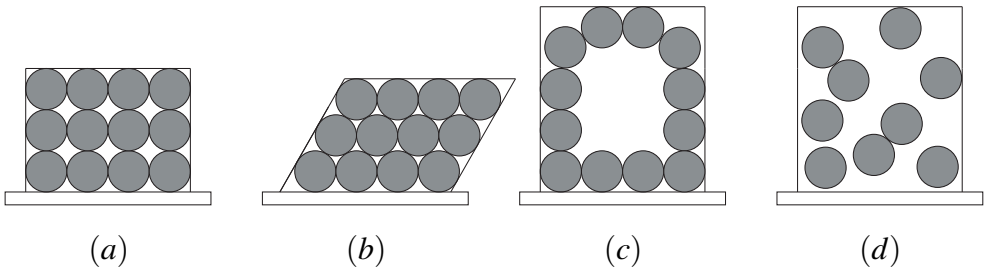

Figure 3.5: Idealized 2-D particles under different states: (a) loosest state; (b) densest state; (c) honeycomb state; (d) granulate flow state.

Considering the possible range of pressure dependent void ratios, Gudehus [22] suggested that the possible rang should be bounded by the limit void ratios, e_i and e_d (Fig. 3.6):

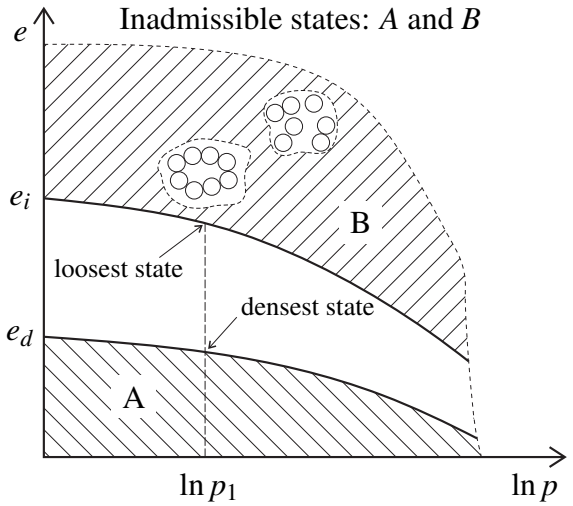

Figure 3.6: Limit void ratios: e_i maximum void ratio, e_d minimum void ratio

The maximum void ratio, e_i, can only be reached in so-called ideal isotropic compression. In particular, the ideal isotropic compression starts with the loosest grain skeleton, $e = e_{i0}$, at stress free state, $p_0 = 0$. The loosest state of a dry material can not be reached in conventional laboratory because of the gravity. Therefore the void ratio at stress free state, e_{i0}, cannot be determined experimentally. However, the concept of maximum limit void ratio indeed has physical meaning and provides a reference for relative density. In order to ensure the specimen as loose as possible, Ishihara [33] suggested adding a small amount of humidity into specimen. Note that this is only appropriate for relative coarse material, like sand and rockfills. For the relative fine material, i.e. peat, silt and clay, the moist appearance will induce suction which cannot lead to the loosest grain skeleton.

3.1.4 Compression laws of unweathered materials

Terzaghi [85] fitted the primary compression data of clay by a line of equation:

$$e = e_0 - C_c \log_{10}\left(\frac{\sigma'}{\sigma'_0}\right) \tag{3.3}$$

in which e_0 denotes the reference void ratio at the reference stress σ'_0 state. C_c is the so-called compression index. Eq. (3.3) can also be represented as a function of the mean pressure $p = -\operatorname{tr}\mathbf{T}/3$

$$e_i - e_{ir} = -\lambda \ln\left(\frac{p}{p_r}\right) \tag{3.4}$$

Herein, e_i denotes the pressure dependent maximum void ratio and e_{ir} is the reference void ratio related to p_r. For clay $e_i(p)$ is the so-called normal consolidation line in a semi-logarithmic representation in Fig. 3.7 (Terzaghi [85], Roscoe et al. [78] and Schofield and Wroth [81]). In the Cam clay model the pressure dependent critical void ratio e_c is assumed to be parallel to e_i in e-$\ln(p)$ space as illustrated in Fig. 3.7b.

$$e_i - e_{ir} = e_c - e_{cr} = -\lambda \ln(p/p_r) \tag{3.5}$$

This concept is widely used in many models, i.e., Muir Wood [65], Fig. 3.7.

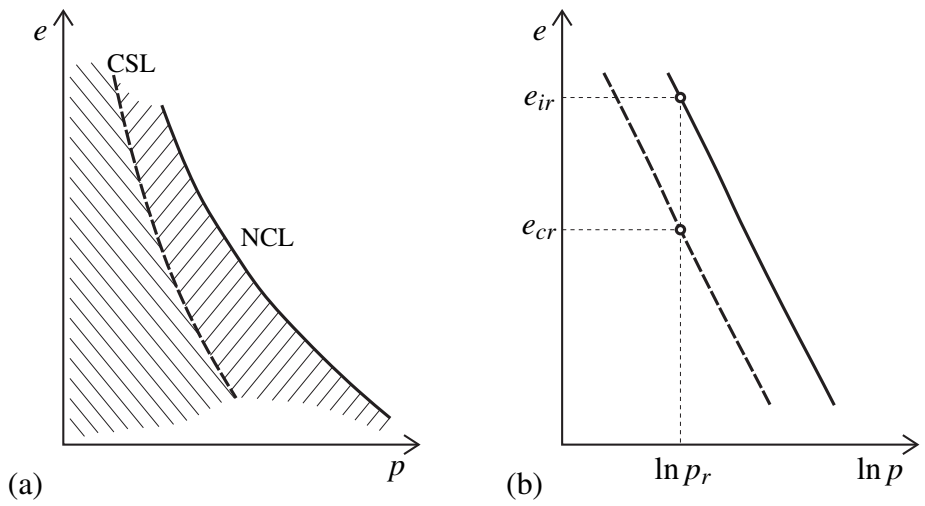

Figure 3.7: Limit state lines: (a) e-p representation, slightly modified from Muir Wood [65]; (b) e-$\ln p$ representation.

Been et al. [14] assumed a bilinear relation for the critical state line of Erksak sand and Leighton Buzzard sand (Fig. 3.8a).

Based on the results of compression experiments with Karlsruhe sand, Bauer [6] proposed a compression equation for the maximum void ratio e_i

$$e_i = e_{i0} \exp\left[-\left(\frac{3p}{h_s}\right)^n\right] \tag{3.6}$$

here e_i denotes the maximum void ratio of a grain skeleton at a mean stress p. In other words, e_i denotes the pressure dependent void ratio starting from the loosest state of the grain skeleton.

Gudehus [22] postulate that the limit void ratios e_i and e_d as well as the critical void ratio e_c follow the equation proposed by Bauer [6]:

$$\frac{e_i}{e_{i0}} = \frac{e_c}{e_{c0}} = \frac{e_d}{e_{d0}} = \exp\left[-\left(\frac{3p}{h_s}\right)^n\right] \tag{3.7}$$

With the postulation by Gudehus [22], the limit void ratio curves are consistent within the whole pressure range as illustrated in Fig. 3.8b.

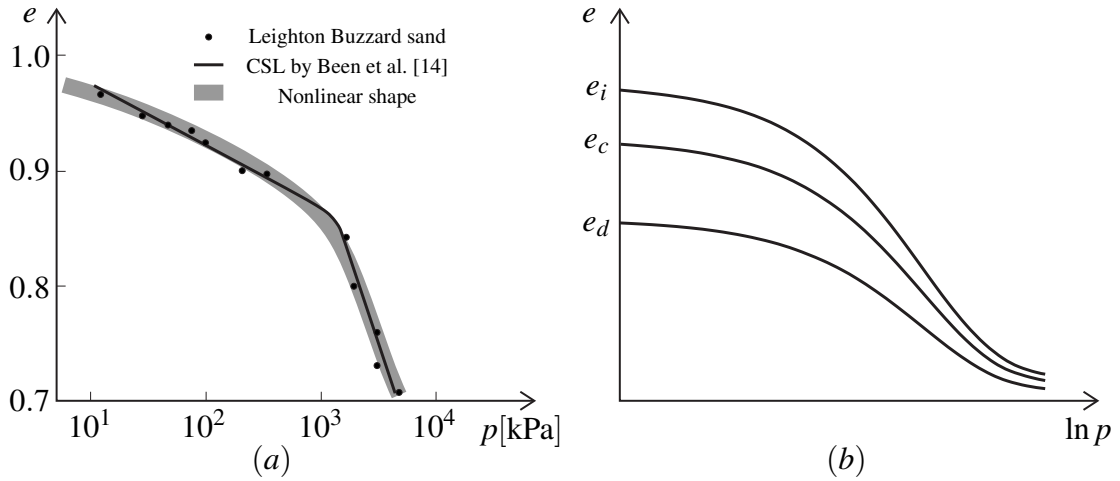

Figure 3.8: Nonlinear limit state lines: (a) bilinear e-$\ln p$ for sand assumed by Been et al. [14]; (b) limit state lines postulated by Gudehus [22] according to the compression law Bauer [6].

Compression law by Janbu, 1963

The incremental stiffness in oedometric compression is defined by the following relation between the stress rate, $\dot{T}_{11}$, and the strain rate, D_{11}:

$$E_s = \frac{\dot{T}_{11}}{D_{11}} \tag{3.8}$$

Janbu (1963) suggested a power law to describe the relation between incremental stiffness and vertical stress in oedometric compression:

$$\frac{E_s}{-T_{ref}} = \chi \left(\frac{T_{11}}{T_{ref}} \right)^{\alpha} \tag{3.9}$$

herein T_{ref} denotes a reference stress, χ the modulus factor and α the stiffness exponent are material parameters depend on material types. By substitute $E_s = \dot{T}_{11}/D_{11}$ into Eq. (3.9) one obtains the following rate form equation:

$$\dot{T}_{11} = -\chi T_{ref} \left(\frac{T_{11}}{T_{ref}} \right)^{\alpha} D_{11} \tag{3.10}$$

For a value of $\alpha = 1$, Eq. (3.10) reduces to

$$\dot{T}_{11} = -\chi T_{11} D_{11} \tag{3.11}$$

Considering Eq. (3.1) for oedometric compression, i.e. $\mathrm{tr}\mathbf{D} = D_{11}$, Eq. (3.11) can be represented as

$$\frac{\dot{T}_{11}}{T_{11}} = -\chi \frac{\dot{e}}{1+e} \tag{3.12}$$

With the initial condition that $T_{11} = T_{11,0} < 0$ and $e = e_0$, the integration of Eq. (3.12) yields:

$$\ln\left(\frac{1+e}{1+e_0} \right) = -\frac{1}{\chi} \ln\left(\frac{T_{11}}{T_{11,0}} \right) \tag{3.13}$$

or

$$\ln(1+e) = -\frac{\ln(-T_{11})}{\chi} + \frac{\ln(-T_{11,0})}{\chi} + \ln(1+e_0) \tag{3.14}$$

This represents a linear relation between $\ln(-T_{11})$ and $\ln(1+e)$. Taking into account the lateral stress coefficient, $K_0 = T_{22}/T_{11}$, Eq. (3.14) can be written as:

$$\ln(1+e) = -\frac{\ln(3p)}{\chi} + \frac{\ln(1+2K_0)}{\chi} + \frac{\ln(-T_{11,0})}{\chi} + \ln(1+e_0) \tag{3.15}$$

As mentioned in Muir Wood [66] (according to Janbu, 1963), $\alpha = 1$ is an appropriate value which provides rather realistic results for different clays, e.g. Butterfield [15], Mašín [59] and Medicus et al. [62].

However, the power law suggested by Janbu (1963) for clay has some limitations: the vertical stress cannot start from stress free state. Furthermore, the vertical stress should be $T_{11} \geq T_{11,0}(1+e_0)^{\chi}$, otherwise the void rate will be less than zero (see Fig. 3.9). These shortages also applies to other compression laws, which consider a linear relationship in the $\ln(1+e)$-$\ln(3p)$ space.

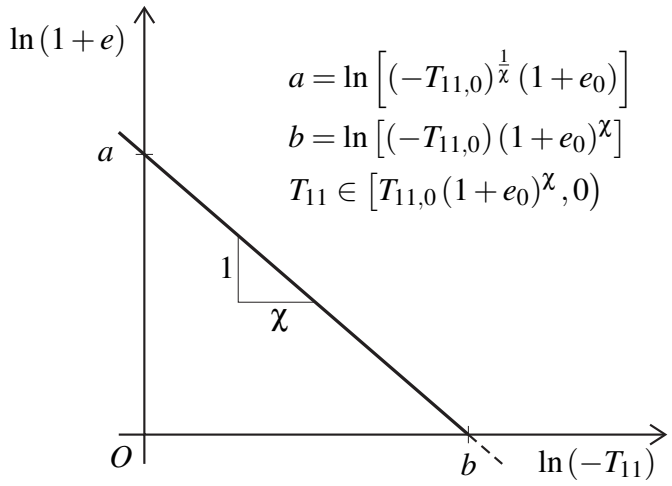

Figure 3.9: The power law by Janbu(1963) for compression behaviour of clay

For a value of $\alpha = 0$, which is suggested for rock by Janbu in 1963, Eq. (3.10) leads to

$$\ln(1+e) = -\frac{T_{11}}{\chi T_{ref}} + \frac{T_{11,0}}{\chi T_{ref}} + \ln(1+e_0) \tag{3.16}$$

with an initial state of: $T_{11} = T_{11,0}$ and $e = e_0$. If the initial stress is set equal to the reference stress, $T_{11,0} = T_{ref}$, Eq. (3.16) yields

$$\ln(1+e) = -\frac{T_{11}}{\chi T_{ref}} + \frac{1}{\chi} + \ln(1+e_0) \tag{3.17}$$

For $0 < \alpha < 1$, Eq. (3.10) leads a equation for compression law of materials like sand, i.e.

$$\ln(1+e) = -\frac{1}{(1-\alpha)\chi T_{ref}^{1-\alpha}}\left(T_{11}^{1-\alpha} - T_{11,0}^{1-\alpha}\right) + \ln(1+e_0) \tag{3.18}$$

herein $T_{11,0}$ and e_0 stand for the initial vertical stress and corresponding initial void ratio. If the initial vertical stress is equal to the reference stress T_{ref}, the Eq. (3.18) can be simplified as

$$\ln(1+e) = -\frac{T_{11}^{1-\alpha}}{(1-\alpha)\chi T_{ref}^{1-\alpha}} + \frac{1}{(1-\alpha)\chi} + \ln(1+e_0) \tag{3.19}$$

The Eq. (3.19) can be represented in the e-T_{11} form as:

$$e = (1+e_0)\exp\left[\frac{1}{(1-\alpha)\chi}\right]\exp\left[-\frac{1}{(1-\alpha)\chi}T_{11}^{1-\alpha}\right] - 1 \tag{3.20}$$

Note that the compression law for sand by Janbu (1963) should be limited to the stress range $T_{11} \in \left[\{(1-\alpha)\chi\ln(1+e_0)+1\}^{1/(1-\alpha)}T_{ref}, 0\right)$. If the vertical stress is less than

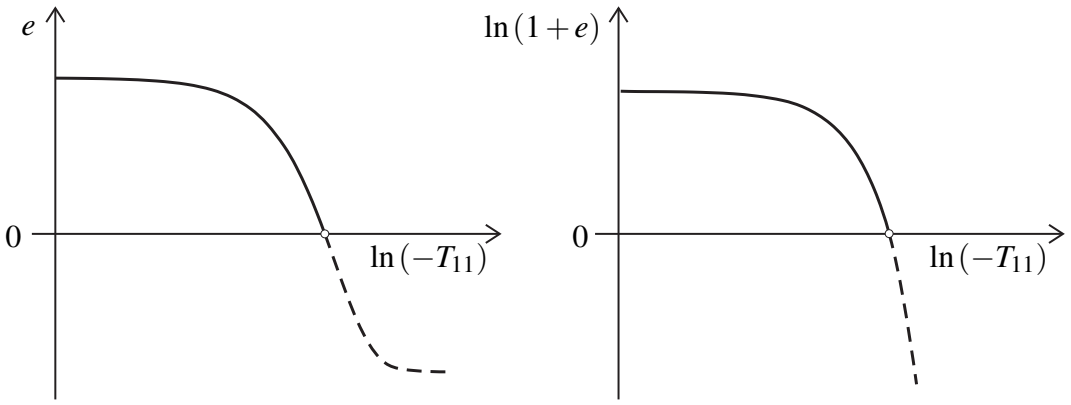

Figure 3.10: Different representations of the compression law of Eq. 3.19 with $\alpha = 0.5$ and $\chi = 100$

the lower bound value, negative void ratio can be archived according to the Eq. (3.19) (Fig. 3.10).

According to Muir Wood [66], the suggested range of α and χ for sands are $\alpha \in [0.2, 0.8]$ and $\chi \in [100, 1000]$. It is suggested that α and χ are parameters depending on the value of void ratio (see Fig. 4.11 of Muir Wood [66]).

Compression law by Pestana, 1995

Pestana and Whittle [76] proposed a compression equation defined in a linear $\ln(e)$-$\ln(p)$ space

$$\ln(e) = -\rho_c \ln\left(\frac{p}{p_{ref}}\right) \tag{3.21}$$

with a slope $-\rho_c$ in the $\ln(e)$-$\ln(p)$ space. p_{ref} is the reference pressure for the void ratio $e = 1$. The equation is actually proposed for the hydrostatic limit compression curve (HLCC in Fig. 3.11a) of high stress level range. This HLCC is the upper limit of the $\ln(e)$-$\ln(p)$ space, of which all possible void ratios should lie beneath. Hydrostatic compressions with different initial void ratios (HCC1 and HCC2 as shown in Fig. 3.11a) should approach the HLCC asymptotically. The compression curve with greater initial void ratio as illustrated by the red dashed curve in Fig. 3.11a should not cross the one with smaller initial void ratio (HCC2 in Fig. 3.11a).

For the lower-stress range, Pestana and Whittle [76] suggested to simulate the compression curve by a relation between e and p

$$\ln\left(\frac{e}{e_0}\right) = -e_0^{1/\rho_c}\beta\left(\frac{p}{p_{at}}\right) - \frac{3}{2C_b}\left(\frac{p}{p_{at}}\right)^{2/3} \tag{3.22}$$

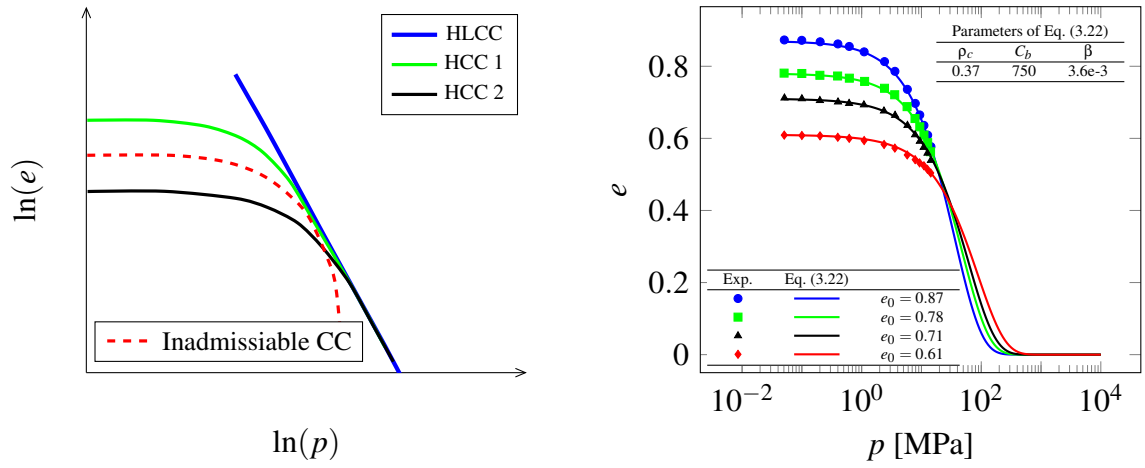

(a) (b)

Figure 3.11: Performance of compression equation by Pestana and Whittle (1995): (a)conceptual interpretation of hydrostatic limit compression curve (HLCC); (b)compression of experimental data by Lee and Seed [53] and compression equation (Eq. (3.22)) by Pestana and Whittle [76].

with the constants ρ_c, β and C_b. Here p_{at} denotes the atmospheric pressure. As shown in Fig. 3.11b, the numerical results obtained with Eq. (3.22) using the single set of parameters are in good agreement with the four experiments starting from different initial void ratios. However, the predictions are clearly inadequate for higher stress levels, i.e. compression curve for the initially dense specimen crosses the curve predicted for the initially loose specimen.

Compression law by Bauer, 1996

In general, the compression behaviour of granular material, especially of the crushable material, is strongly nonlinear over the entire possible stress range. The compression law introduced by Bauer [6] is characterized by mathematical simplicity, and only the three parameters e_{i0}, h_s and n are required:

$$e_i = e_{i0} \exp\left[-\left(\frac{3p}{h_s}\right)^n\right] \tag{3.23}$$

With the initial limit void ratio, e_{i0}, the so-called solid hardness, h_s, and the exponent n. The latter is related to the slope of the compression curve, Eq. (3.23) describes a compression relation between maximum void ratio e_i and mean pressure p, within a stress range of $p \in [0, +\infty]$. Moreover, this curve forms an upper bound of the possible void ratio in the e-p space. This upper limit can be reached under an ideal isotropic compression. In the

laboratory test, this ideal isotropic compression condition cannot archived due to the effect of the gravity.

The shapes of the compression curve described by the Eq. (3.23) in linear and semi-logarithmic representations are shown in the Fig. 3.12.

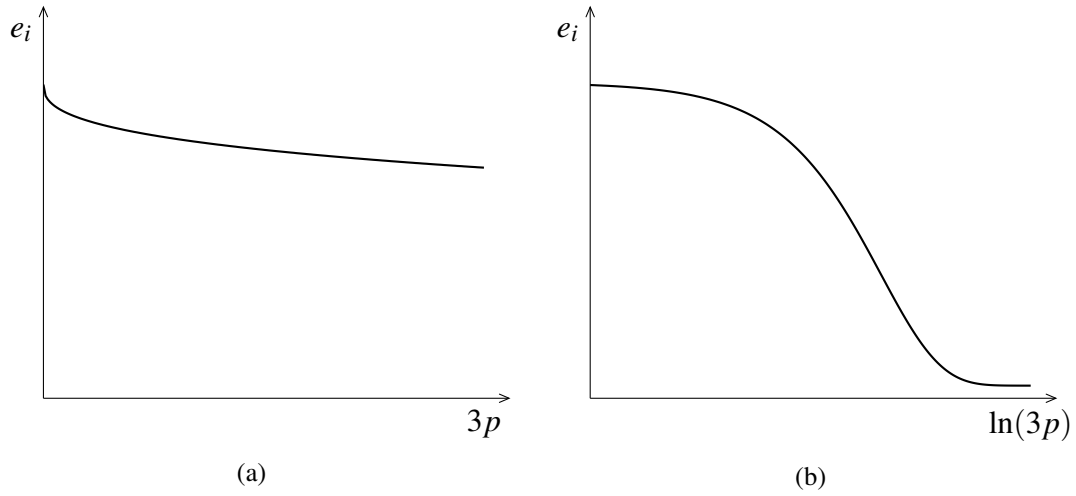

Figure 3.12: Compression curve: (a)linear representation; (b)semi-logarithmic representation.

The main properties of the compression equation can be better demonstrated by considering the following form:

$$f(x) = f(x_0) \exp\left\{ - \left[\frac{\exp(x)}{h_s} \right]^n \right\} \tag{3.24}$$

with $x = \ln(3p)$ and $f(x) = e_i$. The e_{i0} is represented by $f(x_0)$ with $x_0 = -\infty$ or with $p = 0$. Therefore, the slope of the compression curve (the derivative of the function $f(x)$ in Eq. (3.24)) can be explicitly expressed as

$$f'(x) = -f(x)\, n \left[\frac{\exp(x)}{h_s} \right]^n \tag{3.25}$$

The derivation of the Eq. (3.25) is detailed in Appendix A.1. As shown in Fig. 3.13, the slope of the curve decreases from 0 to the minimum value $-f(x_0)\exp(-1)n$. After the minimum value is reached, the slope approaches to 0 with $x \to +\infty$.

When the point of inflection of the compression curve is reached $x = \ln(h_s)$, the corresponding value of the function is $f(x) = f(x_0)\exp(-1)$. Another representation of this relation is $f(x_0) = f(x)\exp(1)$. Therefore, the value of $f(x)$ at the point of inflection can be used to calculate the initial value of the function $f(x_0)$.

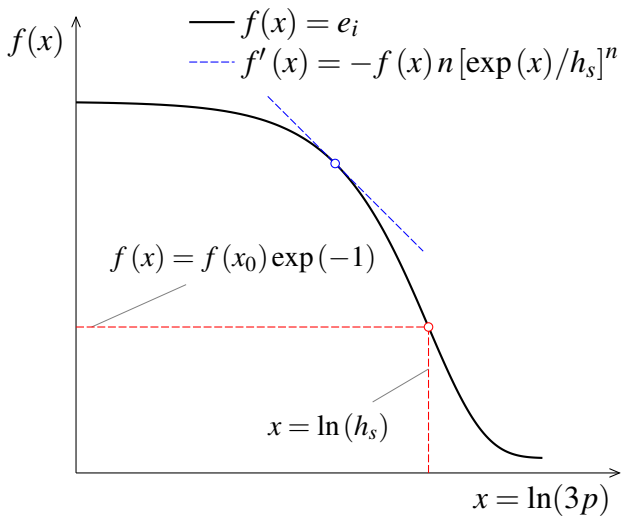

Figure 3.13: Characteristics of the compression law by Bauer [6].

Furthermore, according to the Eq. (3.24), the curvature $\kappa(x)$ of the compression curve can be derived analytically (Appendix A.1)

$$\kappa = \frac{f(x)\, n^2 \left[\frac{\exp(x)}{h_s}\right]^n \left\{ \left[\frac{\exp(x)}{h_s}\right]^n - 1 \right\}}{\left\{ 1 + [f(x)]^2 n^2 \left[\frac{\exp(x)}{h_s}\right]^{2n} \right\}^{3/2}} \tag{3.26}$$

For $x = \ln(h_s)$, the curvature becomes $\kappa = 0$.

In Fig. 3.14, $f(x)$ and the corresponding curvature $\kappa(x)$ are plotted. First the compression curve decreases to a minimum value and then it increases to a maximum value which is greater than zero. After the peak the curvature decreases again to tend asymptotically to zero. Thus, the compression curve defined by the Eq. (3.23) describes three phases, which can be interpreted according to Fig. 3.15:

At low stress levels (Phase I), the deformation of grain assembly is mainly due to particle rearrangement, achieved by overcoming interparticle friction through sliding and rotation. This particle rearrangement may be accompanied by abrasion of surface asperities. When the compression increases grain crushing occurs. With increasing pressure the amount of fracturing increases (Phase II). At very high stresses the void ratio tends to zero and a phase transition (diagenesis) takes place (Phase III) (Vesić and Clough [88]; Pestana and Whittle [76]; Mesri and Vardhanabhuti [63]).

The compression law (Eq. (3.23)) reflects these three phases. It is interesting to compare the transition states of these three phases with the extreme values of the curvature curve

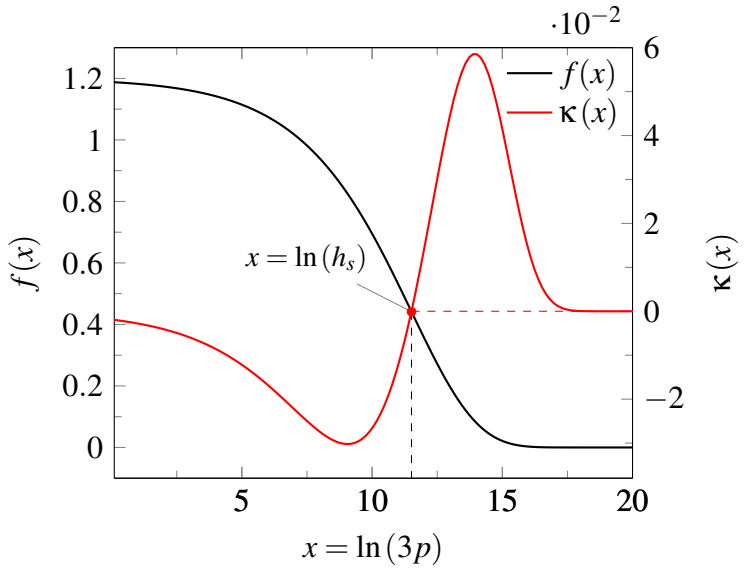

Figure 3.14: Compression curve $f(x)$ and curvature curve $\kappa(x)$ for $h_s = 100$ MPa, $n = 0.4$ and $e_0 = 1.2$.

$\kappa(x)$. In particular the two extreme values of $\kappa(x)$ separate the compression curve into three parts. The minimum value of curvature is frequently related to the yield stress concept for granular materials (e.g. Carter et al. [16]; Coop and Atkinson [19]; McDowell et al. [60]; Nakata et al. [68]; Mesri and Vardhanabhuti [63]). The range between the minimum and maximum value of curvature can be related to phase II of the compression curve where grain crushing becomes dominant (Bauer et al. [12] and Laufer [52]). After phase II the additional reduction of the void ratio for the same stress increment becomes smaller and smaller.

The mathematical analysis of the Eq. (3.23) can be summarized as follow:

- The slope of the compression curve can be expressed by $-e_i n (3p/h_s)^n$.
- The point of inflection of the curve is defined for $3p = h_s$ and $e_i^* = e_{i0} \exp\{-1\}$. For the case e_i^* is known the initial maximum void ratio can be calculated from

$$e_{i0} = e_i^* \exp\{1\} \tag{3.27}$$

- The extreme values of the curvature curve allow the distinction of three different phases of the compression curve.

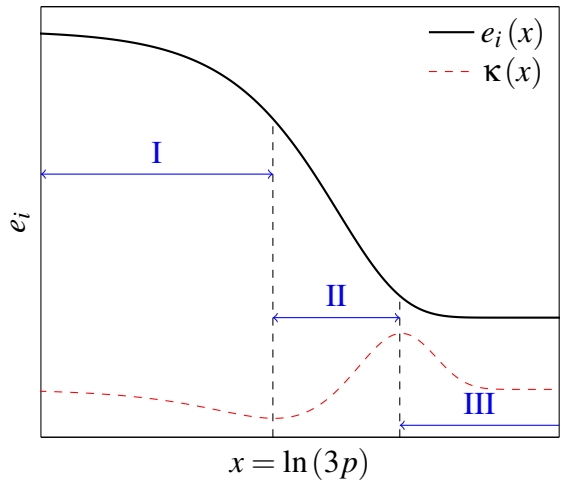

Figure 3.15: Phases of the compression law by Bauer(1996)

Ideal oedometric compression based on Bauer's law

The compression law by Bauer [6] is originally defined for ideal isotropic compression curve, i.e. an isotropic compression starting from the maximum void ratio e_{i0} $(p = 0)$. The same function can also be used to approximate the behaviour under oedometric condition. Recalling the proportional strain paths theory by Goldscheider [21], the proportional path and asymptotic behaviour under isotropic compression is illustrated in Fig. A.2a. Considering an oedometric compression test starting from the initial stress free state and $e = e_{o0}$, the corresponding stress paths will be proportionally as well and $T_{22} = T_{33} = K_0 T_{11}$. The compression curve of the ideal oedometric compression will act as an attractor for cases oedometric compression starts from another initial state. This explains why with different initial densities, the oedometric compression curves converge into a unique curve after reaching a certain stress level (see Fig. 3.4). Based on the proportional strain and stress paths theory, the limit void ratio curve and normal compression curve in e-$\ln(p)$ space can be illustrated as in Fig. 3.16. Here the K_0 is considered as constant, some soft grains show increasing values of K_0 with vertical stress increased (i.e. after Yamamuro et al. [100]).

For the given ideal oedometric compression condition, the mean pressure can be represented as $p = T_{11}(1+2K_0)/3$. Therefore, the compression equation by Bauer [6] can be represented as:

$$e_o = e_{o0} \exp\left\{-\left[\frac{T_{11}(1+2K_0)}{h_s}\right]^n\right\} \tag{3.28}$$

Herein e_o denotes the void ratio of ideal oedometric compression at a stress state with $p = T_{11}(1+2K_0)/3$. Alternatively, the Eq. (3.28) can be expressed as

$$e_o = e_{o0} \exp\left[-\left(\frac{T_{11}}{h_s^*}\right)^n\right] \tag{3.29}$$

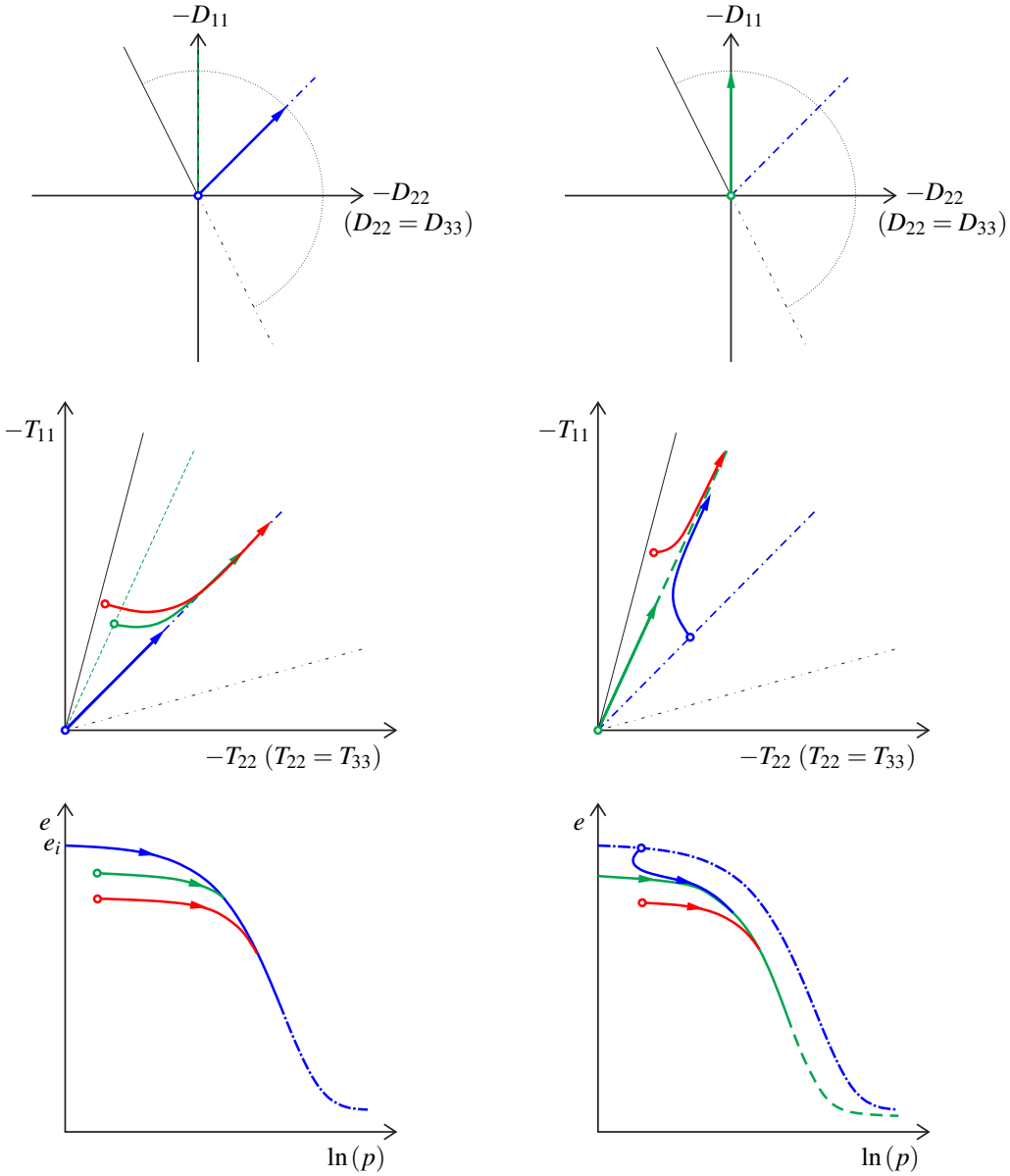

(a) isotropic compression (b) oedometric compression

Figure 3.16: Proportional paths under axisymmetric condition and asymptotic behaviour: (a) isotropic compression; (b) oedometric compression.

with $h_s^* = h_s/(1+2K_0)$. Similar to the feature of Eq. (3.27), the e_{i0} can be calculated according to the point of inflection the ideal oedometric compression curve defined by Eq. (3.29)

$$e_{o0} = e_o^* \exp\{1\} \tag{3.30}$$

where e_o^* is the void ratio at the inflection point. The quantity e_{o0} is smaller than e_{i0}. According to the ideal oedometric compression concept, the oedometric experimental results also can be used to calculate the e_{o0}. Then the calculated e_{o0} can be used to estimate e_{i0} according to the concept $e_{i0} > e_{o0}$. For instance, if the point of inflection is known, e_{o0} can be estimated from Eq. (3.30). As shown in Table 3.1, the values of e_{o0} for the sands in Fig. 3.4 can be calibrated according to the point of inflection.

Table 3.1: Prediction of initial value of maximum limit void ratio of sands (from Fig. 3.4)

Sand	Feldspar	Quiou	Ottawa	Quartz	Cambria	Gypsum
$-T_{11}$ [MPa]	18	15.2	144	46.2	47.8	11.7
e_o^*	0.57	0.512	0.372	0.478	0.334	0.409
e_{o0}	1.55	1.39	1.01	1.30	0.91	1.11

If K_0 is not known, h_s^* or h_s cannot be determined from data of oedometric compression test, i.e. from T_{11}-ε_{11} data.

Provided K_0 is known either from special oedometric device (Kolymbas and Bauer [47] and Yamamuro et al. [100]) or K_0 is estimated, the ideal compression curve can be approximated according to Eq. (3.23). For Dog's Bay sand which is a highly crushable biogenic carbonate sand with fragile particles mainly composed of broken shell fragments (Altuhafi and Coop [4]), the calibration results obtained for isotropic and oedometric compression are shown in Fig. 3.17.

Application scope

As summarized by Pestana and Whittle [76], the compression behaviour is mainly affected by: initial density, mineralogy and structure of particles, granulometric properties (particle size, shape, angularity, and grain size distribution). Therefore a statistical evaluation to deal with such complex is inevitable. The compression law proposed by Bauer [6] is developed based on the Karlsruhe sand in a statistical manner. The compression equation has three parameters, e_{i0}, h_s and n. The equation takes into account the stiffness and strength properties of the grain assembly by h_s with exponent n, describes the whole compression history from the stress free state to the infinity stress level.

Broad agreement can be find in literature that the fine grains are less likely to be crushed than the coarse ones. Therefore, for those fine materials, i.e. clay and silt, the phase I

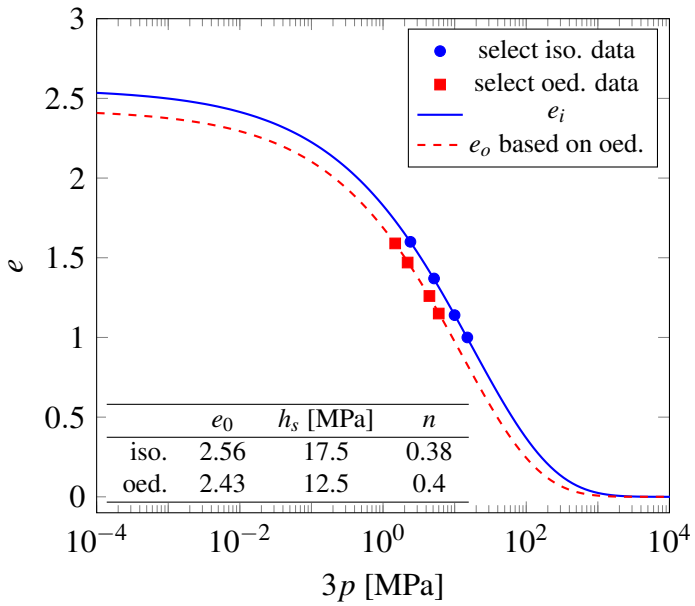

Figure 3.17: Prediction of compression curves of Dog's Bay sand using experimental data from Coop [18] for the prediction of h_s, n, e_{i0} and e_{o0}.

(illustrated in Fig. 3.15) is sufficient to describe the compression behaviour of the materials (another manner is to consider linear relation in e-$\ln(p)$ or in $\ln e$-$\ln(p)$). As the discrete element modeling (DEM) simulation shown by Laufer [52] (in Fig. 3.18) that the grains without grain crushing under oedometric compression condition has similar shape as the phase I of compression curve by Bauer [6], and the compression curve with considering grain crushing has similar shape as the one according to Eq. (3.29).

The compression equation by Bauer [6] is developed based on the analysis of experimental investigation of Karlsruhe sand and can also be used to simulate the compression behaviour of other sands, e.g. Herle and Gudehus [27]; Anaraki [5] and Phuong et al. [77]. The calibration and numerical simulation of sandstone by Li et al. [56] shows that the compression equation can be used for coarse granular material as well. By calibrating the parameters based on the experimental data of metal powders by Heckel (1961) from [76], it shows that the compression equation is appropriate for metal powders as well.

Some aspects about the application of the compression law by Bauer [6] should be emphasized:

(a) *remoduling*; The remoduling should be treated differently from the unloading. Remoduling normally will change the grain skeleton significantly, and the smaller initial maximum limit void ratios should be taken into account since the during the loading before remoduling grain crushing changes the GSD. Thus the original grain skeleton cannot be reached any more. Of course for those condition with insignificant grain

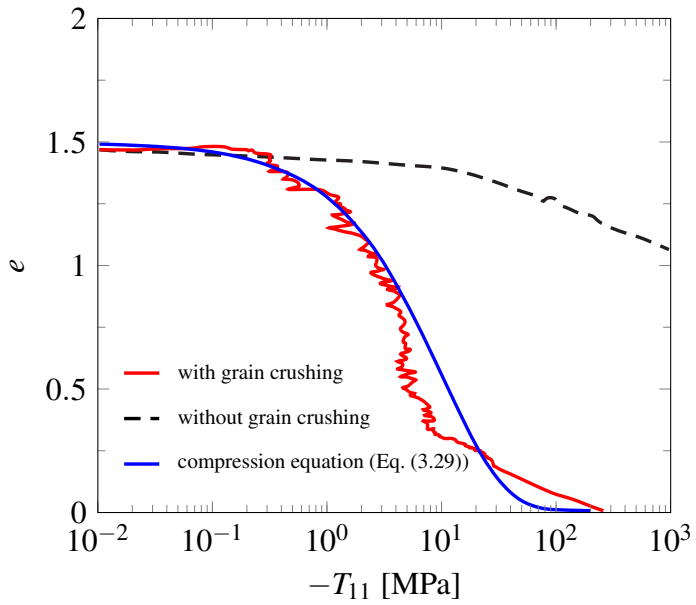

Figure 3.18: Comparison of compression curves under oedometric compression with grain crushing and without grain crushing from DEM simulation by Laufer [52]. The figure is replotted and compared with the compression curve proposed by Bauer [6] with $e_{i0} = 1.5$, $h_s^* = 10^4$ MPa and $n = 0.8$.

crushing occurred, the remoduling will not have strong influence on the h_s and n, and on this giving condition, considering the same h_s and n is acceptable.

(b) *fluids*; Pore fluid, fluid saturation can affect the compressibility of cohesionless materials (e.g. Nobari and Duncan [70]; Miura and Yamanouchi [64]; Kast et al. [39]; Oldecop and Alonso [71]; Ovalle et al. [74]). The different compressibilities imply the stiffness (related to crushing resistance) changed during the process of adding fluids. Therefore, the changing of solid hardness should be taken into account as well. Details are outlined in Section 3.2.

(c) *time-dependent behaviour*; Time dependent phenomena (e.g. Schmertmann [80]; Oldecop and Alonso [72]; Ovalle et al. [74]), i.e. creep and stress relaxation (e.g. Karimpour and Lade [36]; Karimpour and Lade [37]), which lead volume change, cannot be described with a constant solid hardness.

Bauer [8] extended the Eq. (3.6) by considering the solid hardness is a time-dependent quantity during the process of adding fluid and it will degrade into a value related to the fully saturation state of the material

$$e_i = e_{i0} \exp\left[-\left(\frac{3p}{h_{st}}\right)^n\right] \tag{3.31}$$

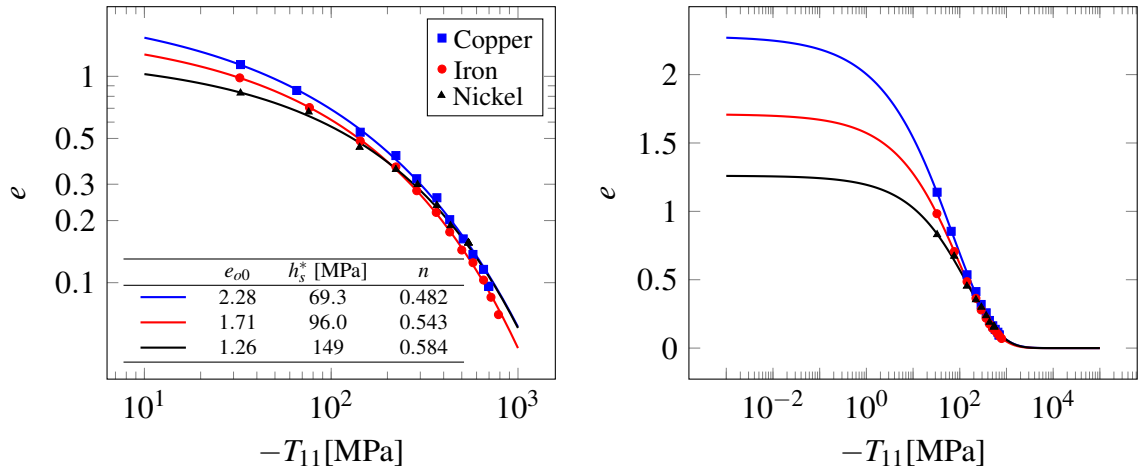

Figure 3.19: Prediction of metal powders at high stress levels using Bauer's equation: (a)parameter sets of compression equation (Eq. (3.29)) for metal powders [76]; (b)prediction with large stress range.

with

$$h_{st} = h_{sw} + (h_{sd} - h_{sw}) \exp\left(-\frac{t}{c}\right) \tag{3.32}$$

Note that it takes time to reach a stable state after fully saturation, therefore the degradation of solid hardness should last longer than saturation. Details of the time-dependent compression relation are outlined in Chapter 4.

3.2 Behaviour of moisture sensitive materials

As mentioned in Chapter 1, a change of the moisture content can lead to an increase of the compressibility of coarse-grained and weathered rockfills. This phenomenon can be explained as the degradation of the strength of the solid grains caused by hydrochemical process inside of the micro cracks. The additional deformation after wetting of the material is usually called *wetting deformation*.

From the experimental observations, main conclusions can be summarized as: (a) under one-dimensional compression condition, after wetting the compression curve of initially dry specimen approaches to the initially wet compression curve, with continue loading, the dry-wet compression curve follows the initially wet one; (b) for the specimen under triaxial compression condition, the stress- and volumetric strain-axial strain curves shift from the initially dry ones and approached to the initially wet ones asymptotically; (c) for the relative coarse material (i.e. sand and rockfill), the wetting deformation is mainly caused by the additional grain crushing.

3.2.1 Experimental observations

Howson [30] reported a sudden increase in settlement after a flood during the construction of Dix River Dam, due to saturation of the partially completed embankment (Fig. 3.20a). This field observation starts the hypothesis about crushing-upon-wetting.

Sowers et al. [82] tested the jetting effects on settlement of rock and observed that the initial wetting causes additional settlement of rock comparing with the initial dry rock, and jetting dry rock will cause additional settlement of rock as well (Fig. 3.20b). Due to the fact that the impervious graywacke and the more pervious sandstone had similar wetting deformation, the authors concluded that the mineral bond softening by wetting is not appropriate explanation for the wetting deformation of rocks. Wedge-shaped intact rocks were tested for investigating the effect of wetting on contact points (local) crushing. Splitting was observed immediately after the contact points were wetted, consequently induced the sudden compression of the specimens. The authors concluded that the crushing of contact points is caused by a locally increased stress and additional cracks propagation which induced by the entering of water in the microcracks of the highly stressed contact points.

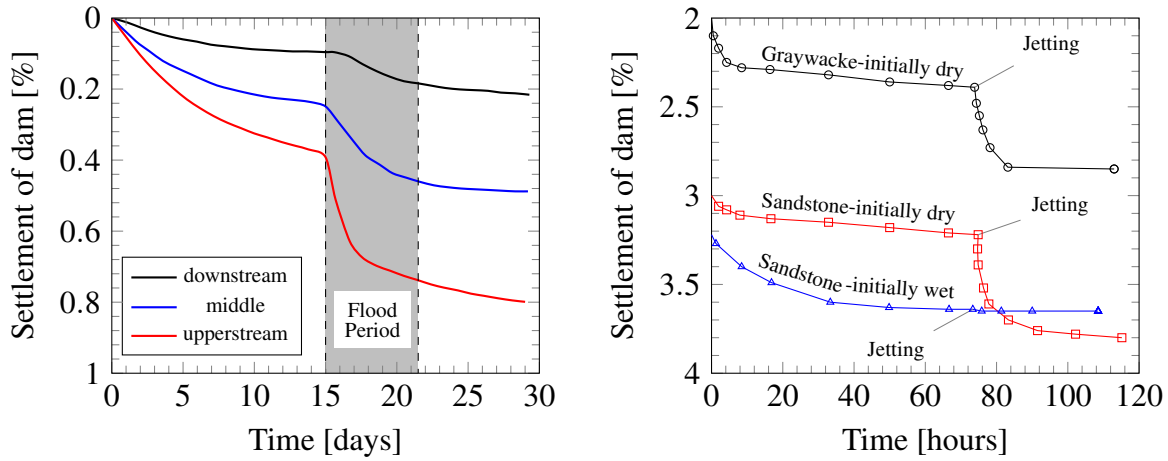

(a) Field observation of settlements at the same level of Dix River Dam (redrawn from Howson [30])

(b) Laboratory tests of graywacke and sandstone with wetting at 0.78 MPa (from Sowers et al. [82])

Figure 3.20: Field and experimental observation of wetting effect on settlement of rock

Holestöl et al. [29] investigated the effect of wetting on the settlement of Venemo Dam in Norway, which was constructed of granitic gneiss and amphibolite rockfill, and discovered similar relation of the vertical stress and settlement (Fig. 3.21a).

Leonards and Altschaeffl [55] found that a significant wetting deformation occurred when water was added to compacted specimens of limestone residual clay (with initial water

content $\omega = 14.9\%$) during one-dimensional compression (Fig. 3.21b). This discovery also proved that the wetting deformation can occur in different particle size granular materials in partial saturation state (stated by Jennings [34]).

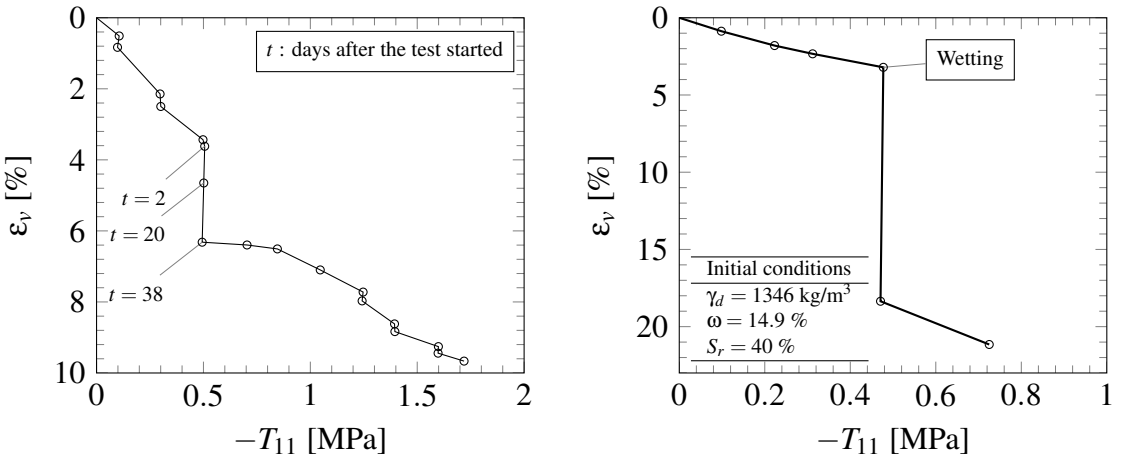

(a) Compression behaviour of Venemo Dam material (redrawn from Nobari and Duncan [70])

(b) Compression behaviour of limestone residual clay (after Leonards and Altschaeffl [55])

Figure 3.21: Wetting deformation under oedometric compression

Nobari and Duncan [70] tested the Pyramid material under one-dimensional condition, and found similar tendency of compression curves as the material showed in triaxial compression tests (see Fig. 3.22a).

Kast et al. [39] referred to a set of one-dimensional compression tests performed on weathered broken granite with different dynamic compaction energy (λ_p in Fig. 3.22b) that showed the granite exhibited the same compression behaviour as the one of Pyramid material.

Oldecop and Alonso [71] conducted laboratory tests with specimen flooding and relative humidity control on Pancrudo slate. Ovalle et al. [74] investigated an angular sand, obtained from a quartzite shale rock by grinding, in oedometric and triaxial compression tests with different wetting stress levels and different stress paths (creep, stress relaxation). All these oedometric compression test results show the same phenomenon: when the specimen is wetted, the compression curve transform from the initially dry compression curve to the initially wet compression curve and follow the wet compression curve with continuing loading.

Vesić and Clough [88] conducted a set of triaxial compression tests up to high stress level ($p_{max} = 118.83$ MPa) with sand samples and found that the wetting leads additional crushing of sand when comparing to the dry specimen, and the particle crushing is more pronounced in the specimen with triaxial compression path than in the specimen under isotropic compression condition.

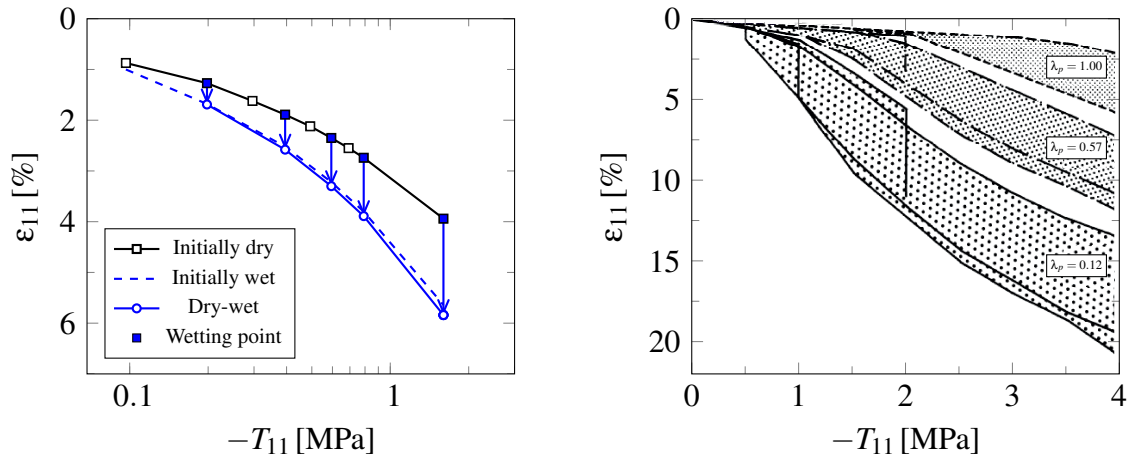

(a) Wetting deformation of pyramid material (redrawn from Nobari and Duncan [70])

(b) Wetting deformation of weathered broken granite (redrawn from Kast et al. [39])

Figure 3.22: Oedometric compression behaviour of materials under dry and wet condition

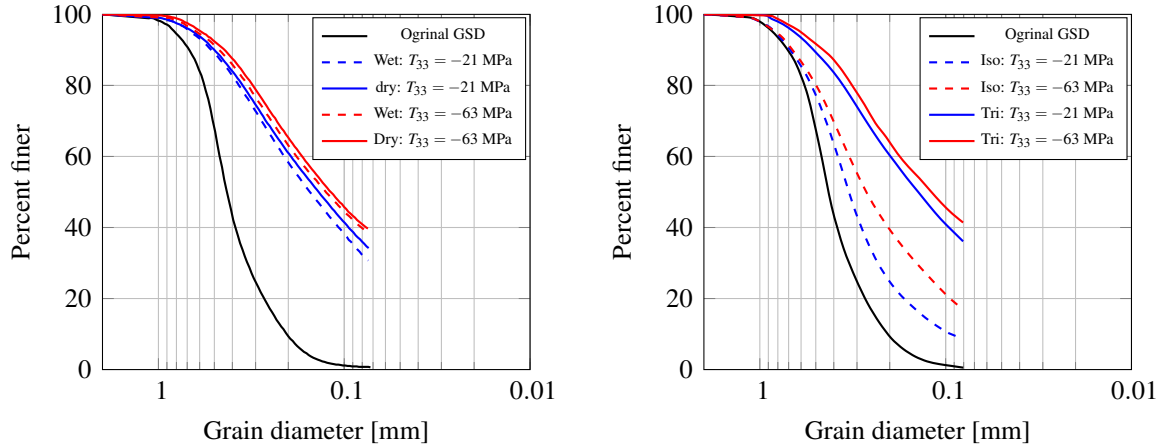

(a) Wetting effect on grain crushing

(b) Stress path effect on grain crushing

Figure 3.23: Effects of wetting and stress path on GSD

3.2.2 Constitutive modelling of wetting deformations

Alonso et al. [3] proposed a constitutive model (Barcelona basic model) for unsaturated soils to simulate the phenomenon of wetting deformation. Based on the unsaturated soil mechanics, the concept of crack propagation velocity (by Laidler [51]) and previous works referred to Barcelona basic model, Oldecop and Alonso [71] introduced a model for rockfill compressibility.

Recalling the fact that after wetting the compression curves approach to the initially wet

curve independent of the stress or strain paths, i.e. creep (A-C path) as shown in Fig. 3.24b or stress relaxation (A-B path), as mentioned in Section 3.2.1), and considering the process of shifting from dry curve to wet curve takes time. Based on the stiffness degradation concept Bauer [8] proposed the compression curve shifting process by introducing the time dependent solid hardness h_{st} and replaced the term h_s in Eq. (3.6). Therefore, the compression curves for dry, wet and the transition from dry to wet can be described by substituting the h_s in Eq. (3.6) with h_{sd}, h_{sw} and h_{st}, respectively.

With respect to that the h_{st} is considered as a time-dependent quantity, h_{st}, the derivative of Eq. (2.17) yields (Bauer [8]):

$$\dot{e}_i = -e_i n \left(\frac{3p}{h_{st}}\right)^n \left(\frac{\dot{p}}{p} - \frac{\dot{h}_{st}}{h_{st}}\right) \tag{3.33}$$

Based on the Eq. (3.33), the creep deformation (or wetting deformation, collapse, A-C path in Fig. 3.24) can be described by setting the $\dot{p} = 0$, and the stress relaxation (A-B path in Fig. 3.24) can be archived with considering $\dot{p}/p = \dot{h}_{st}/h_{st}$. Although, the stress-strain path between the creep and stress relaxation paths, illustrated as A-D in Fig. 3.24, can be described using Eq. (2.17) and Eq. (2.17). Note that the partly saturated state (illustrated as the red dashed line Fig. 3.24) can be described using the Eq. (2.17) as well, however it is not covered in this work.

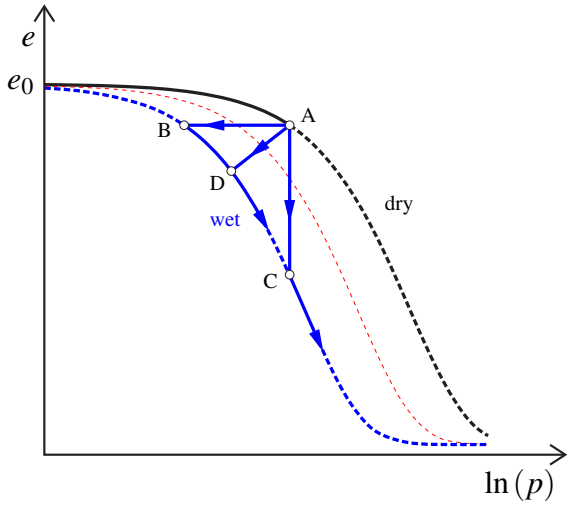

Figure 3.24: Conceptual model for wetting deformation: (a) subcritical crack growth curves after Oldecop and Alonso [71], slightly modified; (b) stiffness degradation after Bauer [8].

4 A simplified hypoplastic model for stiffness degradation

In this chapter, a simplified hypoplastic constitutive model for stiffness degradation is outlined as follows: the general equation of the simplified constitutive model is given in Section 4.1; in Section 4.2 the consistency condition proposed by Gudehus [22] is addressed to illustrate how the compression law can be taken account into the constitutive equation; the standard calibration procedure of the model is detailed in Section 4.3; the hypoplastic element test program (HET) is introduced in Section 4.4.

4.1 General equation of the simplified hypoplastic model

In this work the general equation of the simplified model is proposed as follows:

$$\mathring{\mathbf{T}} = \check{f}_s \left\{ \hat{a}^2 \mathbf{D} + \mathrm{tr}\left(\hat{\mathbf{T}}\mathbf{D}\right)\hat{\mathbf{T}} + \check{f}_d \hat{a} \left(\hat{\mathbf{T}} + \hat{\mathbf{T}}^*\right) \|\mathbf{D}\| \right\} + \frac{\dot{h}_{st}}{h_{st}} \left\{ \frac{1}{3}\,\mathrm{tr}\,(\mathbf{T})\mathbf{I} + \kappa \mathbf{T}^* \right\} \tag{4.1}$$

and

$$e_i = e_{i0} \exp\left\{ -\left(\frac{3p}{h_{st}}\right)^n \right\} \tag{4.2}$$

with:

- $\dot{h}_{st} = 0$ for constant solid hardness, like dry or wet condition[1]
- $\dot{h}_{st} \neq 0$ for stiffness degradation.

In particular, the constant solid hardness for the dry condition differs from the one of wet condition. Therefore, additional subscripts d and w are used in the terms, h_{sd} and h_{sw}, to denote the solid hardness of the material under the dry and wet conditions, respectively. And the stiffness degradation is described based on the Eq. (3.32) which is proposed by Bauer [8]:

$$h_{st} = h_{sw} + (h_{sd} - h_{sw}) \exp\left\{ -\frac{t}{c} \right\} \tag{4.3}$$

herein, c is a constant with dimension of time. The time derivative of the Eq. (4.3) reads:

$$\dot{h}_{st} = -\frac{1}{c}\,(h_{st} - h_{sw}) \tag{4.4}$$

[1] Here the wet condition refers to the stable state after fully saturation. Before the stable state reached, the stiffness degradation should be taken into account.

In this simplified model, the density factor in Eq. (2.8) is replaced by the following expression:

$$\check{f}_d = \left(\frac{e}{e_c}\right)^{\check{\alpha}} \tag{4.5}$$

It is obvious that the minimum void ratio e_d is not included in Eq. (4.5). The reason is twofold: for monotonic loading, the minimum void ratio e_d defines the lower bounds of the possible void ratios. However, for unloading, the lower bound defined by e_d might be crossed over, as illustrated in Fig. 4.1a. In addition, the calibration of e_d is rather difficult as mentioned in Herle and Gudehus [27]. Another argument to choose Eq. (4.5) is the fact that the number of constitutive parameters can be reduced.

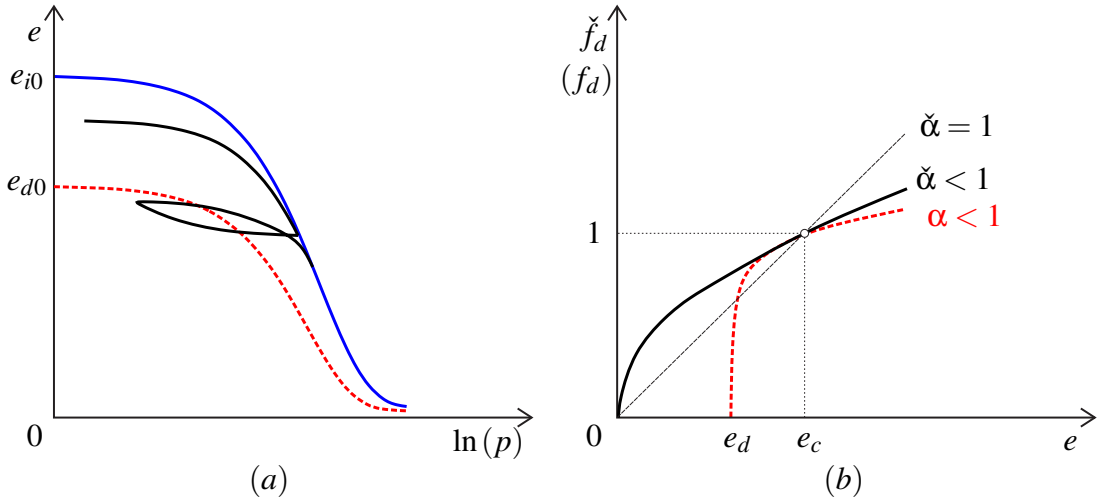

Figure 4.1: Reason for new density factor: (a) limit void ratios and unloading/reloading; (b) relation between density factor and void ratio.

The same function for the density factor is also suggested by Li et al. [56], Wang [91], Wang et al. [93] and Wang et al. [92].

Note that for $e = e_c$, the value of the density factor $f_d = 1$.

With the simplified density factor, the stiffness factor $\check{f}_s$ differs from the stiffness factor f_s mentioned in Eq. (2.8). The derivation of the stiffness factor $\check{f}_s$ is outlined in Section 4.2

The total number of parameters of the simplified model is compared with the reference model in Table 4.1. In the simplified model, h_s stands for h_{sd} for dry material; h_s represents h_{sw} for the wet material.

Table 4.1: Parameters of reference model and simplified model

Models		Parameter set											Total num.
Ref. Model	Eq. (4.19)	φ_c	h_{s0}	/	n	e_{i0}	e_{c0}	e_{d0}	α	β	/	/	8
	Eq. (4.20)	φ_c	h_{s0}	h_{sw}	n	e_{i0}	e_{c0}	e_{d0}	α	β	c	κ	11
Simp. Model	Eq. (4.1)	φ_c	h_s	/	n	e_{i0}	e_{c0}	/	$\check{\alpha}$	/	/	/	6
	Eq. (4.1)	φ_c	h_{sd}	h_{sw}	n	e_{i0}	e_{c0}	/	$\check{\alpha}$	/	c	κ	9

4.2 Derivation of the required consistency condition

Recalling that the compression equation (Eq. (3.23)) proposed by Bauer [6] describes the ideal isotropic compression curve, the constitutive equation which takes into account the compression equation should be consistent with the compression equation by fulfill the requirements of ideal isotropic compression condition. This consistency concept is introduced by Gudehus [22]. Take the Eq. (4.1) as an example, if considering constant h_s, the consistency can be fulfilled as illustrated by following steps.

The ideal isotropic compression condition has the following characteristics: $e = e_i$, $\mathbf{T} = -p\mathbf{I}$, $\hat{\mathbf{T}} = \mathbf{I}/3$, $\hat{\mathbf{T}}^* = 0$ and $\mathbf{D} = \operatorname{tr}(\mathbf{D})/3\mathbf{I}$, provided with $p > 0$ and $\operatorname{tr}(\mathbf{D}) < 0$. Therefore, the mean pressure rate can be described as $\dot{p} = -\operatorname{tr}\left(\dot{T}\right)/3$, the Euclidean norm of stretching tensor is $\|\mathbf{D}\| = -\sqrt{3}/3\operatorname{tr}(D)$, and the stiffness factor for ideal isotropic compression condition can be represented as $\check{f}_{di} = (e_{i0}/e_{c0})^{\check{\alpha}}$. Thus, the rate of mean pressure can read as

$$\dot{p} = -\frac{1}{3}\check{f}_s\left\{\hat{a}_i^2 + \frac{1}{3} - \frac{\sqrt{3}}{3}\check{f}_{di}\hat{a}_i\right\}\operatorname{tr}(\mathbf{D}) \tag{4.6}$$

Recalling the Eq. (3.1), the relation between void ratio and stretching tensor of ideal isotropic compression can be described as $\dot{e}_i = (1+e_i)\operatorname{tr}(\mathbf{D})$, then the Eq. (4.6) can be written as

$$\dot{p} = -\frac{1}{3}\check{f}_s\left\{\hat{a}_i^2 + \frac{1}{3} - \frac{\sqrt{3}}{3}\check{f}_{di}\hat{a}_i\right\}\frac{\dot{e}_i}{1+e_i} \tag{4.7}$$

From the compression equation Eq. (3.23), the rate of void ratio can be derived as

$$\dot{e}_i = -e_i n\left(\frac{3p}{h_s}\right)^n\left(\frac{\dot{p}}{p}\right) \tag{4.8}$$

Therefore, the rate of mean pressure derives from Eq. (3.23) can be expressed as

$$\dot{p} = -\frac{p}{n}\left(\frac{3p}{h_s}\right)^{-n}\frac{\dot{e}_i}{e_i} \tag{4.9}$$

Then, according to Eq. (4.7) and Eq. (4.9), the stiffness factor for ideal isotropic compression can read as

$$\check{f}_{si} = 3\frac{p(1+e_i)}{e_i n}\left(\frac{3p}{h_s}\right)^{-n}\left\{\hat{a}_i^2 + \frac{1}{3} - \frac{\sqrt{3}}{3}\check{f}_{di}\hat{a}_i\right\}^{-1} \tag{4.10}$$

Set $\check{h}_i = \hat{a}_i^2 + 1/3 - \sqrt{3}/3\check{f}_{di}\hat{a}_i$, and considering for isotropic compression the factor f_s^* is equal to 3, the pressure dependent factor f_b reads

$$f_b = \frac{p(1+e_i)}{n e_i \check{h}_i}\left(\frac{3p}{h_s}\right)^{-n}\left(\frac{e_i}{e_c}\right)^{\beta} \tag{4.11}$$

Substitute Eq. (4.11) into Eq. (2.25), the general form of stiffness factor reads

$$\check{f}_s = \left(\frac{e_i}{e}\right)^{\beta}\frac{1+e_i}{n e_i \check{h}_i}\left(\frac{3p}{h_s}\right)^{-n}\frac{p}{\hat{\mathbf{T}}:\hat{\mathbf{T}}} \tag{4.12}$$

Therefore, with considering Eq. (4.12), the consistency condition of Eq. (3.23) and Eq. (4.1) without stiffness degradation is fulfilled.

For constitutive equation with considering stiffness degradation (Eq. (4.20)), the rate of mean pressure for ideal isotropic can be derived with the same procedure as illustrated before:

$$\dot{p} = -\frac{1}{3}\check{f}_s\left\{\hat{a}_i^2 + \frac{1}{3} - \frac{\sqrt{3}}{3}\check{f}_{di}\hat{a}_i\right\}\frac{\dot{e}_i}{1+e_i} - \frac{\dot{h}_{st}}{h_{st}}p \tag{4.13}$$

and the rate of mean pressure derived from Eq. (3.31) can be written as

$$\dot{p} = -\frac{p}{n}\left(\frac{3p}{h_s}\right)^{-n}\frac{\dot{e}_i}{e_i} - \frac{\dot{h}_{st}}{h_{st}}p \tag{4.14}$$

Therefore, the consistency condition can be fulfilled by considering Eq. (4.13) and Eq. (4.14). Obviously, the Eq. (4.12) is valid for the compression equation described by Eq. (3.31) as well.

Note that any modification or extension of either the constitutive equation or the compression relation, consistency condition should be considered as well. In another word, if any modification of the constitutive equation or the compression relation is made, the updating of stiffness factor need to be taken into account as well.

4.3 Direct calibration procedure

Referring to Table 4.1, the simplified model has nine parameters in total. In particular, seven parameters for classic constitutive equation, which is proposed for time-independent

material behaviour; nine parameters for the constitutive equation takes into account time-dependence, like creep and stress relaxation which shows stiffness degradation during a certain period of time. All these nine parameters can be calibrated based on the conventional laboratory tests as summarized in Table 4.2. And the calibration procedure for each parameter is discussed separately in following sections (except that the determination of parameter c and κ is illustrated in Chapter 5).

Table 4.2: Tests for parameter determination

Test	h_{sd}	h_{sw}	n	e_{i0}	φ_c	e_{c0}	$\check{\alpha}$	β	c	κ
Isotropic compression	✓	✓	✓	✓				✓		
Oedometer compression	✓	✓	✓	✓						
Triaxial compression					✓	✓	✓		✓	✓

4.3.1 Material parameters of the compression law by Bauer

In this work the h_s stands for h_{sd} or h_{sw} which distinguish the constant solid hardness from the solid hardness (h_{st}) degrades with time. Recalling that mentioned in Chapter 3, the h_s and n can be determined based on the experimental data from ideal isotropic compression or ideal oedometric compression tests, dry for h_{sd} and wet for h_{sw}. For the sake of simplicity, the n for the dry material is considered the same as the one determined from the wet tests. Based on the calibration will be mentioned in the next chapter, the difference of n calibrated from dry and wet tests is indeed can be ignore.

According to the discussion about asymptotic state of isotropic and oedometric compression test, the data from ideal isotropic compression and ideal oedometric compression test should be considered to determine the h_s and n.

In particular for ideal isotropic compression, the loosest specimen at the stress free state cannot be prepared in the conventional laboratory because of the gravity field. In another word, it is difficult to determine the e_{i0} according to the conventional laboratory tests. While it is possible to prepare the specimen as loose as it can be by adding a slight amount of moist into the specimen (Ishihara [33], Bauer [6]). The looser specimen is prepared, the earlier asymptotic state of isotropic compression will be approached (in the e-lnp space, see Fig. 4.2a). From the application point of view, out of the available experimental data, the isotropic compression curve which lies above the other curves in the e-p space can be considered as the ideal isotropic compression curve, at least the best approximation which is available. The larger stress range the compression test covers, the better approximation can be archived. With the determined value of h_s and n, the e_{i0} can be easily calibrated based on the compression relation of Bauer, by curve fitting of the isotropic compression data or by back calculating according to Eq. (3.27).

However, note that for oedometric compression condition, the ideal oedometric compression is not the one starts from the loosest state according to the concept of proportional paths and asymptotic state of granular material by Goldscheider [21] and Gudehus et al. [24], as illustrated in Fig. 2.19 and Fig. 4.2b.

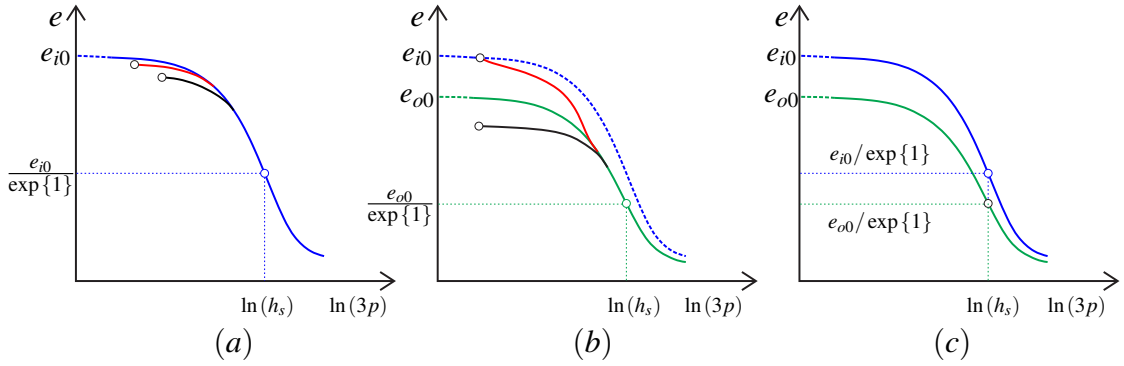

Figure 4.2: Ideal isotropic compression and ideal oedometric compression: (a) ideal isotropic compression and the asymptotic state; (b) ideal oedometric compression and the asymptotic state; (c) characteristics of ideal compression curves.

If the isotropic and oedometric compression tests are loaded up to stress levels which over the solid hardness, the inflection points as mentioned in Chapter 3 can be detected. Therefore the inflection point can be used to determine the value of solid hardness and the initial void ratio of ideal isotropic compression and ideal oedometric compression can be back calculated from the Eq. (3.27) and Eq. (3.28) directly.

From the Fig. 3.17, it can be seen that the value of initial void ratio of ideal isotropic compression has no strong difference from the one of the ideal oedometric compression. Considering the Dog's Bay sand has extremely great initial void ratio compares to the commonly sands, it can conclude that for common sand, the difference between the two initial void ratios should be relatively small.

A really good example of calibration is the determination of h_s and n for Karlsruhe sand. As it is shown in Fig. 4.3, three set of data from oedometric compression tests with different initial densities show similarity: the compression curves are similar in shape, and all three curves approach to a unique curve, the ideal oedometric compression curve as mentioned in Chapter 3. If the experimental data with $e_0 = 1.07$ is used for calibration of h_s and n, the best fit for the experimental data leads to a set of $h_s = 190$ MPa, $n = 0.4$ and $e_{o0} = 1.08$. While if considering the last five points of the experimental data with the e_0 reached the asymptotic oedometric state–the ideal oedometric compression line, then the best fit for these five points lead a combination of parameters as $h_s = 250$ MPa, $n = 0.7$ and $e_{o0} = 0.82$. Of course, it is uncertain whether the last five points chosen for calibration really reached the asymptotic state (the ideal oedometric compression line) or not, a further investigation

considering loading the Karlsruhe sand sample up to relative high stress level, high enough to reach the point of inflection, might be an appropriate solution for this question.

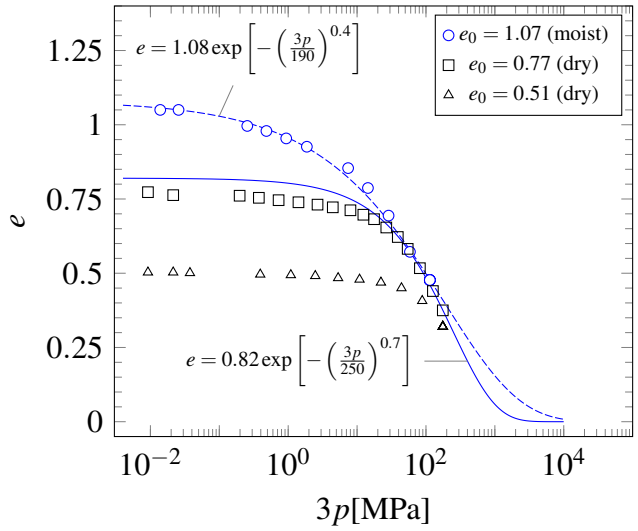

Figure 4.3: Determination of h_s and n for Karlsruhe sand (oedometric experimental results from Bauer [6]): $h_s = 190$ MPa and $n = 0.4$ by assuming the moist curve is the ideal oedometric curve; $h_s = 250$ MPa and $n = 0.7$ by assuming the last five points of $e_0 = 0.77$ curve reached the asymptotic state (ideal oedometric curve).

The reason to emphasize the difference between using ideal isotropic compression data and ideal oedometric compression data to determine the h_s, n and e_{i0} is that one should be familiar with the definitions of the parameters and the physical meaning of them as well.

Herle and Gudehus [27] proposed another method to determine the solid hardness h_s and n, note that as the authors mentioned this method is only valid for a certain stress range, normally only the stress range used for calibration. The calibrate results show that the determined values of h_s of different materials are extremely greater than the ones calibrated according to the method mentioned above in this subsection (see Fig. 4.3). Bauer et al. [13] proposed an extended compression relation with considering the solid hardness as a pressure dependent quantity, which can be used to explain the reason why the calibrated value of h_s with the method suggested by Herle and Gudehus [27] is greater than the one by Bauer [6]. Note that the definition of h_s (as a crushability resistance of the whole grain skeleton) mentioned in Chapter 3 is not valid for the equation proposed by Bauer et al. [13].

Another method of determination of h_s and n is proposed by Herle and Gudehus [27], and the comparison with experiments shows the determination method

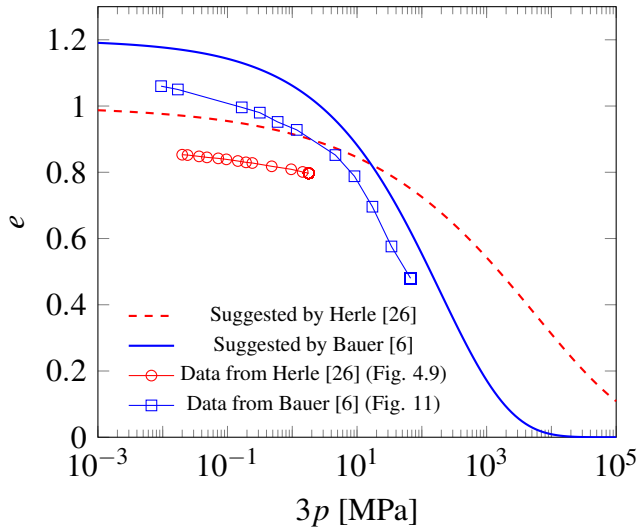

Figure 4.4: Comparison between the calibrated h_s from Herle and Gudehus [27] and Bauer [6]. The markers are oedometric compression test results, and the dashed and solid lines are the compression curves according to the calibration results by Comparison between the calibrated h_s from Herle and Gudehus [27] and Bauer [6], respectively.

The experimental investigation has a certain orientation that cannot guarantee the outcome of the investigation fits all the requirements which are need for calibration of the model. That is the main reason the simple constitutive model with simple calibration requirements is always we pursuing for. While, the simple does not mean it is only for the sake of simplicity. Comprehensive concept with clear definition can be interpreted to simple as well. Therefore, for the application point of view, it is better to insist to consider the compression relation which works well for general cases of granular materials, instead of choosing a (simplified) version which only for a special case or a specific pressure range.

4.3.2 Critical friction angle φ_c

According to the definition of critical state described by Schofield and Wroth [81], when the granular body reaches a critical state, the stress rate vanishes while the volumetric strain keeps constant. The mathematical description of critical state can be written as $\dot{\mathbf{T}} = \mathbf{0}$ and $\mathrm{tr}(D) = 0$. For axisymmetric compression condition (axial stress is T_{11}), the mobilized friction angle φ_{mob} can be represented as:

$$\varphi_{mob} = \arcsin\left(\frac{T_{11} - T_{22}}{T_{11} + T_{22}}\right) \tag{4.15}$$

When the critical state is reached, the asymptotic value of mobilized friction angle should be approached as well. Therefore, for the critical state, the $\varphi_{mob} = \varphi_c$ should be fulfilled. Thus, the critical friction angle can be determined from the data of conventional laboratory shear tests (i.e. drained/undrained triaxial compression test, direct shear test).

Herle [26] and Herle and Gudehus [27] discussed a method [2] that using the angle of repose to determine the critical friction angle of a dry granular material, as shown in Fig. 4.5.

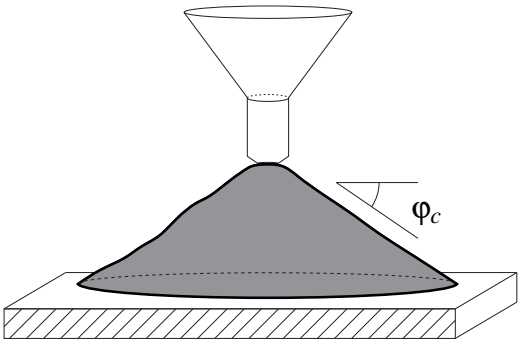

Figure 4.5: Determination of critical friction angle from the angle of repose, redrawn after Herle and Gudehus [27].

In this study, it is suggested to calibrate the friction angle according to the experimental data of shear tests. As it was compared by Herle and Gudehus [27], the prediction of critical friction angle of sands according to the angle of repose might have a deviation around one degree, and it is acceptable for the first estimation of material like sand. While for coarse material it is difficult to determine the angle of repose.

4.3.3 Critical void ratio e_c

Like it is discussed in the subsection above, when the material reaches the critical state, the volumetric strain rate vanishes simultaneously with the vanishing of stress rate. In the shear test, the specimens with different initial densities (initially loose and initial dense) from the same pressure level (p_0) approach to the same critical state (e_c and p_c) asymptotically. And the slopes of the shear compression curves are perpendicular to horizontal axis in the e-$\ln(p)$ space, as illustrated in Fig. 4.6.

Therefore, if h_s and n were given, with single shear test which reached the critical state the initial value of critical void ratio can be calculated according to the Eq. (2.24) directly. If the values of h_s and n were not given, then a set of shear tests which start from different stress level is required to calibrate the h_s, n and e_{c0}.

[2] It is mentioned in the study that the method is proposed by Cornforth in 1973.

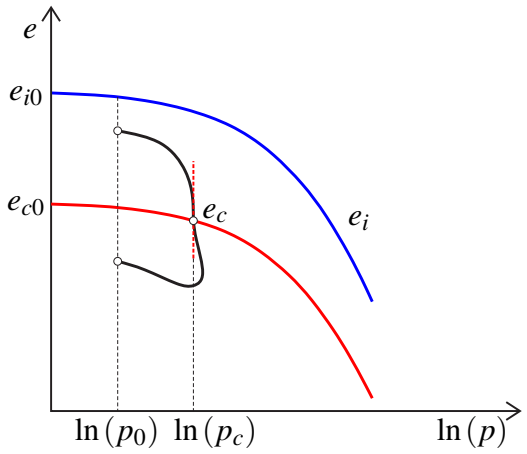

Figure 4.6: Determination of the initial value of critical void ratio

4.3.4 Parameter ǎ

Parameter α in this model is a factor related to relative density. For relative dense material, the value of α affects the location of peak state of the material in stress-strain space, i.e. φ_c-ε_{11}. Take the one of the conventional triaxial compression test in Soil Mechanics as an example, $\dot{T}_{22} = \dot{T}_{33} = 0$, the corresponding value of void ratio at the peak state, e_p, is illustrated in Fig. 4.7.

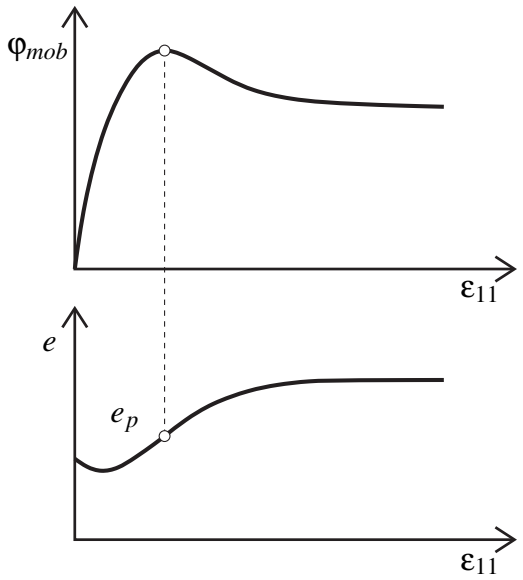

Figure 4.7: Determination of the parameter α according to the peak state

Thus, the parameter α can be derived as

$$\check{\alpha} = \frac{\ln\left\{\dfrac{-\hat{a}^2\left(D_{11}+2D_{22}\right)-\left(\hat{T}_{11}D_{11}+2\hat{T}_{22}D_{22}\right)}{\hat{a}\sqrt{D_{11}^2+2D_{22}^2}}\right\}}{\ln\left(\dfrac{e_p}{e_c}\right)} \tag{4.16}$$

4.3.5 Parameter β

The increase in the incremental stiffness with a decrease in the void ratio is taken account into the model by the stiffness factor $\check{f}_s$ (Bauer [6]). For isotropic compression starts from isotropic state, the following relation can be derived from the Eq. (4.1) without considering degradation of h_s

$$3\dot{p} = -\left(\frac{e_i}{e}\right)^{\beta}\frac{1+e_i}{ne_i\check{h}_i}\left(\frac{3p}{h_s}\right)^{-n} p\left\{3\hat{a}^2+1-\sqrt{3}\left(\frac{e}{e_c}\right)^{\check{\alpha}}\hat{a}\right\}\frac{\dot{e}}{1+e} \tag{4.17}$$

In order to estimate the constant parameter β in Eq. (4.12), an isotropic compression with an initial void ratio e_0 is considered here (as shown in Fig. 4.8, $e_0 < e_i$). The angle ϕ can be represented as $d\left(3p\right)/de = \tan\phi$, therefore, the relation for β can be derived explicitly as

$$\beta = \frac{\ln\left\{\dfrac{-ne_i\check{h}_i\left(1+e_0\right)\tan\phi}{\left(1+e_i\right)p_0\left[3\hat{a}^2+1-\sqrt{3}\hat{a}\left(e_0/e_c\right)^{\check{\alpha}}\right]}\left(\dfrac{3p_0}{h_s}\right)^{n}\right\}}{\ln\left(\dfrac{e_i}{e_0}\right)} \tag{4.18}$$

It is found by numerical simulation that with $\beta = 1$ sufficient accurate can be archived. Therefore, $\beta = 1$ is considered in this thesis. Thus, only nine parameters are required for the simplified constitutive model.

4.4 Constitutive equations for element tests

For validation of a constitutive model proposed (or newly developed, simplified, extended), element test is one of the best solutions[3]. The element tests according to the simplified

[3] Another useful tool is the so-called *response envelope*. For details about response envelope, one can refer to Wu and Kolymbas [98] and Gudehus and Mašín [23].

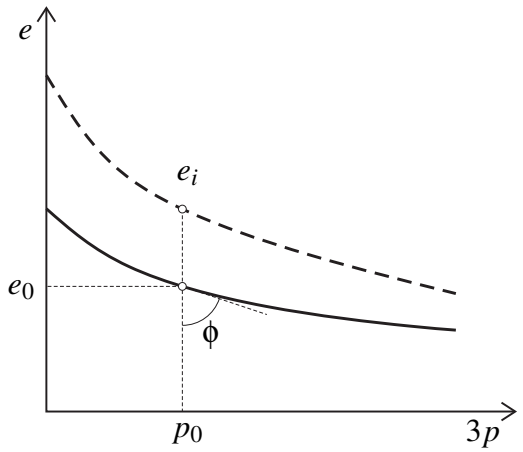

Figure 4.8: Determination of parameter β from isotropic compression test

model mentioned in Section 4.1 are simulated using a hypoplastic element test (HET[4]) program (see Appendix A.3).

In the current version of HET, the element test library includes the following tests:

- Compression tests:
  - Isotropic compression test
  - Oedometric compression test
  - Triaxial compression test
  - Biaxial compression test
- Creep tests:
  - True-triaxial-creep test[5]
  - Oedometric-creep test
  - Biaxial-creep test

[4] Actually, it is my supervisor Prof. E. Bauer's idea to develop this private program. In the course of calibration of different materials based on the available experimental data, the benefits of the program become more and more apparent. Another recommended automation method is the batch processing and automated processing of data based on Abaqus using Python scripts.

[5] This test actually includes the isotropic compression test under creep deformation condition as well. In fact that the isotropic compression test is one special true triaxial compression test.

As in this study only rectilinear stretching is covered, the objective stress rate tensor $\mathring{\mathbf{T}}$ can be replaced with $\dot{\mathbf{T}}$. Therefore the constitutive equation considered later in this work is described in the $\dot{\mathbf{T}}$ form and the reference equations can be written as:

$$\dot{\mathbf{T}} = f_s \left\{ \hat{a}^2 \mathbf{D} + \mathrm{tr}\left(\hat{\mathbf{T}}\mathbf{D}\right)\hat{\mathbf{T}} + f_d \hat{a} \left(\hat{\mathbf{T}} + \hat{\mathbf{T}}^*\right) \|\mathbf{D}\| \right\} \tag{4.19}$$

and

$$\dot{\mathbf{T}} = f_s \left\{ \hat{a}^2 \mathbf{D} + \mathrm{tr}\left(\hat{\mathbf{T}}\mathbf{D}\right)\hat{\mathbf{T}} + f_d \hat{a} \left(\hat{\mathbf{T}} + \hat{\mathbf{T}}^*\right) \|\mathbf{D}\| \right\} + \frac{\dot{h}_{st}}{h_{st}} \left\{ \frac{1}{3}\mathrm{tr}\left(\mathbf{T}\right)\mathbf{I} + \kappa \mathbf{T}^* \right\} \tag{4.20}$$

for dry/wet and stiffness degradation conditions, respectively.

Isotropic compression

The boundary condition of the isotropic compression test can be described as $D_{11} = D_{22} = D_{33}$. Therefore, the stretching tensor can be represented as

$$\mathbf{D} = \frac{1}{3}\mathrm{tr}\left(\mathbf{D}\right)\mathbf{I} \tag{4.21}$$

For compression condition, $D_{11} < 0$ leads $\mathrm{tr}\left(\mathbf{D}\right) < 0$. Thus the constitutive equation can be written as

$$\dot{\mathbf{T}} = \check{f}_s \left\{ \hat{a}^2 \mathbf{I} + \mathrm{tr}\left(\hat{\mathbf{T}}\right)\hat{\mathbf{T}} - \sqrt{3}\check{f}_d \hat{a} \left(\hat{\mathbf{T}} + \hat{\mathbf{T}}^*\right) \right\} \frac{1}{3}\mathrm{tr}\left(\mathbf{D}\right) \tag{4.22}$$

As it is described in Eq. (4.22), with a given initial stress tensor $\mathbf{T}$, the stress rate tensor $\dot{\mathbf{T}}$ can be derived directly according to Eq. (4.22) with a specified stretching tensor $\mathbf{D}$. With a specified time step Δt and total time step n, the strain increment[6] can be described as $\Delta\epsilon_{ij} = D_{ij}\Delta t$ and the total strain (maximum strain) reads $\epsilon_{ij} = D_{ij} n \Delta t$.

[6]The main reason we consider the simple strain increment method is we insist to keep the element test program as simple as it is, that for readers who have no numerical simulation background can handle the element test as well. And the simpler numerical simulation method used, the less computer capacity is required.

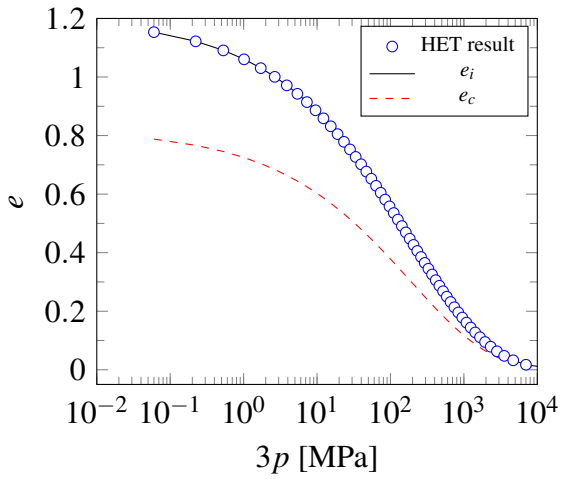

Figure 4.9: Ideal isotropic compression result from HET

Oedometric compression

The boundary condition of the oedometric compression test can be described as $D_{11} < 0$ and $D_{22} = D_{33} = 0$. Therefore, the trace of stretching tensor is $\mathrm{tr}(\mathbf{D}) = D_{11} < 0$ and $\|\mathbf{D}\| = -D_{11}$. Thus, the stress rates can be represented as follows:

$$\dot{T}_{11} = \check{f}_s \left\{ \hat{a}^2 + \hat{T}_{11}^2 - \check{f}_d \hat{a} \left(\hat{T}_{11} + \hat{T}_{11}^* \right) \right\} \mathrm{tr}(\mathbf{D}) \tag{4.23}$$

$$\dot{T}_{22} = \check{f}_s \left\{ \hat{T}_{11} \hat{T}_{22} - \check{f}_d \hat{a} \left(\hat{T}_{22} + \hat{T}_{22}^* \right) \right\} \mathrm{tr}(\mathbf{D}) \tag{4.24}$$

$$\dot{T}_{33} = \check{f}_s \left\{ \hat{T}_{11} \hat{T}_{33} - \check{f}_d \hat{a} \left(\hat{T}_{33} + \hat{T}_{33}^* \right) \right\} \mathrm{tr}(\mathbf{D}) \tag{4.25}$$

Then the rate of mean pressure can be derived according to $\dot{p} = -\mathrm{tr}\left(\dot{\mathbf{T}}\right)/3$. Therefore, considering Eq. (4.23), Eq. (4.24) and Eq. (4.25), the rate of mean pressure can be represented as

$$\dot{p} = -\frac{1}{3} \check{f}_s \left\{ \hat{a}^2 + \hat{T}_{11} - \check{f}_d \hat{a} \right\} \mathrm{tr}(\mathbf{D}) \tag{4.26}$$

here, the $\check{f}_s$ is a quantity with a positive value, $\mathrm{tr}(\mathbf{D})$ is negative. Thus, the sign of the component $\hat{a}^2 + \hat{T}_{11} - \check{f}_d \hat{a}$ determines whether the mean pressure rate is positive or not.

Paths from ideal isotropic compression to ideal oedometric compression.

Recalling that in Chapter 3, a special case of oedometric compression which states from an ideal isotropic initial condition is mentioned. More specific, considering a granular assembly has an initial stress state that $T_{11} = T_{22} = T_{33}$ and with the initial void ratio equals to the maximum limit void ratio at this stress level, $e_0 = e_i$, with applying the oedometric compression condition the void ratio will approach to the ideal oedometric compression curve of the granular body. And in Fig. 3.16b, a possible compression curve is illustrated that during compression the reduction of mean pressure might occur.

Back to the Eq. (4.26), for this special case mentioned above, $\hat{T}_{11} = 1/3$, $\check{f}_d = (e_{i0}/e_{c0})^{\check{\alpha}}$ and as it is mentioned in Eq. (2.23) that $\hat{a}_i = \sqrt{8/3}\sin\varphi_c/(3-\sin\varphi_c)$, the Eq. (4.26) can be written as

$$\dot{p} = -\frac{1}{9}\check{f}_s \left\{ 8\left(\frac{\sin\varphi_c}{3-\sin\varphi_c}\right)^2 + 1 - 2\sqrt{6}\left(\frac{e_{i0}}{e_{c0}}\right)^{\check{\alpha}}\left(\frac{\sin\varphi_c}{3-\sin\varphi_c}\right)\right\}\mathrm{tr}(\mathbf{D}) \tag{4.27}$$

Set $x = \sin\varphi_c/(3-\sin\varphi_c)$, $\check{f}_{di} = (e_{i0}/e_{c0})^{\check{\alpha}}$ and $y = 8x^2 - 2\sqrt{6}\check{f}_{di}x + 1$, Eq. (4.27) can be represented as:

$$\dot{p} = -\frac{1}{9}\check{f}_s y\,\mathrm{tr}\mathbf{D} \tag{4.28}$$

Thus when $y < 0$, the condition of $\dot{p} < 0$ might exist, which can be proved with following steps:

At first, according to the definition of x, it can conclude that $x \in [0, 0.5]$. In particular, when $\sin\varphi_c = 0$, x reaches the minimum value, $x_{min} = 0$; and for $\sin\varphi_c = 1$, x reaches the maximum value, $x_{max} = 0.5$.

The quadratic equation $y = y(x)$ can only have one solution for the case $y = 0$ with providing $\check{f}_{di} = 2\sqrt{3}/3$, and the single solution of the quadratic equation $y = 0$ is $x = \sqrt{2}/4$. That means when $\varphi_c = 51.62^\circ$ and $\check{f}_{di} = (e_{i0}/e_{c0})^{\check{\alpha}} = 2\sqrt{3}/3$, the $\dot{p} = 0$ and the initial direction of the oedometric compression curve, which starts from the ideal isotropic state, is perpendicular to the horizontal axis of the e-$\ln(3p)$ space, as shown in Fig. 4.10b.

For the case that $\check{f}_{di} < 2\sqrt{3}/3$, one solution of $y = 0$ exists and $y > 0$. Therefore, the start point of the aforementioned compression curve will have a direction which has $\dot{p} > 0$ in the e-$\ln(3p)$ space (see Fig. 4.10a).

Considering the $\check{f}_{di} < 2\sqrt{3}/3$, two solutions of $y = 0$ might exist in the range $x \in [0, 0.5]$. And if the following condition

$$\frac{2\sqrt{6}\check{f}_{di} - \sqrt{24\check{f}_{di}^2 - 32}}{16} < x < \frac{2\sqrt{6}\check{f}_{di} + \sqrt{24\check{f}_{di}^2 - 32}}{16} \tag{4.29}$$

exists, the rate of mean pressure of the initial point can be negative, as illustrated in Fig. 4.10c. Thus, the compression curve will first toward to left-hand-side. Considering the asymptotic state concept, with this condition, the mean pressure will first reduce and then increase with the compression deformation increases. For example, considering a specimen with $\check{f}_{di} = 1.3536$ and a critical friction angle $\varphi_c = 30^\circ$, the situation of $\dot{p} < 0$ will happen.

Note here the discussion is based on the strain controlled loading condition. The stress-controlled loading condition is not covered in this work. Therefore, it can be concluded that using the simplified constitutive model, it is possible to simulate compression curve as illustrated in Fig. 3.16b.

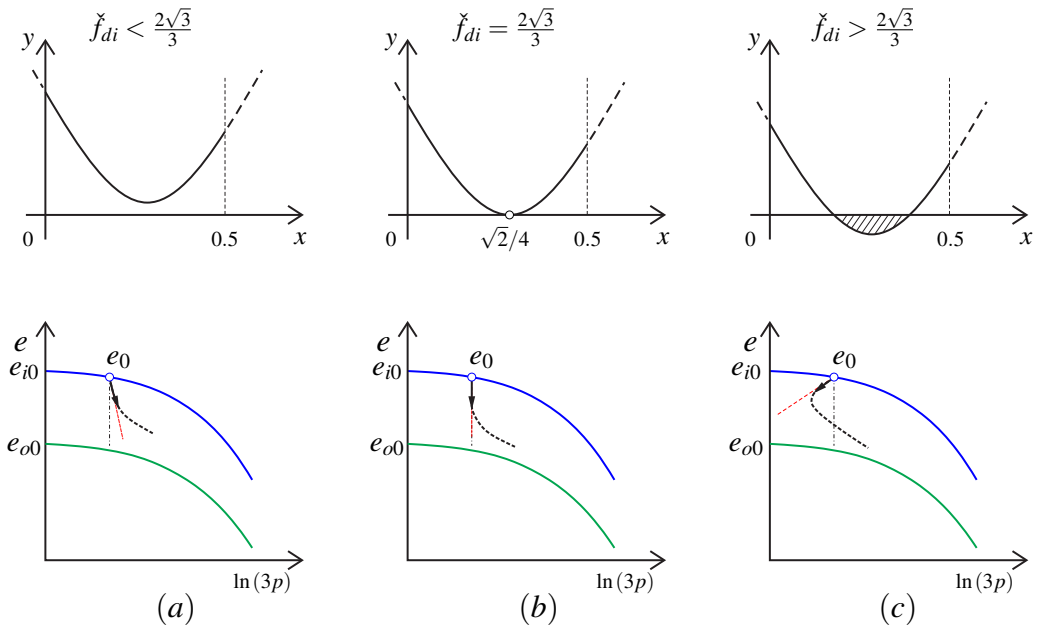

Figure 4.10: Different paths from initially ideal isotropic state to asymptotic state of oedometric compression curve: (a) with $\check{f}_{di} < 2\sqrt{3}/3$; (b) with $\check{f}_{di} = 2\sqrt{3}/3$ and $\varphi_c = 51.62°$; (c) with $\check{f}_{di} > 2\sqrt{3}/3$.

K_0 state Another interesting topic related to the concept of K_0 state and the concept of critical state will be discussed in this part. Before starting the discussion related to the critical state, the analytic solution of $\hat{a}$ of the oedometric compression condition is given by following steps:

The constitutive equation for oedometric condition describe in Eq. (4.23) - Eq. (4.25) can be represented as follows

$$\dot{T}_{11} = \check{f}_s \left\{ \hat{a}_o^2 + \frac{1}{(1+2K)^2} - \check{f}_d \hat{a}_o \frac{5-2K}{3(1+2K)} \right\} \mathrm{tr}(\mathbf{D}) \tag{4.30}$$

$$\dot{T}_{22} = \dot{T}_{33} = \check{f}_s \left\{ \frac{K}{(1+2K)^2} - \check{f}_d \hat{a}_o \frac{4K-1}{3(1+2K)} \right\} \mathrm{tr}(\mathbf{D}) \tag{4.31}$$

here $\hat{a}_o = \sqrt{8/3}\sin\varphi_c / (3 - \sin\varphi_c)$, details can be referred to Appendix A.4. The K_0 state can be described as the ratio of horizontal stress to vertical stress is constant, which is conventionally denoted as K_0. Therefore, consider the stress ratio is constant, $K = K_0$, the stress ratio can be represented as

$$\frac{\dot{T}_{22}}{\dot{T}_{11}} = \frac{3K_0 - f_{do}\hat{a}_o(4K_0 - 1)(1+2K_0)}{3\hat{a}_o^2(1+2K_0)^2 + 3 - f_{do}\hat{a}_o(5-2K_0)(1+2K_0)} \tag{4.32}$$

here the additional subscript "o" is used to emphasize the stiffness factor for oedometric condition.

In order to fulfill the requirement of K_0 state, the stress rate ratio should equal to K_0 as well. Thus, the Eq. (4.32) can be written as

$$K_0 = \frac{3K_0 - f_{do}\hat{a}_o\,(4K_0 - 1)\,(1 + 2K_0)}{3\hat{a}_o^2\,(1 + 2K_0)^2 + 3 - f_{do}\hat{a}_o\,(5 - 2K_0)\,(1 + 2K_0)} \tag{4.33}$$

which requires the following relation of K_0 and f_{do}

$$K_0 = \frac{f_{do}}{3\hat{a}_o + f_{do}} \tag{4.34}$$

or in another representation

$$f_{do} = \frac{3\hat{a}_o K_0}{1 - K_0} \tag{4.35}$$

As $f_{do} = (e_o/e_c)^{\alpha}$, and with regards to the fact that the oedometric compression reaches the ideal odeometric compression state when the requirement of K_0 state is fulfilled, the e_o can be calculated according to Eq. (3.29). Considering the well-accepted Jáky's function

$$K_{0J} = 1 - \sin\varphi_c \tag{4.36}$$

Substitution of the Eq. (4.36) into the Eq. (4.35) leads to

$$f_{do} = 2\sqrt{6}\left(\frac{1 - \sin\varphi_c}{3 - \sin\varphi_c}\right) \tag{4.37}$$

However, in this constitutive model K_0 state cannot be fulfilled. Set of numerical simulation results indicate that the oedometric compression approach to asymptotic state while during the compression K_o does not keep constant (see Fig. 4.11).

As it is shown in Fig. 4.11, the effect of initial stress ratio vanishes after reaching a stress level around $T_{11} = -0.2$ MPa. After reached the asymptotic state, the K_h stays close to a value 0.53 approximately. From these two simulation, it can be seen that for first approximation, it is acceptable to consider $K_{0J} = 1 - \sin\varphi_c$ for prescribing the oedometric stress state. Note that in this model, the stress ratio of T_{22} and T_{11} of oedometric test (K_h) is not predefined and it derives automatically according to the constitutive equation. In addition, in the stress space like T_{11}-T_{22} (illustrated in Fig. A.2) or Rendulic plane (as in Gudehus and Mašín [23]), the oedometric path described by the constitutive equation is not a straight line.

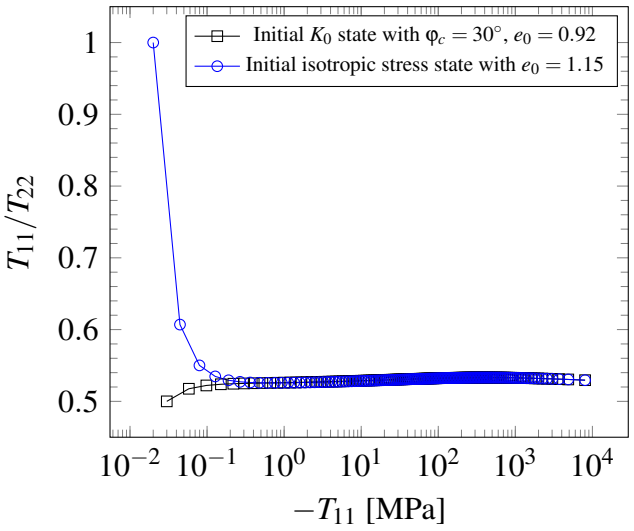

Figure 4.11: Numerical simulation of oedometric compression starting from isotropic state and K_{oJ} state with $p_0 = 0.02$ MPa and constitutive parameter from Table **??**.

Triaxial compression

In the current version of HET, a conventional triaxial compression test with constant lateral stresses condition is considered. In addition, different from the conventional soil mechanic triaxial laboratory test, the triaxial compression element test in HET is not restrict to the axisymmetric stress condition. In another word, different initial lateral stresses is taken into account to the element test as well. Therefore, the triaxial compression element test in HET is designed for the true triaxial compression test with constant lateral stresses. Then the boundary condition of the triaxial compression element test in HET is

$$\dot{T}_{22} = \dot{T}_{33} = 0 \tag{4.38}$$

For this element test, the explicit representation of stress components are given as follows:

$$\dot{T}_{11} = \check{f}_s \left\{ \hat{a}^2 D_{11} + \left(\hat{T}_{11} D_{11} + \hat{T}_{22} D_{22} + \hat{T}_{33} D_{33} \right) \hat{T}_{11} + \check{f}_d \hat{a} \left(\hat{T}_{11} + \hat{T}^*_{11} \right) \sqrt{D^2_{11} + D^2_{22} + D^2_{33}} \right\} \tag{4.39}$$

$$\dot{T}_{22} = \check{f}_s \left\{ \hat{a}^2 D_{22} + \left(\hat{T}_{11} D_{11} + \hat{T}_{22} D_{22} + \hat{T}_{33} D_{33} \right) \hat{T}_{22} + \check{f}_d \hat{a} \left(\hat{T}_{22} + \hat{T}^*_{22} \right) \sqrt{D^2_{11} + D^2_{22} + D^2_{33}} \right\} \tag{4.40}$$

$$\dot{T}_{33} = \check{f}_s \left\{ \hat{a}^2 D_{33} + \left(\hat{T}_{11} D_{11} + \hat{T}_{22} D_{22} + \hat{T}_{33} D_{33} \right) \hat{T}_{33} + \check{f}_d \hat{a} \left(\hat{T}_{33} + \hat{T}^*_{33} \right) \sqrt{D^2_{11} + D^2_{22} + D^2_{33}} \right\} \tag{4.41}$$

Strain-controlled loading procedure is considered for the triaxial element test as well. Then, with given axial stretching, D_{11}, and an appropriate iteration method, the stretching components D_{22} and D_{33} can be predicted based on the Eq. (4.39)-Eq. (4.41).

In this element test, the numerical simulation ends up with solving a 2-dimensional equation system:

$$\mathbf{f}(\mathbf{x}) = \mathbf{0} \tag{4.42}$$

here $\mathbf{x} = \begin{bmatrix} D_{22} & D_{33} \end{bmatrix}^T$ and $\mathbf{f} = \begin{bmatrix} \dot{T}_{22} & \dot{T}_{33} \end{bmatrix}^T$. Then the Jacobian matrix of $\mathbf{f}$, $\mathbf{J_f}(\mathbf{x})$, is a 2×2 matrix

$$\mathbf{J_f}(\mathbf{x}) = \begin{bmatrix} \frac{\partial \dot{T}_{22}}{\partial D_{22}} & \frac{\partial \dot{T}_{22}}{\partial D_{33}} \\ \frac{\partial \dot{T}_{33}}{\partial D_{22}} & \frac{\partial \dot{T}_{33}}{\partial D_{33}} \end{bmatrix} \tag{4.43}$$

and the matrix representation of $\mathbf{f}$ with respect to Jacobian matrix reads

$$\begin{bmatrix} \frac{\partial \dot{T}_{22}}{\partial D_{22}} & \frac{\partial \dot{T}_{22}}{\partial D_{33}} \\ \frac{\partial \dot{T}_{33}}{\partial D_{22}} & \frac{\partial \dot{T}_{33}}{\partial D_{33}} \end{bmatrix} \begin{bmatrix} \Delta D_{22} \\ \Delta D_{33} \end{bmatrix} = \begin{bmatrix} \Delta \dot{T}_{22} \\ \Delta \dot{T}_{33} \end{bmatrix} \tag{4.44}$$

Therefore a simple iteration method can be considered for finding the root of the Eq. 4.42. In order to keep the program as simple as it can be, the well-known Newton-Raphson iteration method is adopted. Note the iteration speed or results are highly depending on the quality of prediction of unknowns for the first iteration. For this triaxial element test, it is suggested to choose a set of values close to zeros.

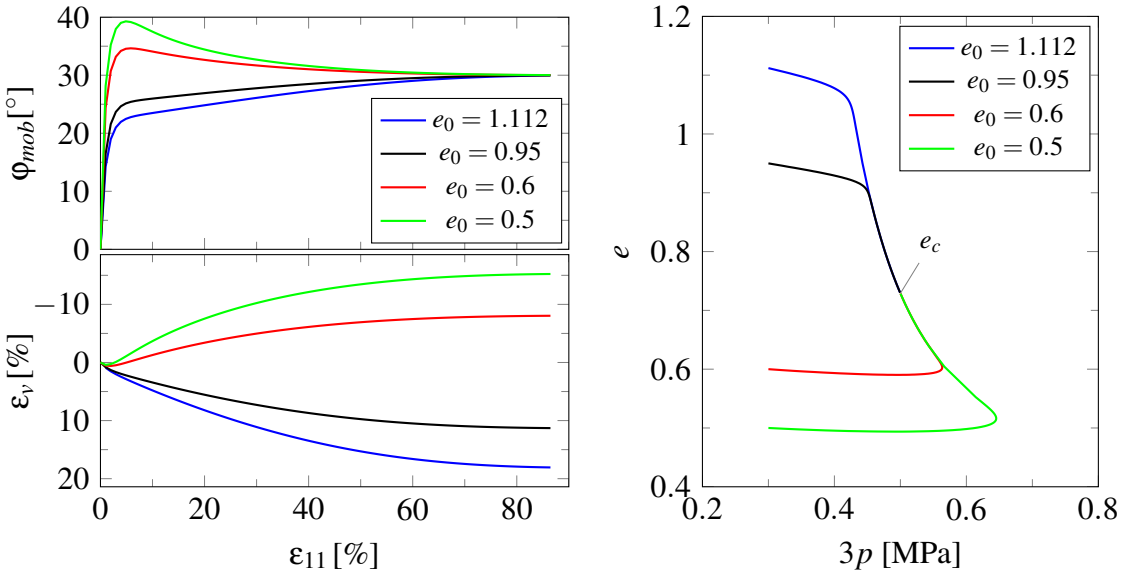

(a) Stress-strain behaviour and critical state

(b) Density independency in e-$3p$ space

Figure 4.12: Triaxial compression test with different initial void ratios

A set of element tests, with same initial stresses, $T_{11} = T_{22} = T_{33} = -0.1$ MPa and different initial void ratios, are loaded up to critical state and the results are summarized in Fig. 4.12. The results indicate tests with different initial void ratio but same initial stresses reach the same void ratio at the critical state (Fig. 4.12b).

Biaxial compression

The boundary conditions of biaxial compression are

$$T_{22} = \text{const.} \quad \left(\text{or } \dot{T}_{22} = 0\right) \tag{4.45}$$

and

$$D_{33} = 0 \tag{4.46}$$

Therefore, the explicit equations of biaxial compression element test read

$$\dot{T}_{11} = \check{f}_s \left\{ \hat{a}^2 D_{11} + \left(\hat{T}_{11} D_{11} + \hat{T}_{22} D_{22}\right) \hat{T}_{11} + \check{f}_d \hat{a} \left(\hat{T}_{11} + \hat{T}^*_{11}\right) \sqrt{D^2_{11} + D^2_{22}} \right\} \tag{4.47}$$

$$\dot{T}_{22} = \check{f}_s \left\{ \hat{a}^2 D_{22} + \left(\hat{T}_{11} D_{11} + \hat{T}_{22} D_{22}\right) \hat{T}_{22} + \check{f}_d \hat{a} \left(\hat{T}_{22} + \hat{T}^*_{22}\right) \sqrt{D^2_{11} + D^2_{22}} \right\} = 0 \tag{4.48}$$

$$\dot{T}_{33} = \check{f}_s \left\{ \left(\hat{T}_{11} D_{11} + \hat{T}_{22} D_{22}\right) \hat{T}_{33} + \check{f}_d \hat{a} \left(\hat{T}_{33} + \hat{T}^*_{33}\right) \sqrt{D^2_{11} + D^2_{22}} \right\} \tag{4.49}$$

From the Eq. (4.47)-Eq. (4.49), only unknown D_{22} need to calculate according to the requirement of boundary condition $\dot{T}_{22} = 0$. Let $x = D_{22}$ be the unknown and $f(x) = \dot{T}_{22}$ be the function. In the current version of HET, Newton-Raphson iteration method is used for solving this one-dimensional equation $f(x)$, with an initial estimation of x (D_{22}) set to a number close to zero. Numerical simulation of biaxial compression test shows similar results as the ones from triaxial compression test.

Creep tests

Creep test for triaxial condition For triaxial compression test with creep deformation, the boundary condition can be described as

$$\dot{\mathbf{T}} = \mathbf{0} \tag{4.50}$$

and the explicit constitutive equations read

$$\dot{T}_{11} = \check{f}_s \left\{ \hat{a}^2 D_{11} + \left(\hat{T}_{11} D_{11} + \hat{T}_{22} D_{22} + \hat{T}_{33} D_{33}\right) \hat{T}_{11} + \check{f}_d \hat{a} \left(\hat{T}_{11} + \hat{T}^*_{11}\right) \sqrt{D^2_{11} + D^2_{22} + D^2_{33}} \right\} + \frac{\dot{h}_{st} \left(T_{11} + T_{22} + T_{33}\right)}{3 h_{st}} = 0 \tag{4.51}$$

$$\dot{T}_{22} = \check{f}_s \left\{ \hat{a}^2 D_{22} + \left(\hat{T}_{11} D_{11} + \hat{T}_{22} D_{22} + \hat{T}_{33} D_{33} \right) \hat{T}_{22} + \check{f}_d \hat{a} \left(\hat{T}_{22} + \hat{T}_{22}^* \right) \sqrt{D_{11}^2 + D_{22}^2 + D_{33}^2} \right\} + \frac{\dot{h}_{st} \left(T_{11} + T_{22} + T_{33} \right)}{3 h_{st}} = 0 \quad (4.52)$$

$$\dot{T}_{33} = \check{f}_s \left\{ \hat{a}^2 D_{33} + \left(\hat{T}_{11} D_{11} + \hat{T}_{22} D_{22} + \hat{T}_{33} D_{33} \right) \hat{T}_{33} + \check{f}_d \hat{a} \left(\hat{T}_{33} + \hat{T}_{33}^* \right) \sqrt{D_{11}^2 + D_{22}^2 + D_{33}^2} \right\} + \frac{\dot{h}_{st} \left(T_{11} + T_{22} + T_{33} \right)}{3 h_{st}} = 0 \quad (4.53)$$

The numerical simulation is related to solve a 3-dimensional equation system:

$$\mathbf{f}(\mathbf{x}) = \mathbf{0} \quad (4.54)$$

with $\mathbf{x} = \begin{bmatrix} D_{11} & D_{22} & D_{33} \end{bmatrix}^T$ and $\mathbf{f} = \begin{bmatrix} \dot{T}_{11} & \dot{T}_{22} & \dot{T}_{33} \end{bmatrix}^T$ and a 3×3 Jacobian matrix of $\mathbf{f}$, $\mathbf{J_f}(\mathbf{x})$:

$$\mathbf{J_f}(\mathbf{x}) = \begin{bmatrix} \dfrac{\partial \dot{T}_{11}}{\partial D_{11}} & \dfrac{\partial \dot{T}_{11}}{\partial D_{22}} & \dfrac{\partial \dot{T}_{11}}{\partial D_{33}} \\ \dfrac{\partial \dot{T}_{22}}{\partial D_{11}} & \dfrac{\partial \dot{T}_{22}}{\partial D_{22}} & \dfrac{\partial \dot{T}_{22}}{\partial D_{33}} \\ \dfrac{\partial \dot{T}_{33}}{\partial D_{11}} & \dfrac{\partial \dot{T}_{33}}{\partial D_{22}} & \dfrac{\partial \dot{T}_{33}}{\partial D_{33}} \end{bmatrix} \quad (4.55)$$

and the matrix representation of $\mathbf{f}$ with respect to Jacobian matrix reads

$$\begin{bmatrix} \dfrac{\partial \dot{T}_{11}}{\partial D_{11}} & \dfrac{\partial \dot{T}_{11}}{\partial D_{22}} & \dfrac{\partial \dot{T}_{11}}{\partial D_{33}} \\ \dfrac{\partial \dot{T}_{22}}{\partial D_{11}} & \dfrac{\partial \dot{T}_{22}}{\partial D_{22}} & \dfrac{\partial \dot{T}_{22}}{\partial D_{33}} \\ \dfrac{\partial \dot{T}_{33}}{\partial D_{11}} & \dfrac{\partial \dot{T}_{33}}{\partial D_{22}} & \dfrac{\partial \dot{T}_{33}}{\partial D_{33}} \end{bmatrix} \begin{bmatrix} \Delta D_{11} \\ \Delta D_{22} \\ \Delta D_{33} \end{bmatrix} = \begin{bmatrix} \Delta \dot{T}_{11} \\ \Delta \dot{T}_{22} \\ \Delta \dot{T}_{33} \end{bmatrix} \quad (4.56)$$

Note that the Eq. (4.51)-Eq. (4.53) are rate-dependent. Similar iteration procedure can be used but the time step Δt should be considered as the real time. For the creep test under biaxial or oedometric condition, the boundary conditions are different, while it is worth noting that the conventional biaxial-creep or oedometric-creep test is not a real creep test.

Creep test for biaxial condition The boundary condition for biaxial-creep can be described as

$$\dot{T}_{11} = \dot{T}_{22} = 0 \quad (4.57)$$

and

$$D_{33} = 0 \quad (4.58)$$

Thus, two unknowns, D_{11} and D_{22} need to be calculated. Considering the similarity in mathematical description and iteration procedure for other element tests mentioned above, the details of this element test and the oedometric-creep test are not given here.

Creep test for oedometric condition The mathematical expression for the boundary conditions of oedometric-creep are

$$\dot{T}_{11} = 0 \tag{4.59}$$

$$D_{22} = D_{33} = 0 \tag{4.60}$$

Only one equation $\dot{T}_{11} = 0$ with one unknown, D_{11}, is required to solve for this condition.

5 Calibration of the constitutive parameters for a shale quartzite sand

For numerical simulation of geotechnical structures, first the calibration of the constitutive model used has to be carried out. To this end experimental data from laboratory element tests (isotropic, oedometric and triaxial compression tests) are used. Note the element tests are homogeneous element deformation test, which can be used for calibration and the validation of calibration as well. In this chapter, the application of the constitutive model aforementioned (in Chapter 4) based on the experimental data by Ovalle et al. [74] is outlined using the hypoplastic element test program (HET).

The outline of this chapter is as follow: the experimental study by Ovalle et al. [74] is summarized in Section 5.1; the calibration based on the study of Ovalle is detailed in Section 5.2.

5.1 Experiments by Ovalle et al. (2015)

Constitutive models are developed based on the results from experimental investigations and basics of continuum mechanics. Calibration of the material parameters involved in the constitutive model can be a challenging task in particular for weathered and moisture sensitive materials.

Ovalle et al. [74] investigated an angular sand under different conditions: dry, wet and wetting at a certain stress level of the initial dry specimen. In particular, the tested sand is obtained by grinding a quartzite shale rock from Trois Vallées quarry located in Orne, a department in the northwest of France. One of the main purposes of the study by the authors is evaluating the mechanical behaviour of the material with respect to the stiffness degradation induced by wetting. This study offers a valuable original source, which is used as an example for calibration in Section 5.2.

5.1.1 Characterization of the tested material and preparation of specimens

The tested material and the quartzite shale rock are shown in Fig. 5.1. After grinding, the solid grains are sieved and selected to prepare samples with a uniform initial grain size distribution (GSD) with the size range between 2 and 2.5 mm. The dry density of solid grains obtained from the shale rock is $\rho_d = 2.75e3\mathrm{kg/m}^3$. As it is shown in the Fig. 5.1b, the material before the test is angular and flat, which is vulnerable to crushing.

Electron microscope scans shows the original material, the shale rock is composed of thin sheets (see Fig. 5.2a right, and Fig. 5.2b left), which can be easily detached during the compression and essentially become the source of significant amount of fine grains produced during the test.

The grain size distribution analysis after tests shows that finer grains were produced by grain crushing. In addition, the grains finer than 0.08 mm were analyzed using X-ray diffraction (XRD), and the composition of the fine grains are tabulated in Table A.1 and Table A.2.

(a) Riprap of shale from Trois Vallées quarry (b) Grains of shale quartzite sand from the shale

Figure 5.1: The quartzite shale rock from Trois Vallées quarry and the angular sand from the grinding of the shale rock from Ovalle [73].

After grinding, the material was first air dried and then pluviated at low height into cylindrical moulds. Therefore, it can be concluded that the prepared specimens were relative loose and no grain crushing occurred during the preparation. One set of specimens were loaded continuously under dry condition, another set of specimens were saturated before compression or after a phase of compression. In this chapter, capital letter “D” and with a number is used for denoting the dry test, “S” for initially saturated test and “W” for the test was wetted during the compression.

Results of laboratory tests

Isotropic, oedometric and triaxial compression tests were conducted under different conditions: dry, saturated or initial dry and then saturated. A general overview of the test types are summarized in the Table 5.1. The test numbers introduced in the following are different from the ones in Ovalle et al. [74].

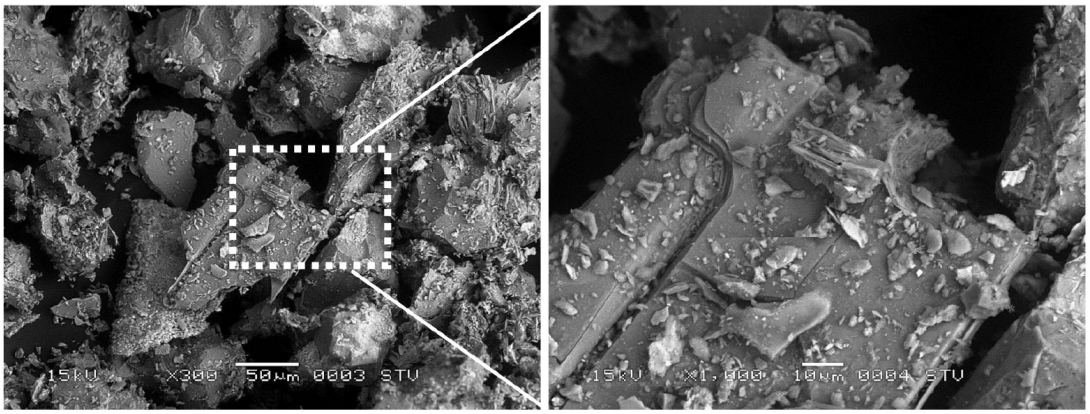

(a) Fine grains between 0.08 and 0.1 mm

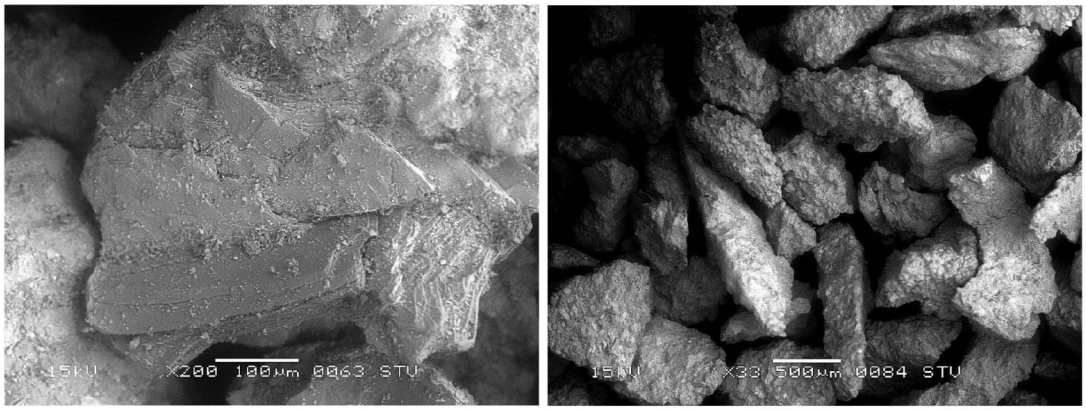

(b) Fine grains between 0.315 and 0.4 mm (left) and between 0.5 and 0.6 mm (right)

Figure 5.2: Electron microscope scans of fine fractions after oedometric compression test from Ovalle et al. [74].

Isotropic compression tests Two specimens, D1 and W2, were loaded up to 0.8 MPa. After reached the designed stress level, specimen of W2 was saturated. Summary of isotropic compression tests are tabulated in Table A.3.

The experimental results of isotropic compression tests, D1 and W2, and the isotropic compression phases before triaxial compression tests (D15, W16∼W20, D21 and W22) before wetting are plotted in Fig. 5.3.

It is shown in Fig. 5.3, each compression shows similar trend of compression curve. In addition, tests results of D1 and W2 lie above the other curves, which means the specimens of D1 and W2 have relative looser state comparing the other specimens. The grain size distribution (GSD) analysis of D1 and the one of W2 after wetting (see Fig. 5.4) shows that finer particles were detected in both tests, which indicates that even in relative low stress level the shale quartzite sand can be easily crushed. In addition, more fine particle can be

Table 5.1: General information of experimental investigation by Ovalle et al. [74]

Test type	Specimen size [mm] Height	Diameter	Loading type	$T_{11,max}$ [MPa]	T_{22} [MPa]
Isotropic	110	70	Stress-controlled	$-0.4, -0.8$	/
Oedometric	19	70	Stress-controlled	$-0.4 \sim -2.1$	/
Triaxial	110	70	Strain-controlled	/	$-0.4, -0.8$

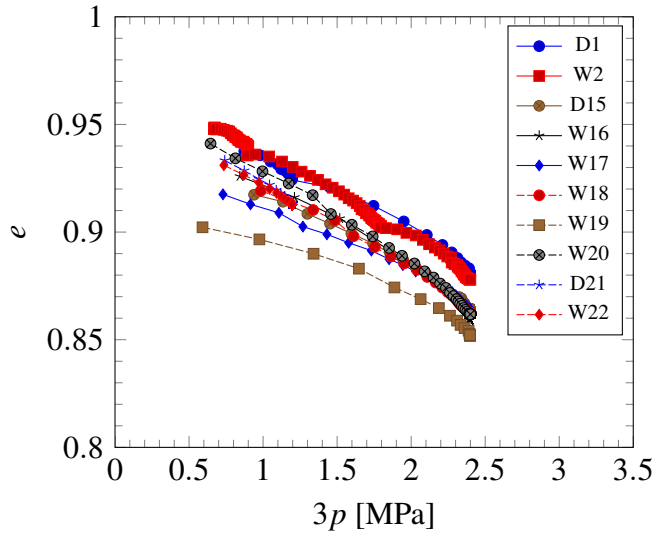

Figure 5.3: Isotropic compression tests results from Ovalle [73] and Ovalle et al. [74]

created after wetting (test W2). In the isotropic compression tests the maximum pressure applied is not sufficient for calibration of h_s.

Oedometric compression tests Specimens with different conditions, dry (D3∼D7), initial saturated (S8∼S10) and initially dry and wetted after a certain compression phase (W11∼W14), were tested in oedoemtric devices and compression results are summarized in Table A.4 and in Fig. 5.5. After wetting the compression curve transferred from the dry curve to and followed the initially saturated curve when the specimen was continuous loaded. This experimental results confirm the wetting effects mentioned in Section 3.2.

Triaxial compression tests Triaxial tests were conducted using loose specimens, which were loaded with constant lateral stress (T_{22}) after isotropic consolidation. Some specimens (W16, W17) were wetted after isotropic consolidation and other specimens (W18, W19, W20 and W22) were wetted after reaching a certain axial strain (see Table A.5). Results of the stress-strain and compression curves of triaxial compression are shown in

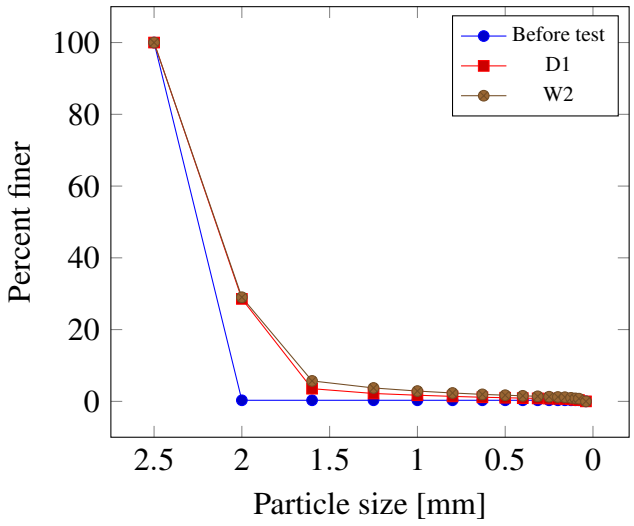

Figure 5.4: GSD results of isotropic compression tests from Ovalle [73]

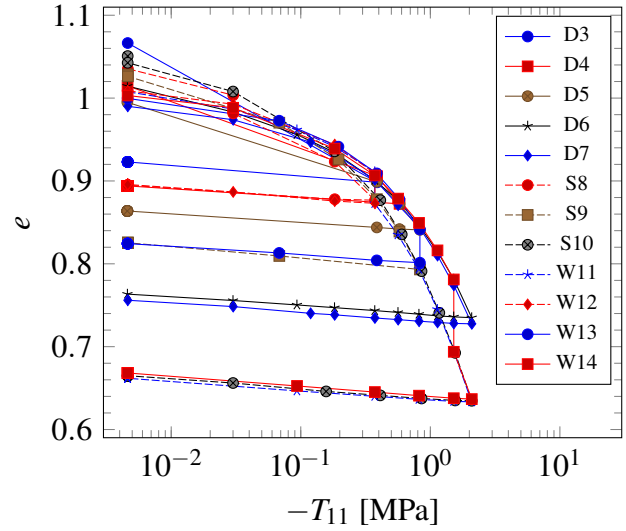

Figure 5.5: Results of oedometric compression tests from Ovalle [73] and Ovalle et al. [74]

Fig. 5.6. After wetting, stress relaxation and reloading, the stress-strain curves are approaching to the compression curves of the initially saturated tests (W16 and W17). The compression curves (W18∼ W20) transfer from the dry curve (similar to the one of D15) to the wet curve (like W16 in Fig. 5.6).

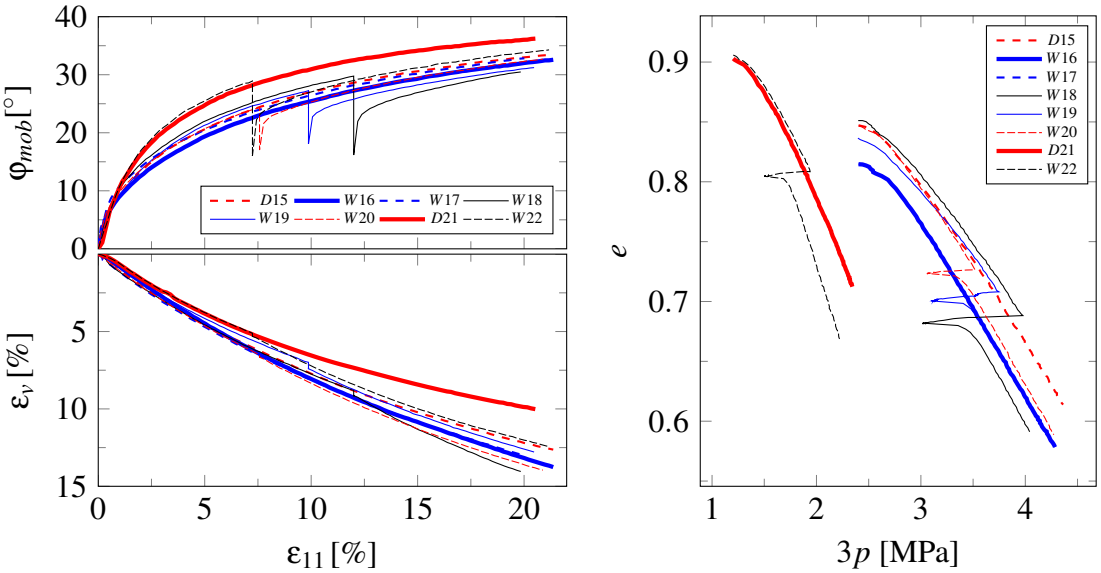

(a) Stress-strain curves

(b) Compression curves in e-$3p$ space

Figure 5.6: Results of triaxial compression tests from Ovalle [73] and Ovalle et al. [74]

5.2 First estimation of the material parameters

The stiffness degradation under creep and stress relaxation of shale quartzite sand were investigated by Ovalle [73] and Ovalle et al. [74]. These investigations provide details which can be used for the calibration of the parameters for the simplified constitutive model introduced in Chapter 4. However, the experimental concept by Ovalle was not designed for the simplified hypoplastic model in this work. As no experimental investigation related to initially dense material, the parameter α, which related to the peak state of the stress-strain behaviour, is difficult to be determined. Therefore, a specific calibration strategy should be considered to overcome the problems of insufficient experimental data for the simplified hypoplastic model.

As outlined in Chapter 4, nine parameters in total are need for the general equation which covered the classic constitutive equation for dry or saturated case and stiffness degradation cases like creep or stress relaxation. h_s (h_{sd} and h_{sw}) and n can be considered as a parameter set which can be determined together according to the isotropic compression or the oedometric compression test results. Other parameters have the own physical meanings and can be considered independent from each other parameters. If all the necessary experimental data is available, except h_s and n, the other parameters can be determined independently and the calibration orders are not important. However, without some important data, the calibration orders are important, and some parameters cannot be determined independently.

5.2.1 Calibration of h_s and n

For the initially loose specimen, the experimental data can be used for the first approximation of the h_s and n, with an easy manner like curve fitting. Therefore, the experimental data of D1 and W2[1] are used for calibrating h_s and n as an illustration (see Fig. 5.7).

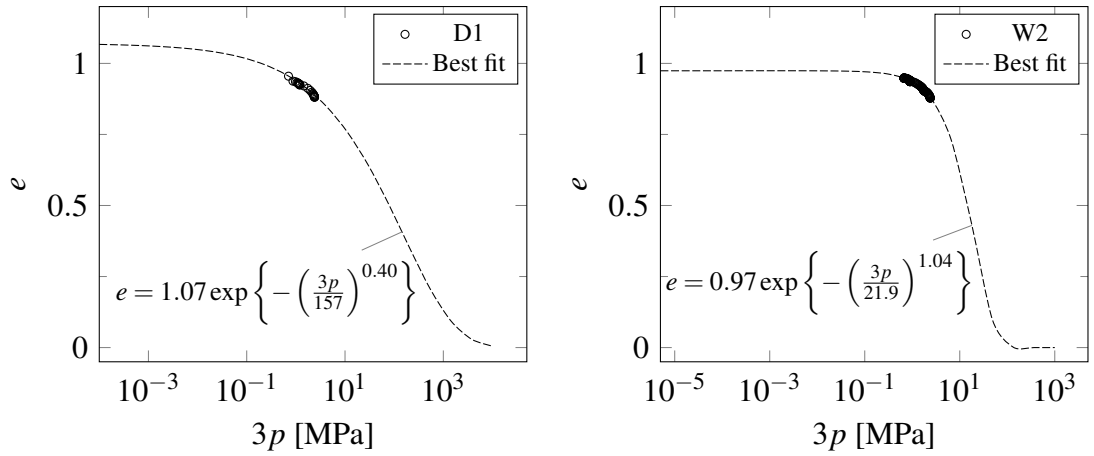

(a) Calibration using data from D1

(b) Calibration using data from W2

Figure 5.7: Calibration of h_{sd} and n using data of isotropic compression tests D1 and W2

As it is shown in Fig. 5.7, the calibration results of h_{sd} and n using experimental data from D1 are $h_{sd} = 157$ MPa and $n = 0.4$, while using data from W2, the calibration results are $h_{sd} = 21.9$ MPa and $n = 1.04$. This huge difference is mainly related to the small stress range. For the small stress range, the trend of the compression curve is not clear, that will easily cause different calibration results, as illustrated in Fig. 5.8.

In contrast to the stress range of isotropic compression tests, the stress range of oedometric compression tests is wider and allows a more precise calibration. However, the lateral stresses in the oedometric tests were not measured. In the conventional soil mechanic oedometric test, the lateral stress is not measured. In order to estimate the lateral stress, the formula by Jáky can be used, i.e.

$$T_{22} = T_{11}\,(1 - \sin\varphi_c) \tag{5.1}$$

Therefore, before we calibrate h_s and n, the critical friction angle of the shale quartzite sand should be determined first.

[1] Only the experimental data of dry state is considered here.

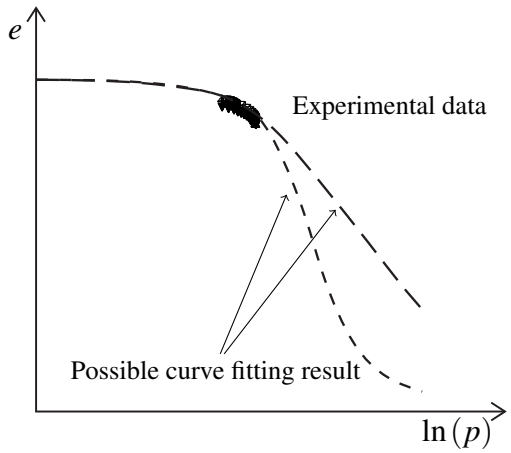

Figure 5.8: Illustration of calibration problem using small stress range

5.2.2 Calibration of φ_c

As it is shown in Fig. 5.6a, the results of triaxial compression tests indicate that the critical state was not approached during the test. In order to calibrate the critical friction angle, assumption of the value of critical friction angle should be made, according to the available experimental data.

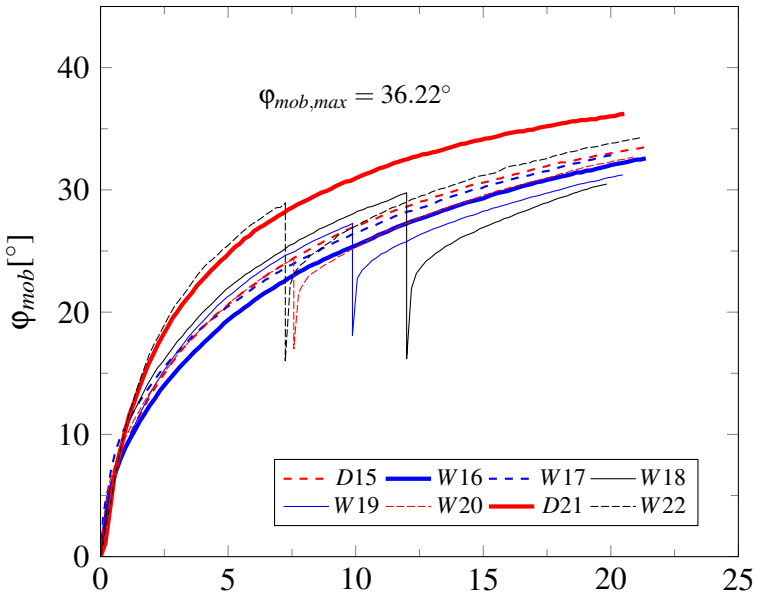

Figure 5.9: Prediction of critical friction angle

From the available triaxial experimental data, as in Fig. 5.9, it can be seen that the max-

imum mobilized friction angle is from the D21 test, $\varphi_{mob,max} = 36.22°$. Considering all these specimens are loose specimens, the φ_{mob} will increase with the developing of axial strain and reach the asymptotic state (critical state) without any peak value. Therefore, we can conclude that φ_c should greater than 36.22° and for the first approximation let us consider the $\varphi_c = 37°$. Because this is only an assumption, element test calculation should be done and compared with relative experimental data to verify whether the assumed value is appropriate or not.

With considering the first assumed value of critical friction angle, $\varphi = 37°$, the oedometric experimental data can be used for calibrating h_s and n. Take D7 as an example, with considering the $\varphi_c = 37°$, the best fit of experimental data leads $h_s = 22.1$ MPa and $n = 0.664$ (see Fig. 5.10).

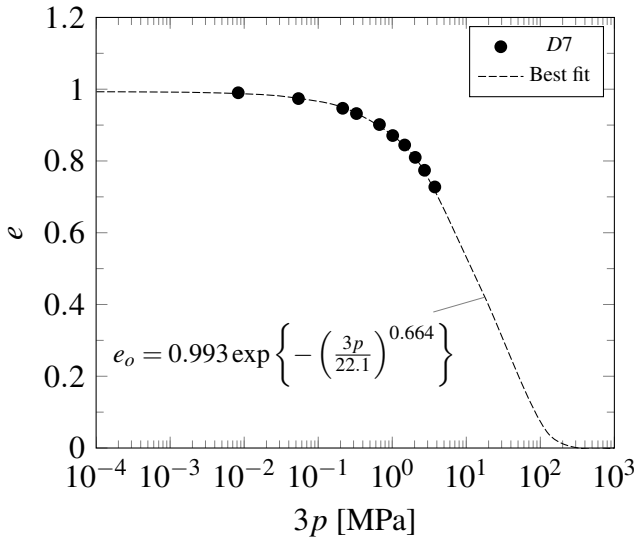

Figure 5.10: Calibration of h_{sd} and n with considering $\varphi_c = 37°$

Before starting to calibrate h_{sw} and n, the effect of uncertainty of the critical friction angle on the calibration results should be clarified. Considering a set of critical friction angle: $\varphi_c = 37°, 38°, 40°, 42°$, the calibration results of h_{sd} and n are presented in Fig. 5.11.

It is clear to see that in Fig. 5.11, the calibrated h_{sd} decreases with the increasing of the value of φ_c. While the calibrated e_o and n are kept constant for this case. It is uncertain that whether the φ_c has no effects on the value of calibrated e_o and n, but it is apparently that using experimental data of D7 with considering different value of φ_c, which ranges from 37° to 42°, no significant difference in the result of calibrated h_{sd}.

Considering the $\varphi_c = 37°$, the results of calibration using a set of selected experimental data are summarized in Table 5.2. The average value of calibration results is considered, $h_{sd} = 22.4$ MPa and $n = 0.64$.

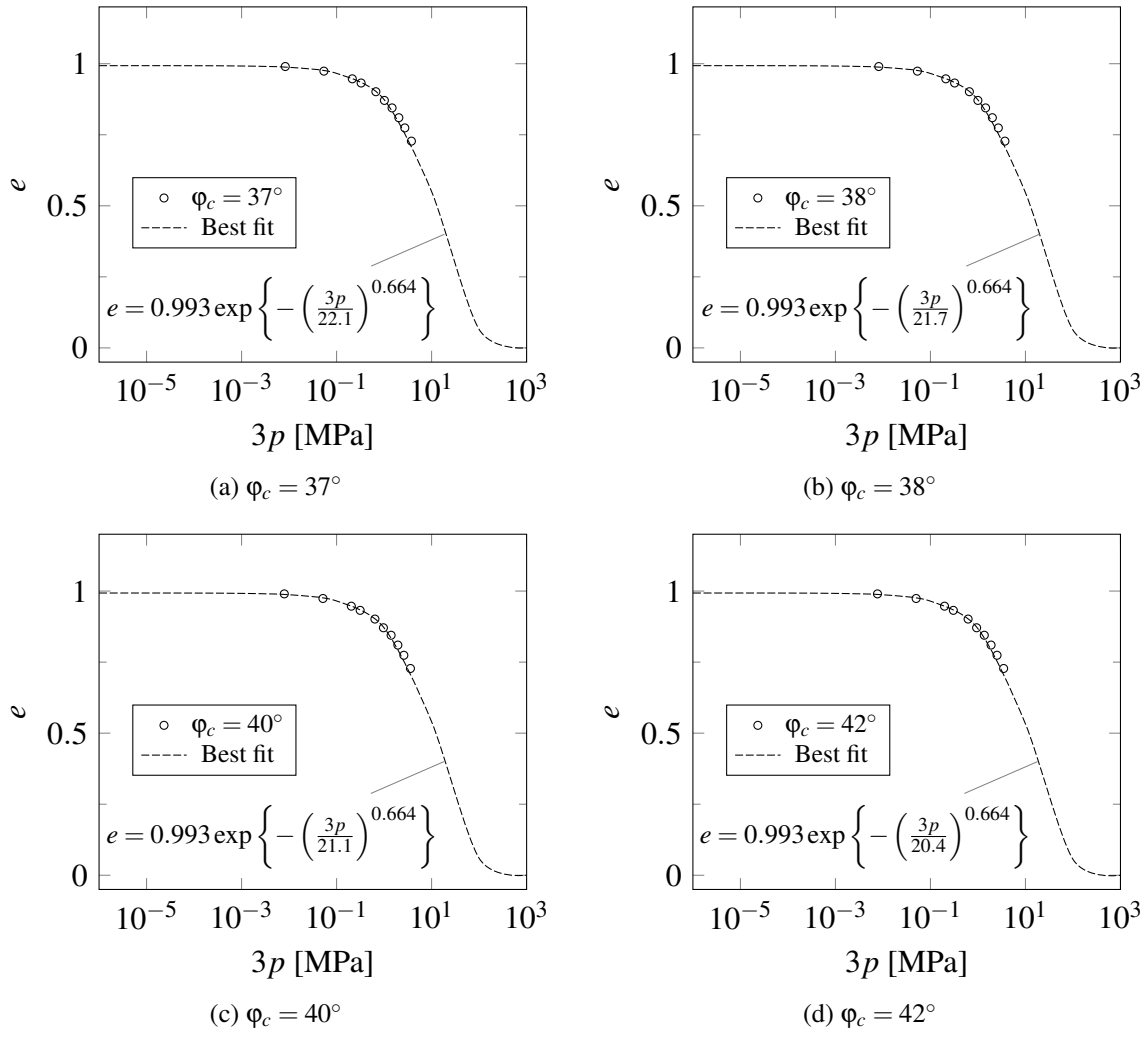

(a) $\varphi_c = 37°$ (b) $\varphi_c = 38°$

(c) $\varphi_c = 40°$ (d) $\varphi_c = 42°$

Figure 5.11: The effects of φ_c on calibration results of h_{sd} and n using experimental data from D7

Table 5.2: Summary of calibration results for dry material with considering $\varphi_c = 37°$

Test no.	e_{o0} [-]	h_{sd} [MPa]	n [-]
D4	1.02	15.7	0.683
D5	1.00	23.9	0.629
D6	1.02	29.7	0.554
D7	0.993	22.1	0.664
W13 (dry)[2]	1.00	17.4	0.713
W14 (dry)[2]	1.01	25.7	0.607
Average value	1.00	22.4	0.64

Now let $\varphi_c = 37^\circ$ and continue to do the calibration of h_{sw} and n. Take the data from S10 as an example, the calibration results are $h_{sw} = 11.5$ MPa and $n = 0.622$ (see Fig. 5.12).

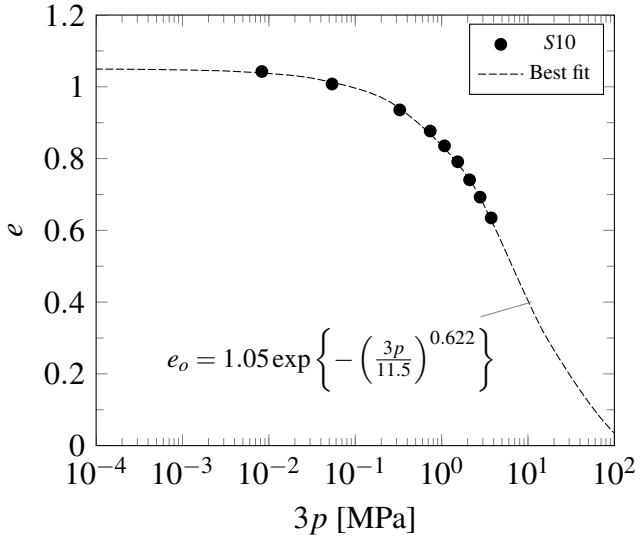

Figure 5.12: Calibration of h_{sw} and n using data from S10 and considering $\varphi_c = 37^\circ$

After analysis the experimental data, experimental data from S8, S9, S10 and W11[3] is selected for calibration and the results are summarized in Table 5.3 In order to simplify

Table 5.3: Summary of calibration results for saturated material with considering $\varphi_c = 37^\circ$

Test no.	e_{o0} [-]	h_{sw} [MPa]	n [-]
S8	1.02	15.7	0.641
S9	1.04	15.4	0.565
S10	1.05	11.5	0.622
W11	0.983	11	0.761
Average value	1.02	13.4	0.647

the model and the calibration procedure, the same value of parameter n is considered for dry and saturated materials. Therefore, for the first approximation, parameters $\varphi_c = 37^\circ$, $h_{sd} = 22.4$ MPa, $h_{sw} = 13.4$ MPa and $n = 0.64$ are considered. Note the calibration result of e_{o0} is not important for the current model.

[2]Before wetting, the specimen is air dried. Therefore, it is appropriate to use the experimental data before wetting for calibration.

[3]Only the data after saturation is considered.

5.2.3 Calibration of e_{i0} and e_{c0}

With the given values of h_s and n, the initial value of maximum void ratio e_{i0} and the critical void ratio e_{c0} can be determined based on the experimental data from loose isotropic compression tests and from the triaxial compression tests, respectively. It should be noted that saturation will have no effects on the initial value of maximum void ratio and the initial value of critical void ratio. This assumption is also confirmed by experiments by Alonso and Cardoso [1]. However, from the experiments it cannot be concluded with certainty that test D1 is in the loosest state or not. It is also apparently that the triaxial compression tests available did not reach the critical state. Therefore no data for e_c are available as well.

Possible value of e_{i0}

Recalling that the e_i curve is the upper bound of the possible void ratio range at a given stress level, which means all the available experimental data should not cross the compression curve of e_i. Thus, the minimum possible value of e_{i0} can be estimated, provided that the h_s and n are given. Therefore, considering the $h_{sd} = 22.4$ MPa and $n = 0.64$, the minimum possible value of e_{i0} is $e_{i0,min} = 1.13$, which fulfill the requirement that no void ratio of available experimental data can cross the compression curve. Then $e_{i0} \geq 1.13$.

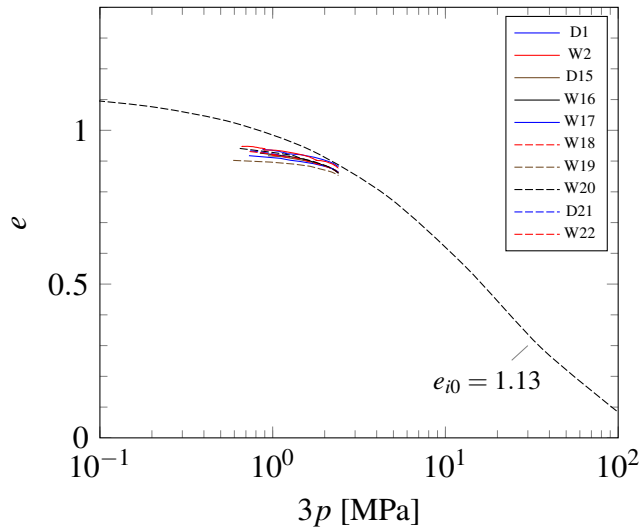

Figure 5.13: Possible initial value of maximum limit void ratio with providing $h_{sd} = 22.4$ MPa and $n = 0.64$

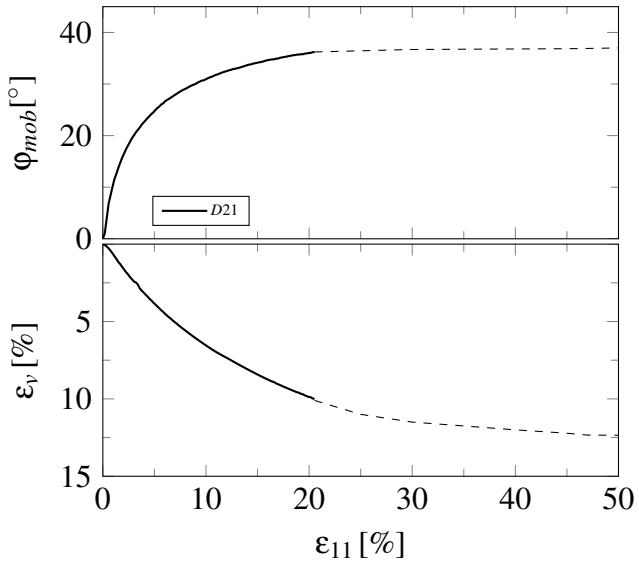

Figure 5.14: Estimation of asymptotic state: solid curves denote experiments of D21; dashed curves denote estimated extrapolation.

Possible value of e_{c0}

According to the estimated value of volume strain at the asymptotic state, the corresponding critical void ratio can be calculated using the following steps:

With respect to the relationship

$$\epsilon_v = \ln(1-\varepsilon_v) = \ln\left(\frac{1+e}{1+e_0}\right) \tag{5.2}$$

and for $e = e_c$ one obtains

$$e_c = e_0 - \varepsilon_v(1+e_0) \tag{5.3}$$

Here the $\varepsilon_v = 12.35\%$, then the corresponding critical void ratio is $e_c = 0.7914$. While, this extrapolation method might not precisely enough, a better way is to find the maximum possible value of critical void ratio. It is obvious that the final value of void ratio from W16 is smaller than the other saturated condition, then assuming this void ratio is the critical void ratio for W16 (in reality it is not the critical void ratio), an initial value of critical void ratio can be back calculated according to the Eq. (5.4):

$$e_{c0} = e_c \exp\left\{\left(\frac{3p}{h_s}\right)^n\right\} \tag{5.4}$$

Here, for W16, $3p = 4.284$ MPa and $e = 0.578$, providing the $h_{sw} = 13.4$ MPa and $n = 0.64$, the assumed $e_{c0} = 0.936$. With respect that the $e > e_c$, therefore the assumed initial value of critical void ratio is over predicted, and $e_{c0} < 0.936$.

Thus, in this section, it can be concluded that $e_{i0} \geq 1.13$ and $e_{c0} < 0.936$, provided the $h_{sd} = 22.4$ MPa, $h_{sw} = 13.4$ MPa and $n = 0.64$.

5.2.4 Calibration of $\breve{\alpha}$ and β

As experimental investigations of the initial dense material are not carried out by Ovalle [73] and Ovalle et al. [74], no data about pressure dependent peak friction angle is available. Here, the parameter $\breve{\alpha}$ can only be calibrated by iteration procedure. For the density factor used in this model, a first approximation of parameter $\breve{\alpha}$ is made as $\breve{\alpha} = 0.5$.

Numerical investigations show that the looser material is, the less effects of β on the prediction of stress-strain behaviour will be. In this case, $\beta = 1$ was found to be sufficient accurate.

Parameter study

Based on the analysis in the previous section, the parameter set for the first approximation is: $\varphi_c = 37^\circ$, $h_{sd} = 22.4$ MPa, $h_{sw} = 13.4$ MPa, $n = 0.64$, $e_{i0} = 1.2$, $e_{c0} = 0.9$ and $\breve{\alpha} = 0.5$.

According to the proposed parameter set, the effect of each parameter on the model performance is studied by varying the values of the parameters for dry material while keeping the other parameters the same as proposed. Parameter set for each test and initial conditions are summarized in Table A.6. It can be noted that the effects of parameters on wet material are similar to the one on dry material.

Effects of φ_c on the performance of the model

Triaxial element tests with same initial stresses, $T_{11} = T_{22} = T_{33} = -0.1$ MPa, different initial density, $e_0 = 0.6$ for dense material and $e_0 = 1.0$ for loose material, are simulated with different critical friction angles. As it is shown in Fig. 5.15, for dense material the critical friction angle has apparently effect on mobilized friction angle, especially after the stress-strain curve reached the peak state. With increasing critical friction angle, the mobilized friction angle increases. Not significant difference caused by critical friction angle on volumetric strain behaviour occurs for dense material. While for loose material, the volumetric strain increases with the critical friction angle increasing. For both dense and loose material, the critical friction angle affects the value of critical void ratio for a given initial stress level. Moreover, the greater the critical friction angle is, the smaller the critical void ratio will be.

Effects of h_s on the performance of the model

Different values of solid hardnesses are considered to analyse the effects of h_s on the model performance. The results of element tests are summarized in Fig. 5.16. It can be seen that the greater the value of h_s is, the stiffer the material behaves. In addition, the effect of h_s is more pronounced in the volumetric strain behaviour. It is obvious that with increasing of h_s, the volumetric strain decreases.

Effects of n on the performance of the model

The results of numerical simulations are summarized in Fig. 5.17. The effect of n on the stress-strain behaviour is similar to the one of h_s. The range of n are relative small, at least $n \in (0, 1.0)$, the different between the values of n considered here are relative huge. Since the n and h_s are parameters of the compression equation, it is strongly suggested to determining the h_s and n together. Any changes of h_s or n will affect the compression curve, and the upper limit bound of void ratios should not be violated.

Effects of e_{i0} on the performance of the model

Considering the same initial conditions and the set of initial values of maximum void ratio, $e_{i0} = 1.1,\ 1.2,\ 1.3,$ and 1.4, with the other parameters as proposed in Table A.6, no distinguishing difference is observed from the numerical simulation.

Effects of e_{c0} on the performance of the model

With respect to the same initial conditions and the parameter of Table A.6, the simulation are carried out with $e_{c0} = 0.7,\ 0.8,\ 0.9,$ and 1.0. Fig. 5.18 shows that e_{c0} has strong effect on the stress-strain behaviour of the material. The value of the initial critical void ratio affects the value of density factor which is taken account into the constitutive model. For initially dense material, the greater the initial critical void ratio is, the more significant dilatancy of the material is; for initially loose material, the greater initial critical void ratio leads less compaction.

Effects of $\breve{\alpha}$ on the performance of the model

As shown in Fig. 5.19, $\breve{\alpha}$ has strong influence on the shape of volumetric strain curve for both loose and dense material. The greater value of $\breve{\alpha}$ is, the higher peak friction angle is. The peak state occurs earlier in the stress-strain curve. In addition, $\breve{\alpha}$ affects the dilatancy behaviour of the material, for a greater value of $\breve{\alpha}$ the asymptotic state will be reached earlier. However, for the loose material, the effect of $\breve{\alpha}$ on the stress-strain behaviour is not observed apparently.

5.3 Specific calibration procedure

For the case that certain experimental data are missing or the available data are within a small stress range, the direct calibration usually will fail. A specific calibration procedure

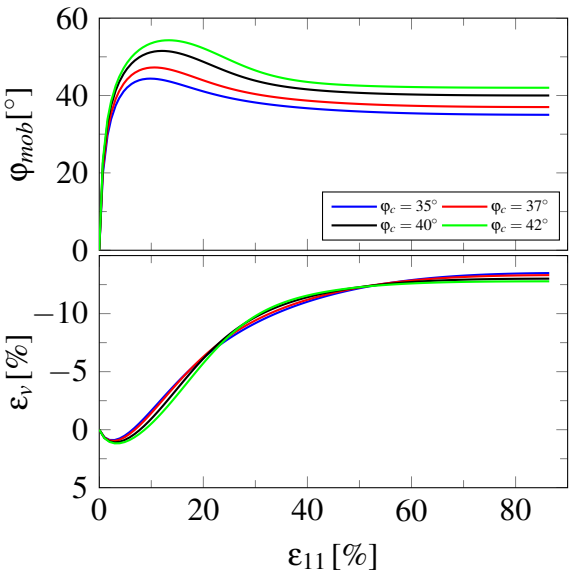

(a) Stress-strain curves of dense material

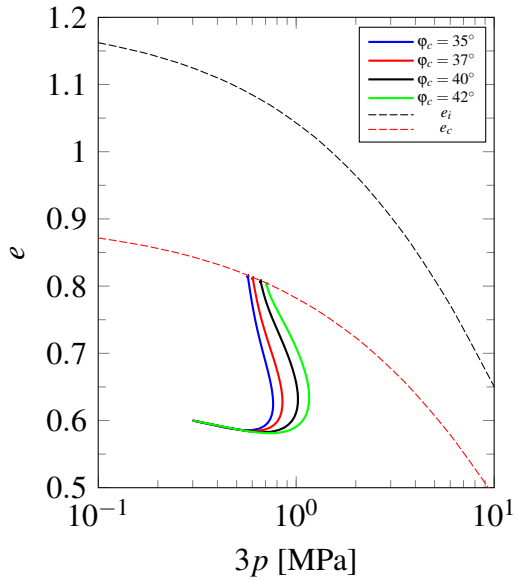

(b) Compression curves of dense material

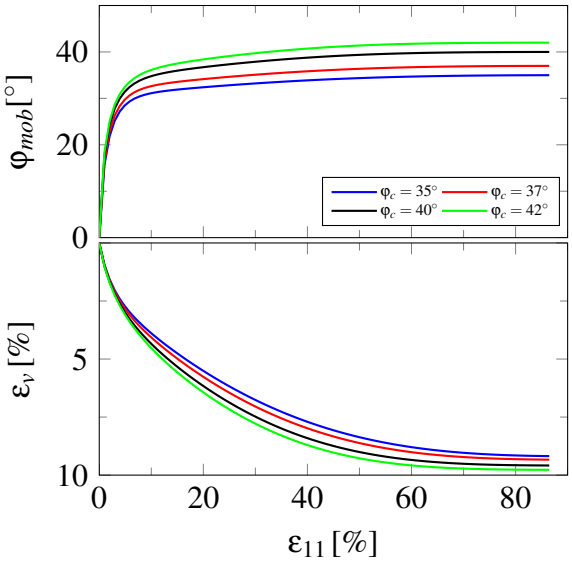

(c) Stress-strain curves of loose material

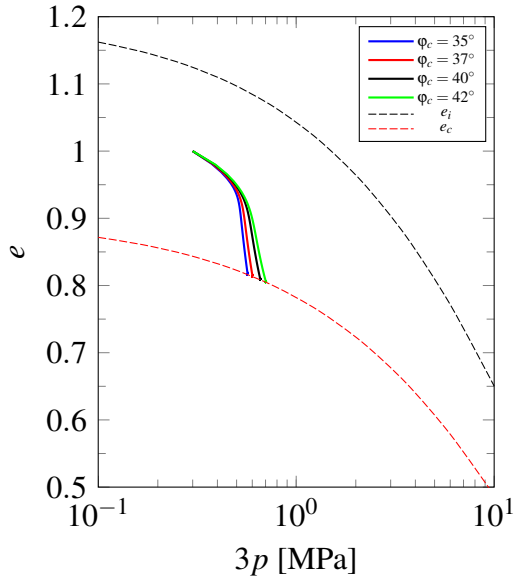

(d) Compression curves of loose material

Figure 5.15: Triaxial element tests: influence of critical friction angle φ_c

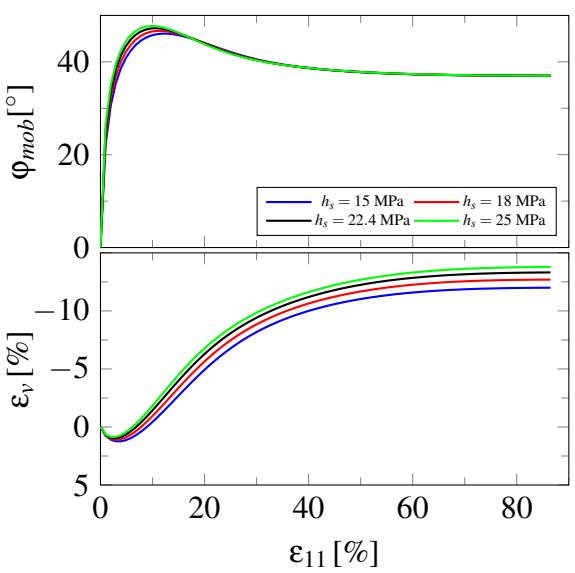

(a) Stress-strain curves of dense material

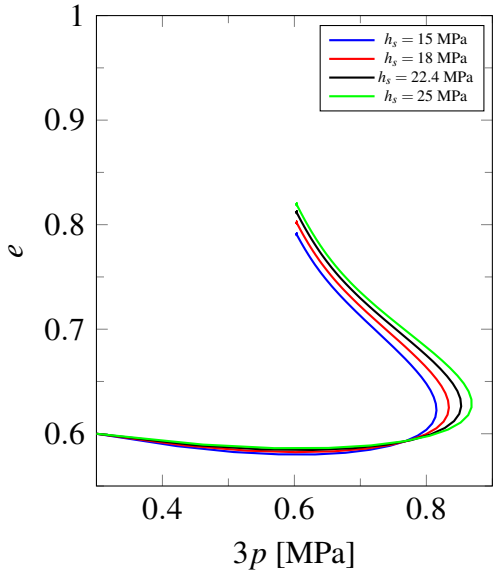

(b) Compression curves of dense material

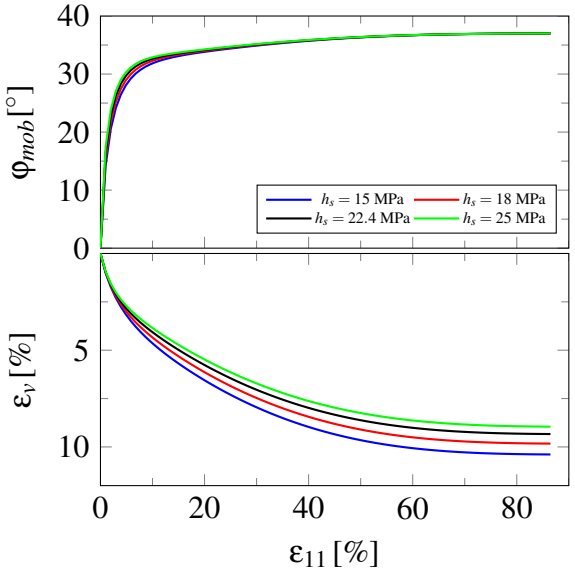

(c) Stress-strain curves of loose material

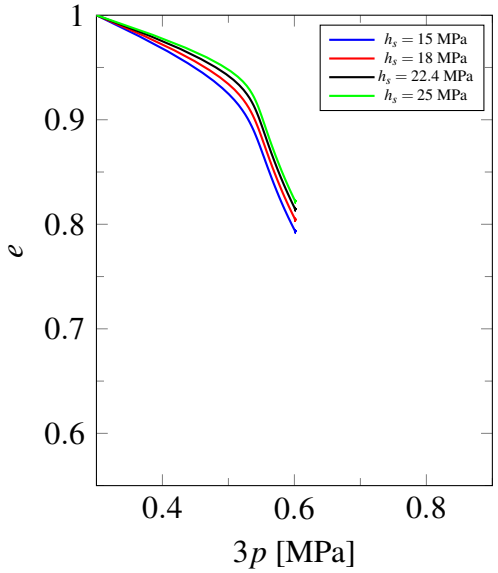

(d) Compression curves of loose material

Figure 5.16: Triaxial element tests: influence of critical friction angle h_s

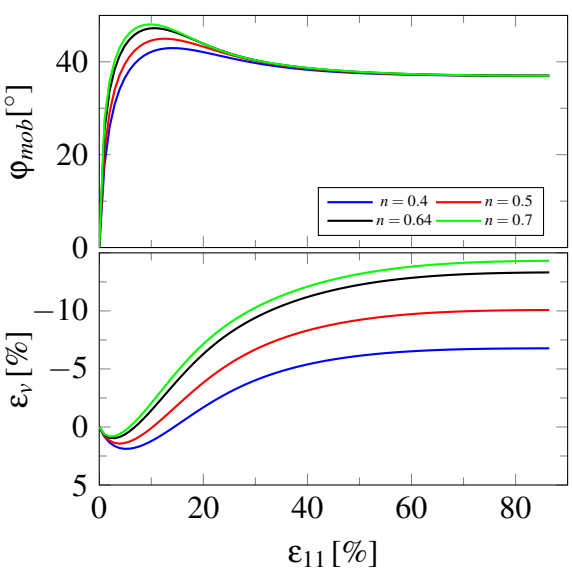

(a) Stress-strain curves of dense material

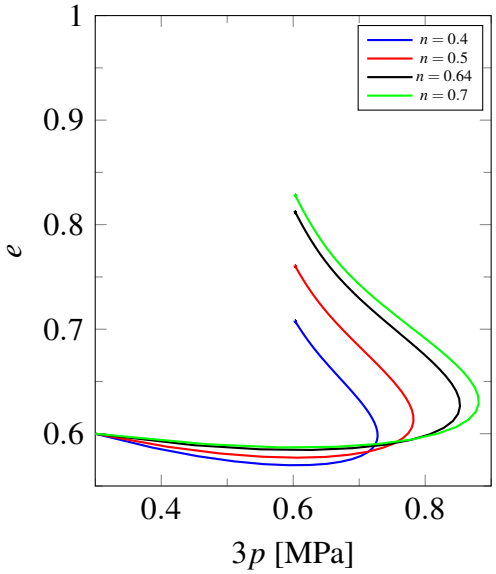

(b) Compression curves of dense material

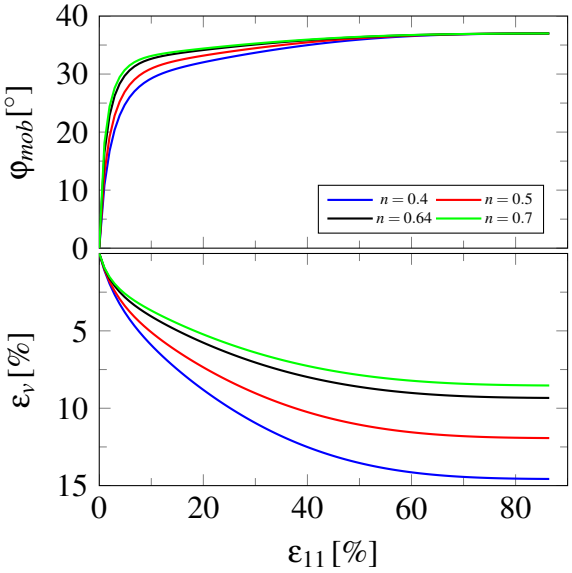

(c) Stress-strain curves of loose material

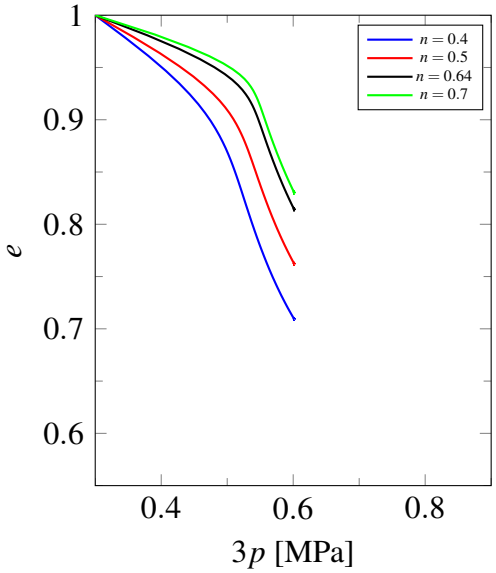

(d) Compression curves of loose material

Figure 5.17: Triaxial element tests: influence of critical friction angle n

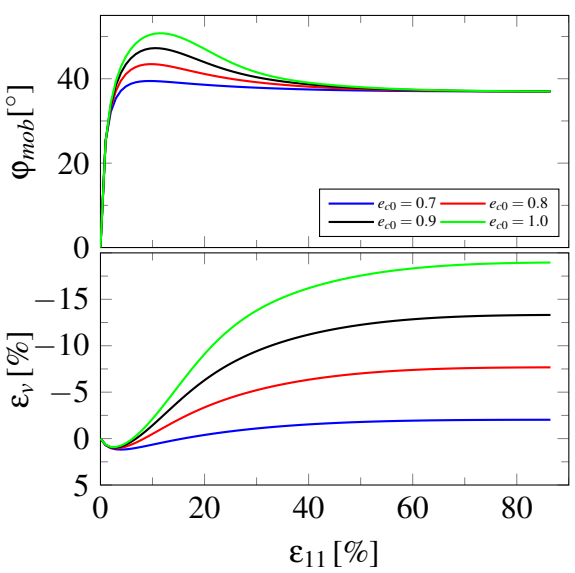

(a) Stress-strain curves of dense material

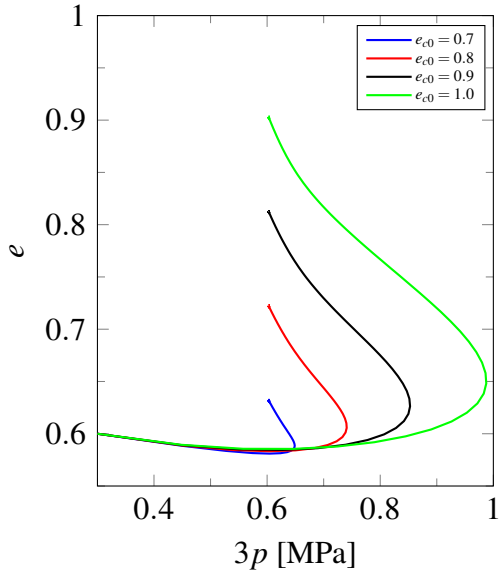

(b) Compression curves of dense material

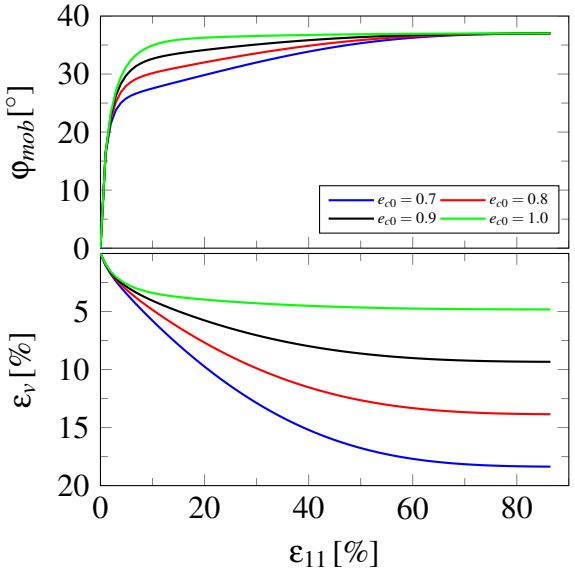

(c) Stress-strain curves of loose material

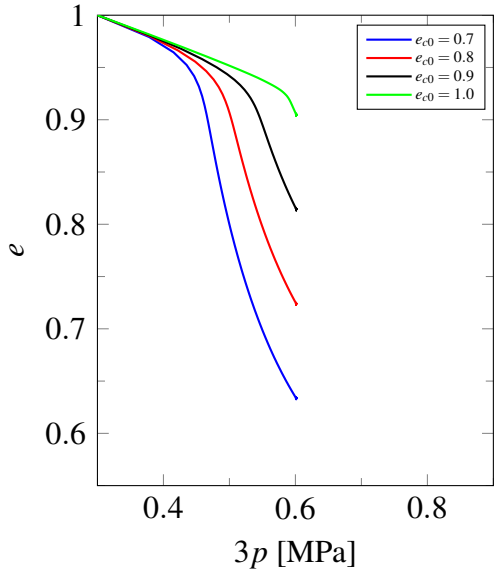

(d) Compression curves of loose material

Figure 5.18: Triaxial element tests: influence of critical friction angle e_{c0}

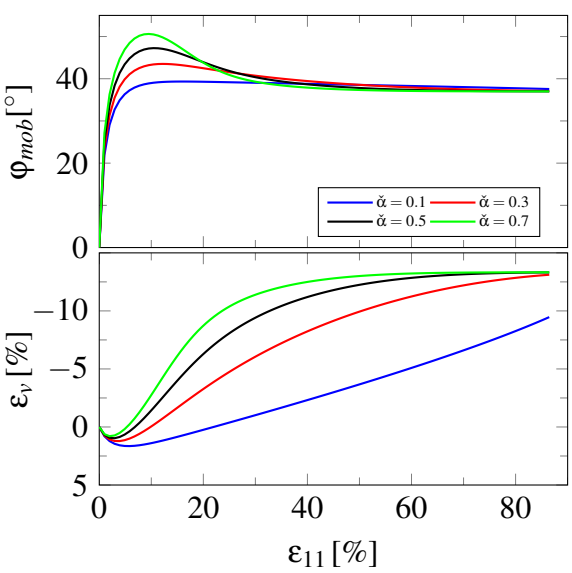

(a) Stress-strain curves of dense material

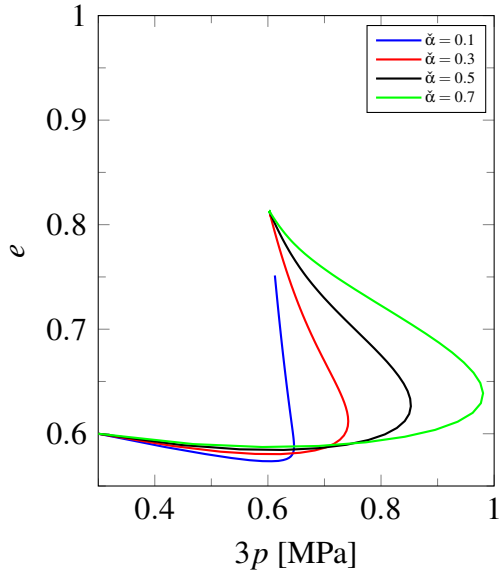

(b) Compression curves of dense material

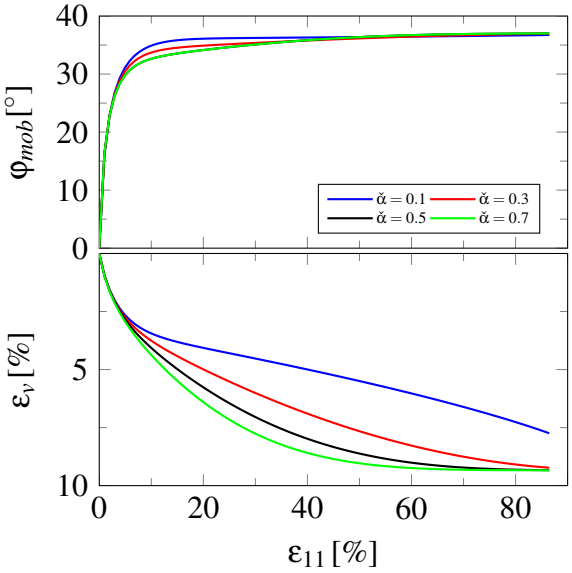

(c) Stress-strain curves of loose material

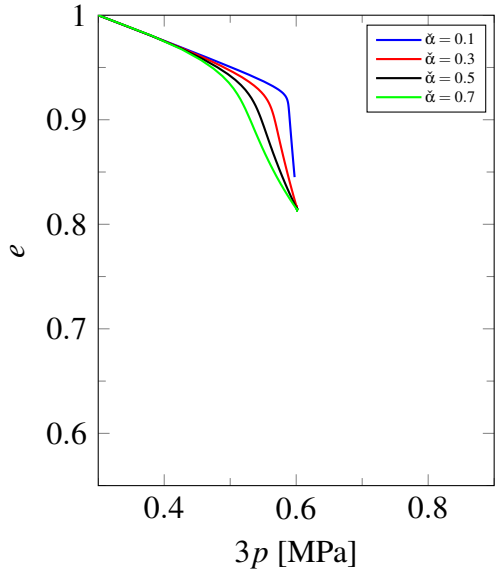

(d) Compression curves of loose material

Figure 5.19: Triaxial element tests: influence of critical friction angle ă

should be proposed based on the available experimental data. In this case the order of assumptions made for the first estimation plays an important rule. The set of parameters assumed must be validated by comparing the results of numerical simulations with experimental data. To this end a numerical simulation program for investigation of the behaviour of material element is required (see the program HET in Appendix A.3). For improving the set of parameters assumed, an iterative procedure can be used.

Iteration procedure

Using the proposed parameter set (as tabulated in Table 5.4), element tests are carried out for the material under dry and saturated conditions, respectively. In particular, isotropic, oedometric and triaxial compression element tests are conducted for both dry and saturated materials. Since the isotropic compression data is within a relative small stress range, comparison between experimental and numerical results of isotropic compression is not presented here. In general, based on the assumption of φ_c and the calibrated h_s and n, the numerical simulation of oedometric compression tests normally shows good agreement with the corresponding experimental data (see Fig. 5.20).

Table 5.4: Parameter set for the first simulation

	φ_c [°]	h_{sd} [MPa]	h_{sw} [MPa]	n [-]	e_{i0} [-]	e_{c0} [-]	α [-]
Dry	37	22.4	/	0.64	1.2	0.9	0.5
Saturated	37	/	13.4	0.64	1.2	0.9	0.5

However, the numerical simulation of triaxial compression test shows deviation from the experimental data for most of the tests (see Fig. 5.21, 5.22 and 5.23). This is mainly because of the oedometric compression, which starts from a relative loose state, approaches to the asymptotic state approximate proportionally. While the triaxial compression test results of the numerical simulation are highly dependent on these parameters related to the critical state, i.e. φ_c, e_{i0}, e_{c0} and α.

In particular, for those tests with lateral stress $T_{22} = -0.8$ MPa, the volumetric strain results of the numerical simulation are smaller than the volumetric strain from experimental data. The reasons of under-prediction of volumetric strain could be one of the followings:

- the h_{sd} and h_{sw} are over-predicted, which leads a stiffer volumetric strain behaviour.
- the relative density of the material is not well-predicted, which means either one of the parameter e_{i0}, e_{c0} and α is not well-predicted, or two or even all of these three parameters are not appropriate.

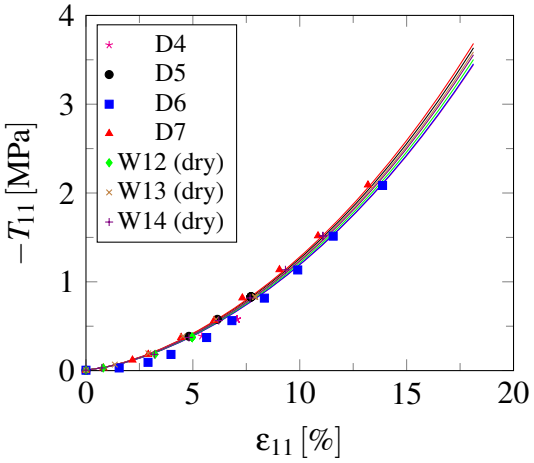

(a) Axial stress-strain results of dry material

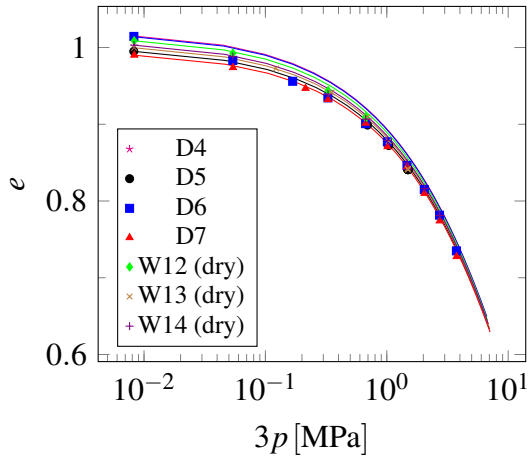

(b) Compression curves of dry material

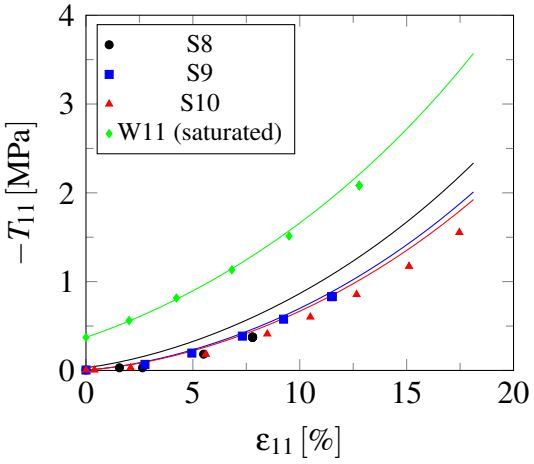

(c) Axial stress-strain results of wet material

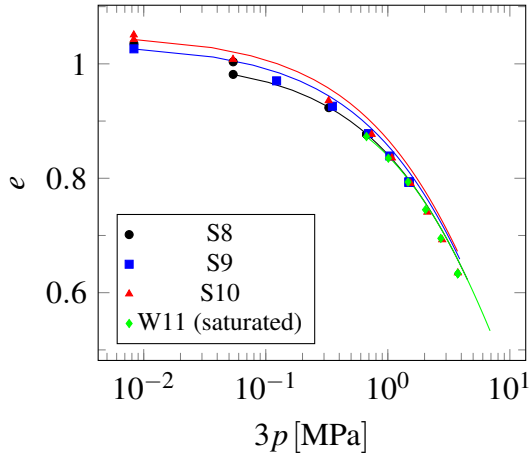

(d) Compression curves of wet material

Figure 5.20: Oedometric compression tests using the parameter set from Table 5.4 (markers are experimental results and solid curves are numerical simulation results).

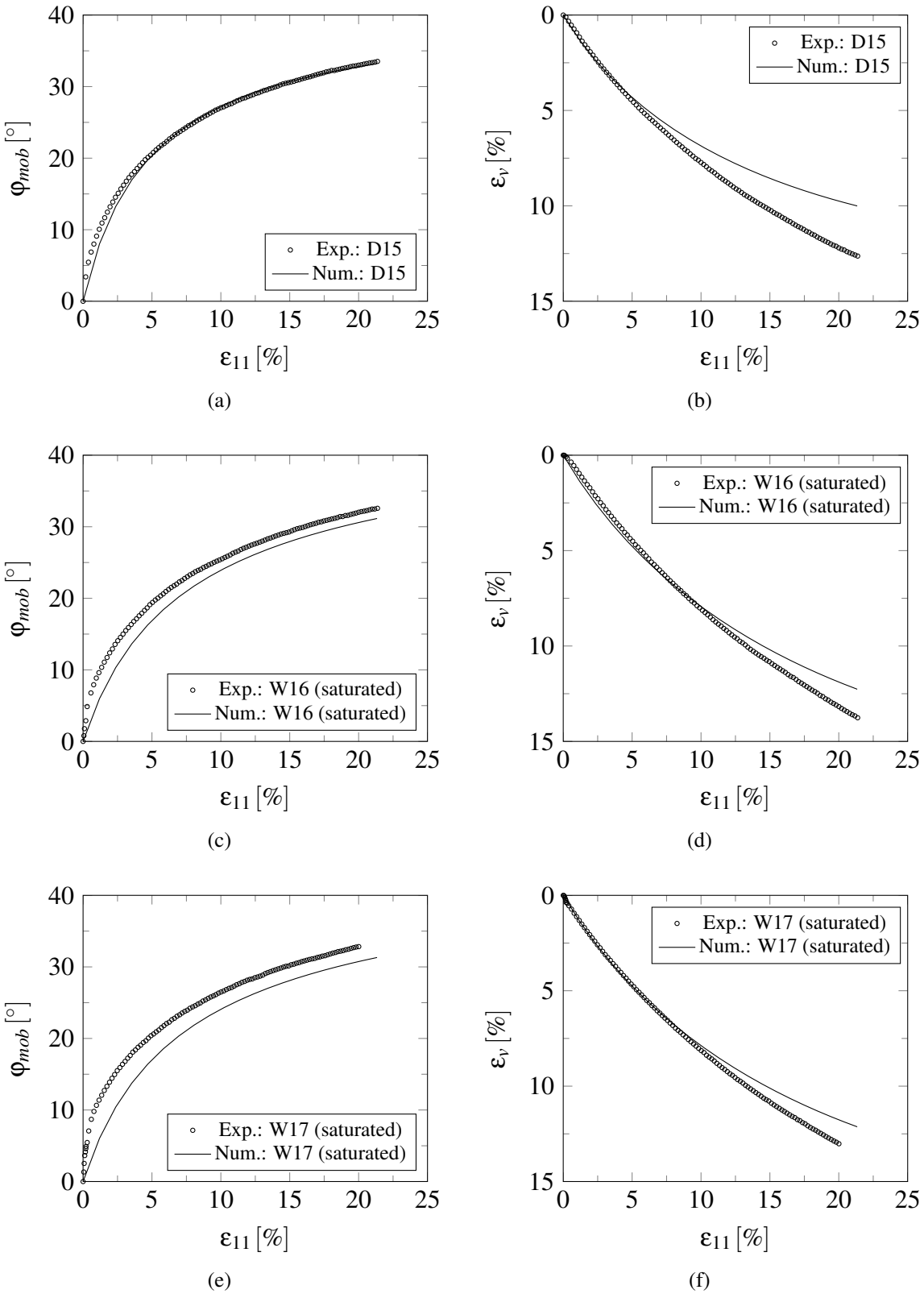

Figure 5.21: Comparison of numerical simulation with experimental data of D15∼W17 using parameters from Table 5.4

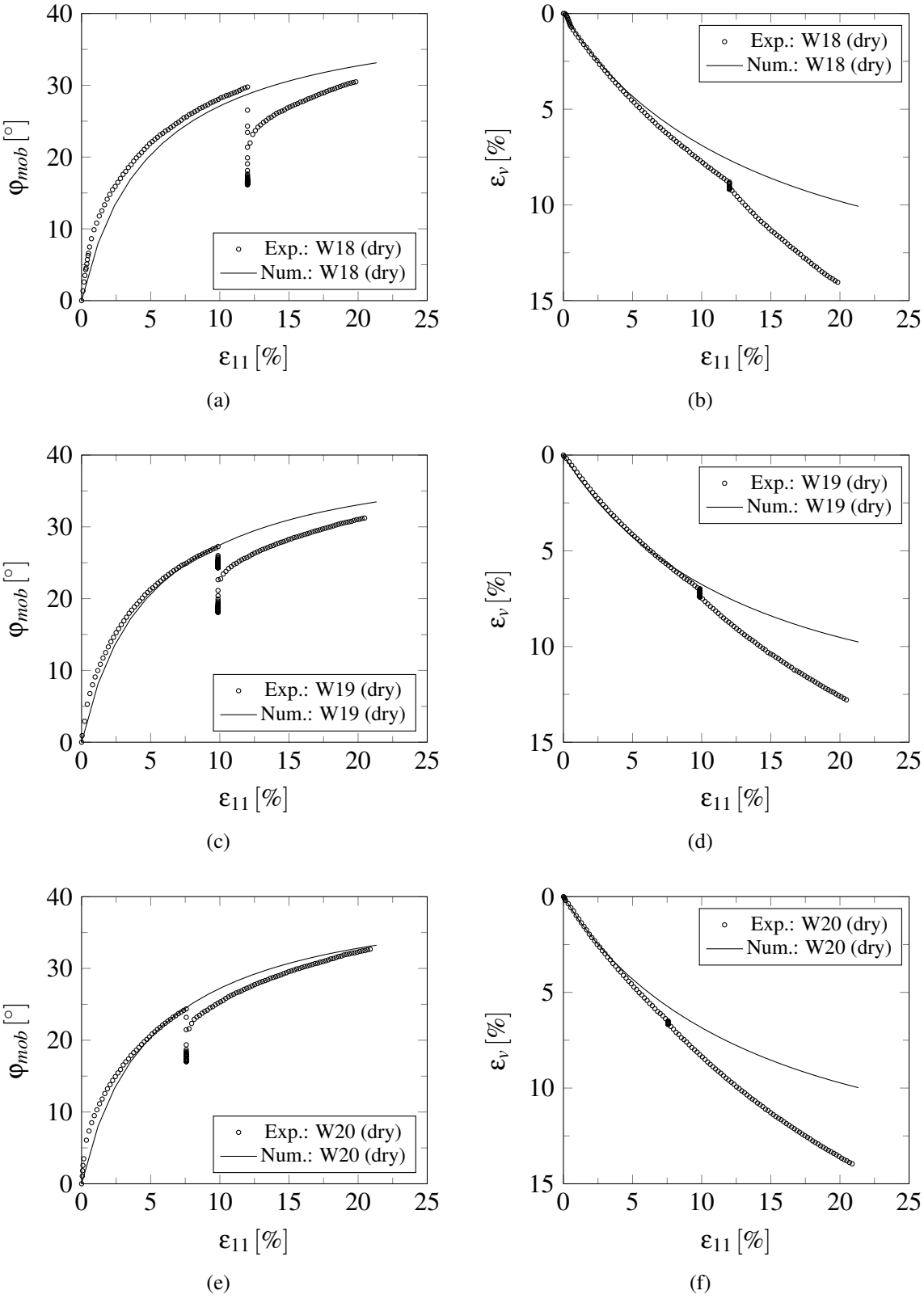

Figure 5.22: Comparison of numerical simulation with experimental data of W18∼W20 using parameters from Table 5.4

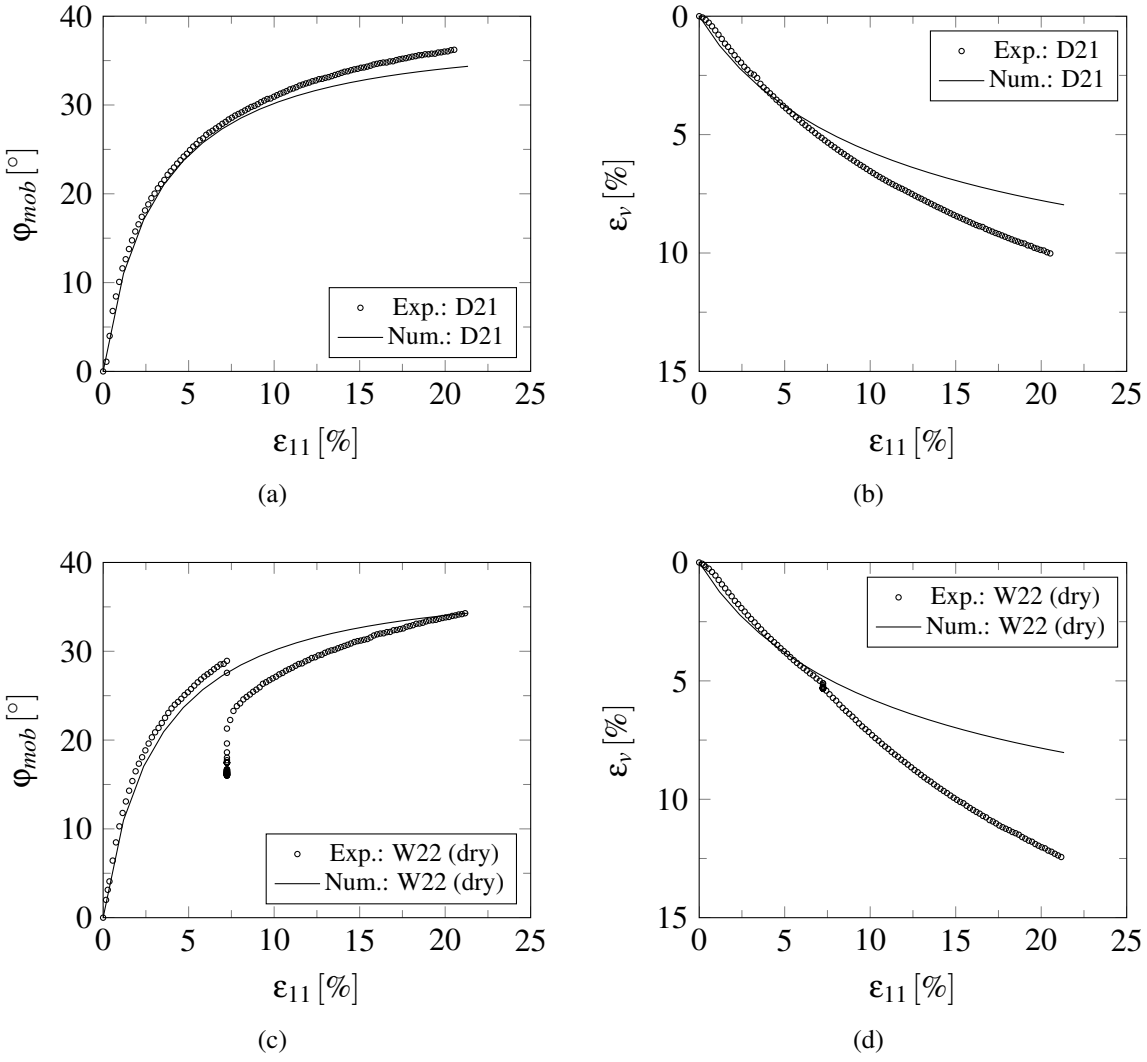

Figure 5.23: Comparison of numerical simulation with experimental data of D21∼W22 using parameters from Table 5.4

- the mobilized friction angle used in this simulation is smaller than the one it should be.

Moreover, numerical simulation of W16 and W17 shows that the mobilized friction angle is under-predicted (comparing the experimental data), which means the stiffness of the saturated material should be higher than the one predicted by the numerical simulation. This indicates an appropriate value of h_{sw} should be greater than the one used in this simulation, $h_{sw} > 13.4$ MPa.

From the Fig. 5.23, it can be seen that the critical friction angle (the asymptotic value of the mobilized friction angle) should be greater than the value which used in this simulation. In another word, it can be concluded that $\varphi_c > 37^\circ$.

Based on the analysis of the first numerical simulation results, the iteration procedure is considered for the calibration:

- increase the value of φ_c
- calibrate the h_{sd}, h_{sw} and n, using the same procedure as suggested in Section 5.2.1 and Section 5.2.2
- test different parameter combinations
- analysis the numerical simulation and suggest the parameter set for the next iteration

Numerical simulations with different combination of possible parameters are conducted and the results are compared with the corresponding experimental data. Based on the iteration procedure, the suggested parameters of the classic model for the shale quartzite sand are summarized in Table 5.5 and the numerical simulation results are presented in Fig. 5.24, 5.25, 5.26 and 5.27.

Table 5.5: The proposed parameter set for dry or saturated shale quartzite sand

	φ_c [°]	h_{sd} [MPa]	h_{sw} [MPa]	n [-]	e_{i0} [-]	e_{c0} [-]	α [-]
Dry	40	23.6	/	0.6	1.3	0.8	0.5
Saturated	40	/	15	0.6	1.3	0.8	0.5

Therefore, only the parameter c is not calibrated. The parameter c, as presented in Eq. (4.3), has the same dimension as the time and is a factor that relates to the degradation velocity. As result, the parameter c normally has significant influence on the slope of the ε_v-t curve, as illustrated in Fig. 5.28. As it is illustrated in Fig. 5.28, the value of c has no effect on the final volumetric strain. Which means for the case that the h_{sd} and h_{sw} are given, an appropriate value of c should exist and can be easily calibrated according to the information of the ε_v-t. Unfortunately, due to lack of the experimental data, the parameter c cannot be

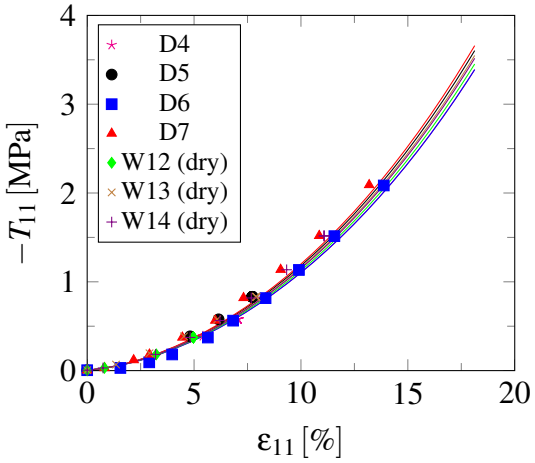

(a) Axial stress-strain results of dry material

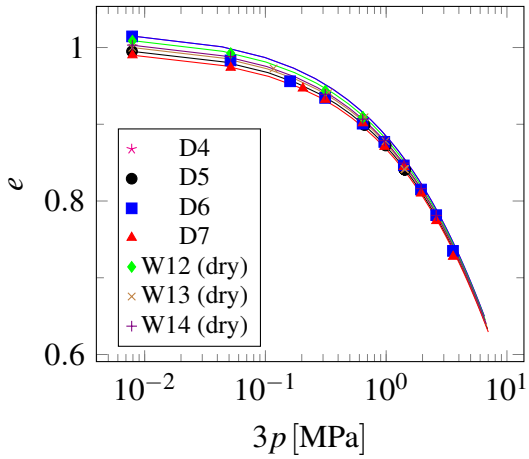

(b) Compression curves of dry material

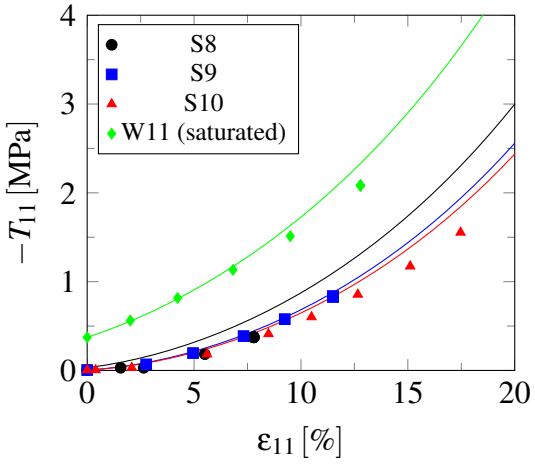

(c) Axial stress-strain results of wet material

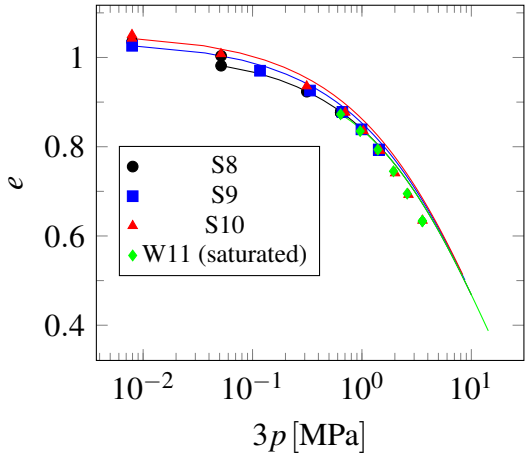

(d) Compression curves of wet material

Figure 5.24: Oedometric compression tests using the parameter set from Table 5.5 (markers are experimental results and solid curves are numerical simulation results).

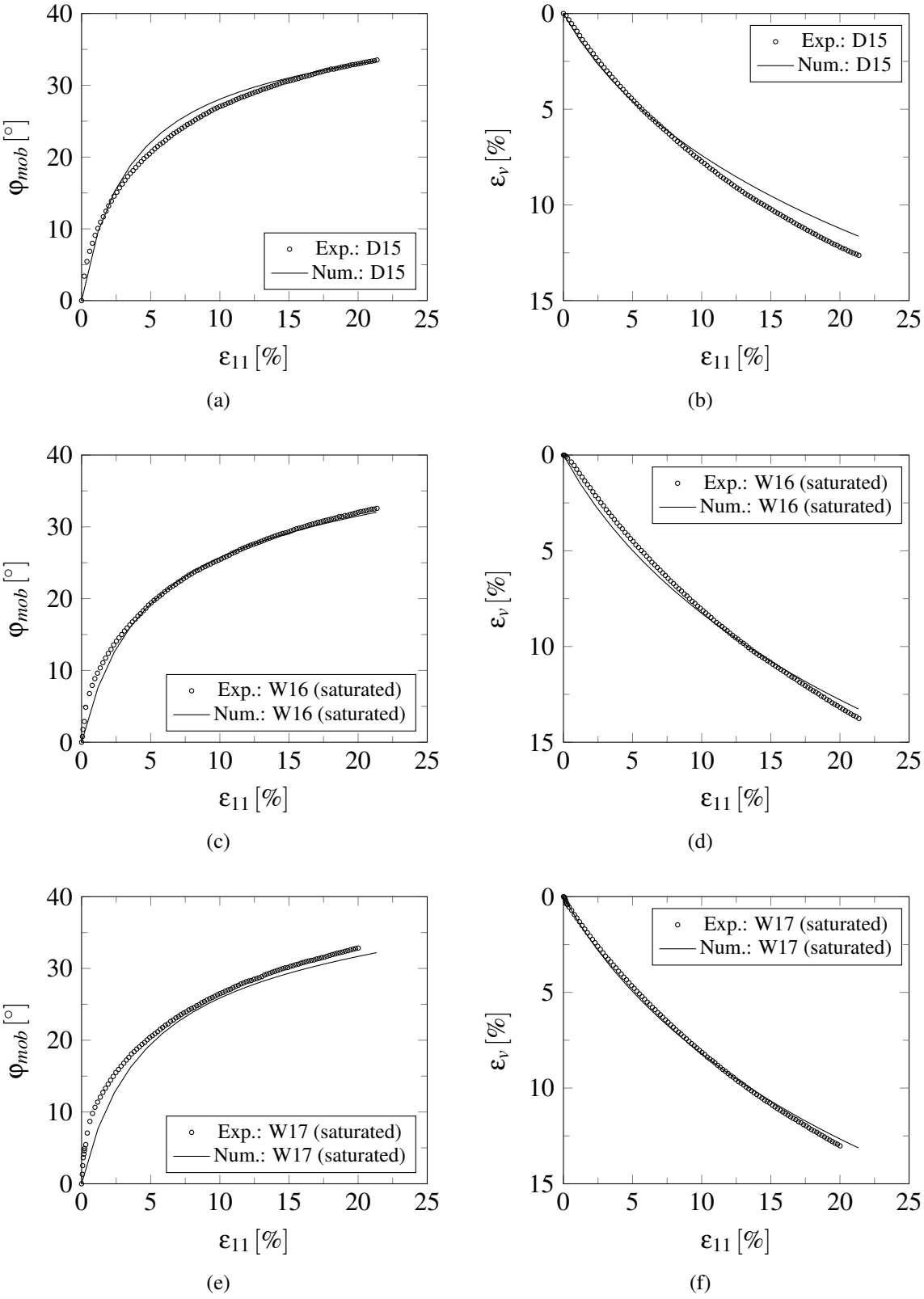

Figure 5.25: Comparison of numerical simulation with experimental data of D15∼W17 using parameters from Table 5.5

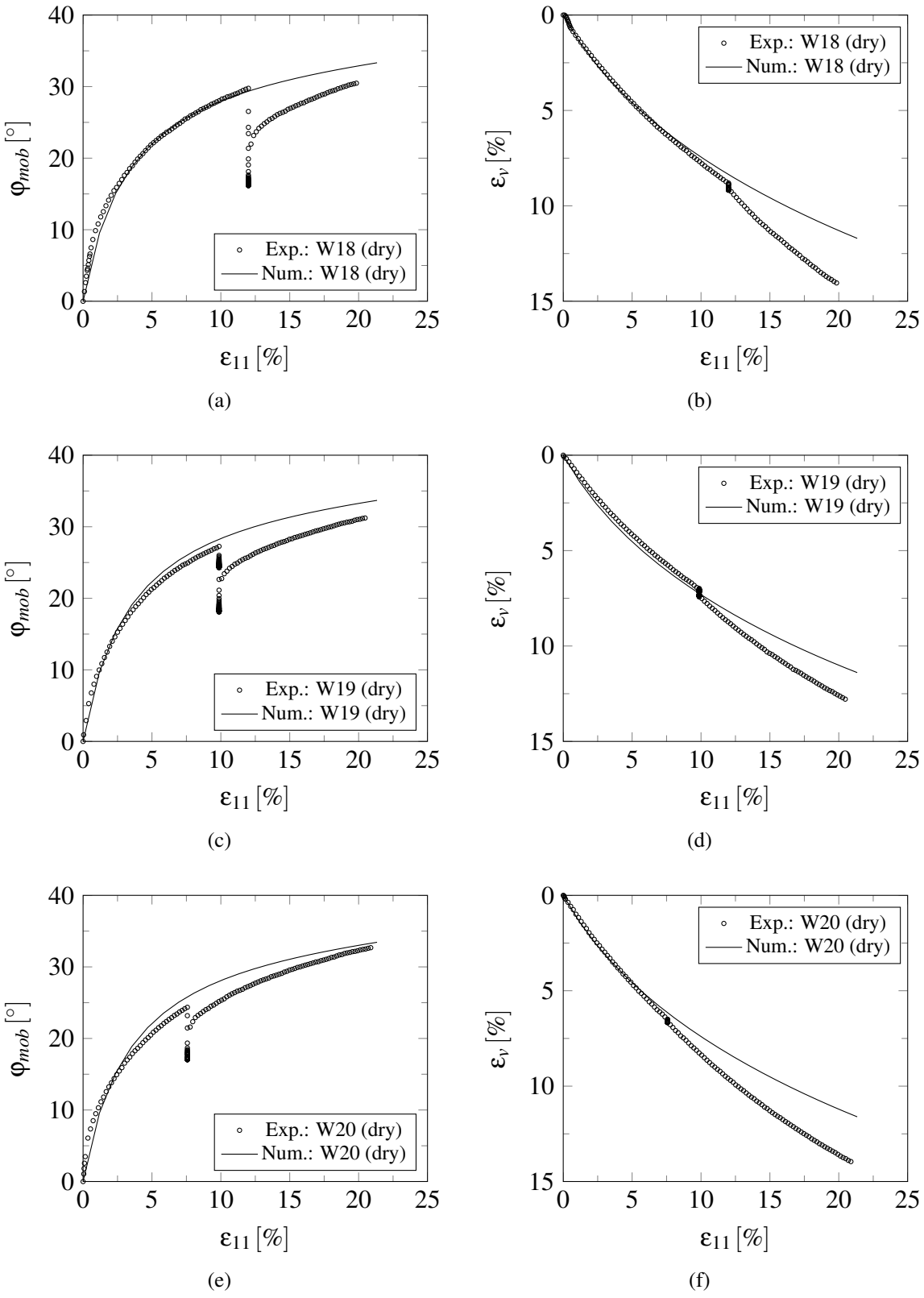

Figure 5.26: Comparison of numerical simulation with experimental data of W18∼W20 using parameters from Table 5.5

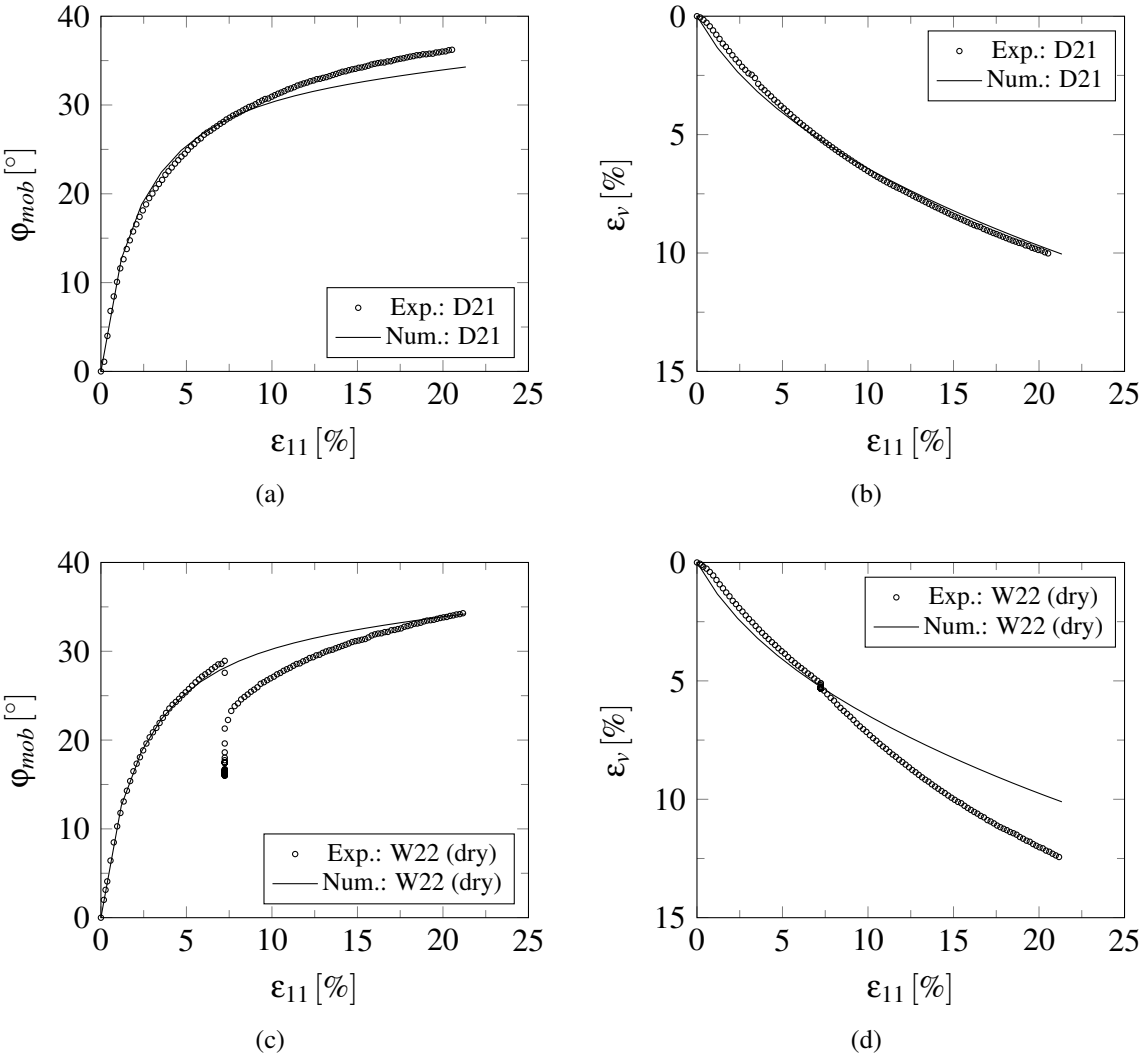

Figure 5.27: Comparison of numerical simulation with experimental data of D21∼W22 using parameters from Table 5.5

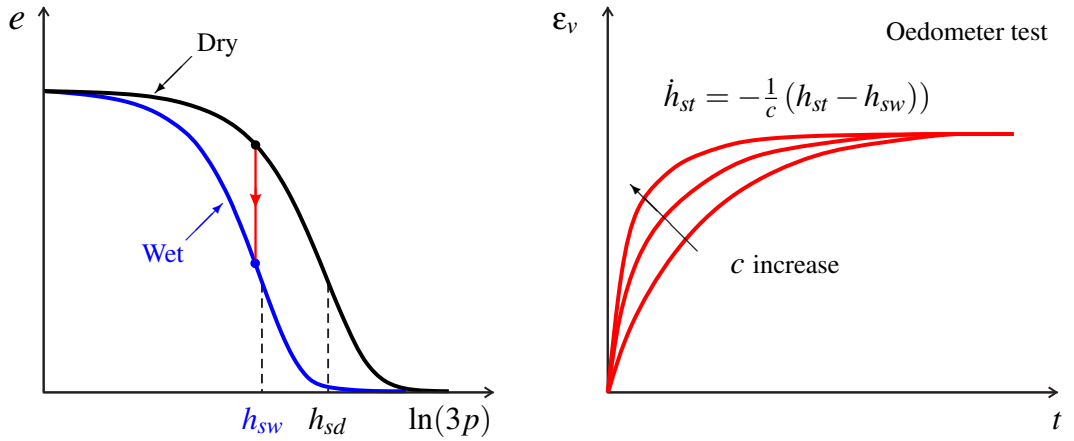

Figure 5.28: Effects of parameter c on the degradation velocity

determined in a qualitative manner. From the results shown in Fig. 5.29, with the parameter set from Table 5.5, the stress-strain and the compression behaviours are will captured by the numerical simulation. In another word, the predicted h_{sd} and h_{sw} are appropriate for this test, and if the information of compression with time is available, the parameter c can be calibrated.

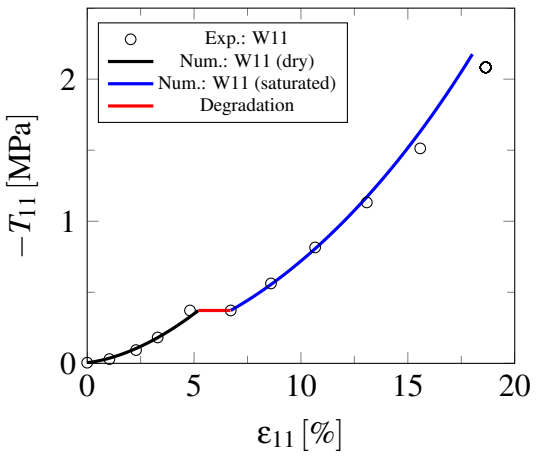

(a) Axial stress-strain results of W11

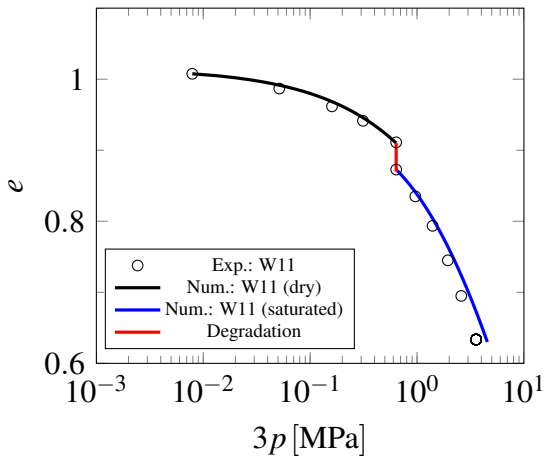

(b) Compression curves of W11

Figure 5.29: Numerical simulation results of W11 and comparison with experimental results

5.4 Calibration of parameter c and κ

With providing a value of c, the stiffness degradation can be described using the Eq. (4.1) comprehensively[4]. Note the stiffness degradation described by Eq. (3.32) will finish only when $t \to +\infty$. This can be easily seen from the follow expression

$$\dot{h}_{st} = -\frac{1}{c}(h_{sd} - h_{sw}) \exp\left\{\frac{c}{t}\right\} \tag{5.5}$$

as the $\dot{h}_{st}$ reaches to zero only when $t \to +\infty$. While this fact does not affect the Eq. (4.1) to describe the stiffness degradation in a qualitative way. With an appropriate value of c, the stiffness degradation can be well captured by Eq. (4.1). In addition, the parameter c triggers the creep velocity, but it has no influence on the final amount of creep deformation for $t \to \infty$.

Now let us try another way to calibrate parameter c. Concerning the stress relaxation test conducted by Ovalle [73] and Ovalle et al. [74], the mathematical description of the boundary conditions of the experimental tests() is $D_{11} = 0$ and $\dot{T}_{22} = \dot{T}_{33} = 0$. Then the constitutive equations can be written as follows:

$$\dot{T}_{11} = f_s \left\{ 2\hat{T}_{22} D_{22} \hat{T}_{11} + \sqrt{2} f_d \hat{a} \left(\hat{T}_{11} + \hat{T}^*_{11}\right) \mid D_{22} \mid \right\} + \frac{\dot{h}_{st}}{3h_{st}} (T_{11} + 2T_{22}) \tag{5.6}$$

$$\dot{T}_{22} = f_s \left\{ \hat{a}^2 D_{22} + 2\hat{T}_{22} D_{22} \hat{T}_{22} + \sqrt{2} f_d \hat{a} \left(\hat{T}_{22} + \hat{T}^*_{22}\right) \mid D_{22} \mid \right\} + \frac{\dot{h}_{st}}{3h_{st}} (T_{11} + 2T_{22}) \tag{5.7}$$

With considering the $D_{22} < 0$ for the experimental observation by Ovalle et al. [74], the Eq.(5.6) and Eq.(5.7) can be presented as

$$\dot{T}_{11} = f_s \left\{ \hat{T}_{22} \hat{T}_{11} - \frac{\sqrt{2}}{2} f_d \hat{a} \left(\hat{T}_{11} + \hat{T}^*_{11}\right) \right\} 2D_{22} + \frac{\dot{h}_{st}}{3h_{st}} (T_{11} + 2T_{22}) \tag{5.8}$$

$$\dot{T}_{22} = f_s \left\{ \frac{\hat{a}^2}{2} + \hat{T}^2_{22} - \frac{\sqrt{2}}{2} f_d \hat{a} \left(\hat{T}_{22} + \hat{T}^*_{22}\right) \right\} 2D_{22} + \frac{\dot{h}_{st}}{3h_{st}} (T_{11} + 2T_{22}) \tag{5.9}$$

According to Eq. (5.8), Eq. (5.9) and the relation $\dot{e} = (1+e)\,\mathrm{tr}\mathbf{D}$, the e-p relation can be described as

$$\dot{p} = -\frac{1}{3} f_s \left\{ \hat{a}^2 + \hat{T}_{22} - \frac{\sqrt{2}}{2} f_d \hat{a} \right\} \frac{\dot{e}}{1+e} - \frac{p}{h_{st}} \dot{h}_{st} \tag{5.10}$$

With a given initial condition of the stress relaxation and the first loading step, the parameter c can be calculated according to Eq. (5.9) or Eq. (5.10).

[4] Not only the creep path, but also the stress relaxation path.

However, the calibration of c according to the method mentioned above failed for all tests (W18, W19, W20 and W22). The main reason is the stress relaxation test conducted by Ovalle [73] and Ovalle et al. [74] are significantly sensitive to the loading speed, stress level and some other facts as well, as discussed by Lade [49].

In this work, the stiffness degradation is simulated with considering the degradation of the solid hardness, which is considered as a key parameter for the stiffness degradation simulation. In particular, the degradation of solid hardness is described by the Eq. (3.32). The graphic representation of the solid hardness degradation can be illustrated as Fig. 5.30a. Due to stiffness degradation, the stress relaxation path of q-t (or ε-t) shows similar trend as the one of solid hardness degradation curve (see Fig. 5.30). Without considering the effects of deviatoric stress[5] on the results of q-t and ε-t, the parameter c can be calibrated based on the characterization of the solid hardness degradation using the q-t or ε-t experimental results.

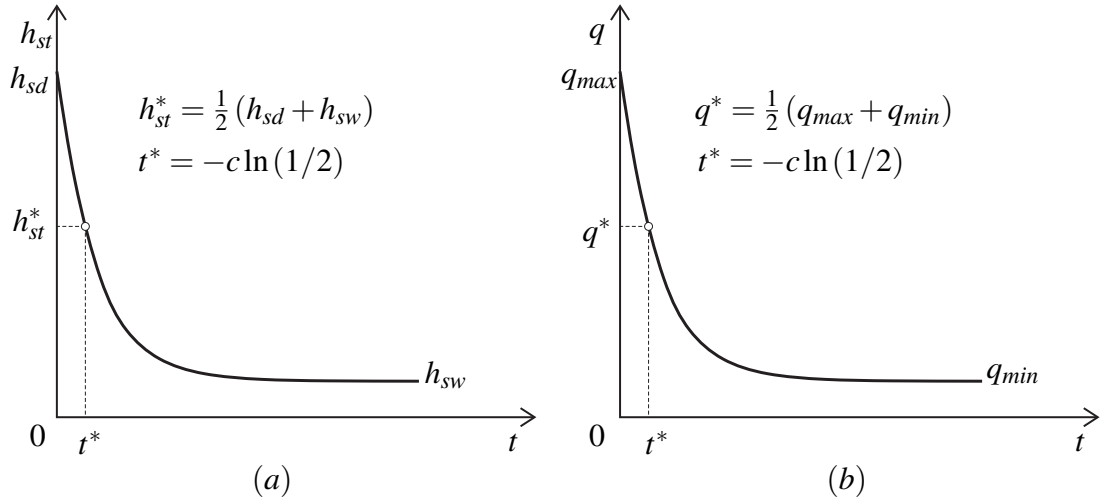

Figure 5.30: Solid hardness degradation and stress relaxation curves: (a) solid hardness degradation with time; (b) stress relaxation with time.

The parameter c can be calculated according to the equation (as mentioned in Fig. 5.30)

$$c = -\frac{t^*}{\ln(1/2)} \tag{5.11}$$

In the following the calibration process of c with respecting to the q-t experimental data is addressed.

[5] If experimental data is sufficient to study the effects of deviatoric stress on the final results of creep volumetric strain and the final results of stress relaxation, it is suggested to consider the constitutive equation proposed by Bauer [8] with the factor κ for taking into account the effects of deviatoric stress.

The experimental results of q-t from W18, W20 and W22 are summarized in Fig. 5.31. The characteristic time t^* of the tests are tabulated as well. The average value of the t^* from these three tests is $t^* = 2.1$. According to the Eq. (5.11), the parameter c can be calculated and the calibrated result of $c = 3$.

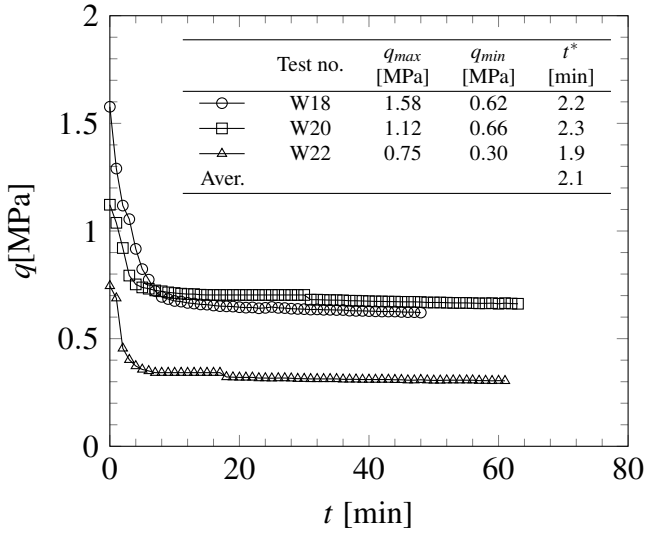

Figure 5.31: Experimental results of q-t from stress relaxation tests by Ovalle et al. [74] and the characteristic time

Therefore, considering the calibration result, $c = 3$, the numerical simulation results of q-t and e-$3p$ from W18, W20 and W22 are presented in Fig. 5.32, respectively.

It is clear to see that with the suggested parameter set from Table 5.5 and $c = 3$, the model is capable to capture the stress relaxation phenomenon qualitatively. Comparing the numerical simulation with the experimental data, the material stiffness is under-predicted by the numerical simulation. In another word, the stiffness degradation might be over-predicted, with a greater h_{sw} the numerical simulation will lead better results.

While for the quantitatively prediction of the stress relaxation phase a more sophisticated constitutive equation should be considered

$$\dot{\mathbf{T}} = f_s \left\{ \hat{a}^2 \mathbf{D} + \mathrm{tr}\left(\hat{\mathbf{T}}\mathbf{D}\right)\hat{\mathbf{T}} + f_d \hat{a} \left(\hat{\mathbf{T}} + \hat{\mathbf{T}}^*\right) \|\mathbf{D}\| \right\} + \frac{\dot{h}_{st}}{h_{st}} \left\{ \frac{1}{3}\mathrm{tr}\left(\mathbf{T}\right)\mathbf{I} + \kappa \mathbf{T}^* \right\} \tag{5.12}$$

which is similar to the constitutive equation proposed by Bauer [8]. Moreover, the κ is a parameter related to the effects of deviatoric stress on the stress-strain behaviour. Take W18 as an example, using the same parameter set from Table 5.5 and considering $c = 3$, numerical simulation results of different κ are summarized in Fig. 5.33a and Fig. 5.33b.

As it shown in Fig. 5.33a and Fig. 5.33b, the asymptotic value of deviatoric stress q from numerical simulation decreases with the increasing of κ. While the greater κ is, the less

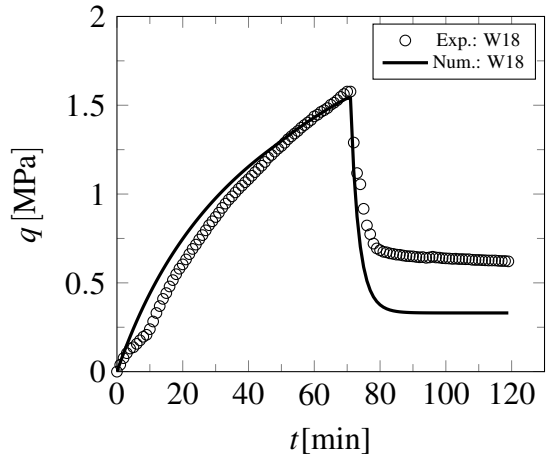

(a) Axial stress-strain results of W18

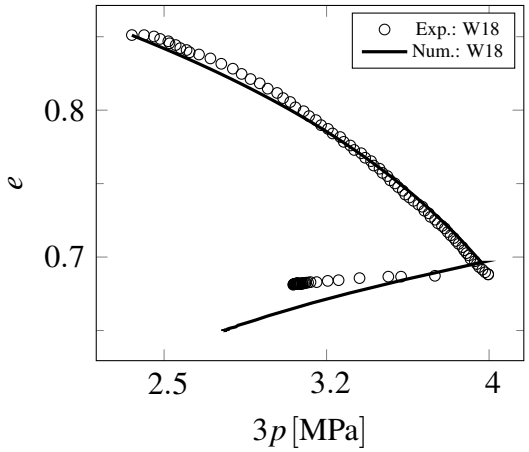

(b) Compression curves of W18

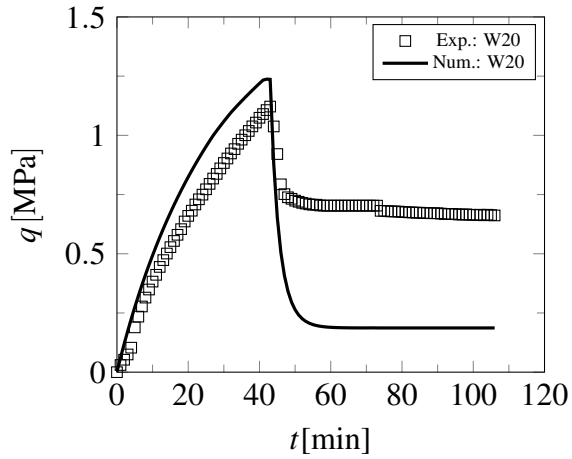

(c) Axial stress-strain results of W20

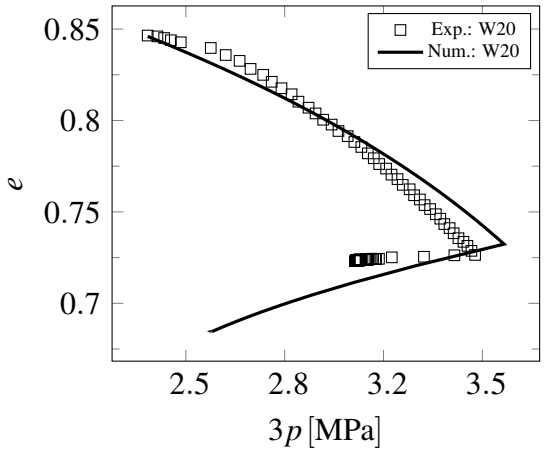

(d) Compression curves of W20

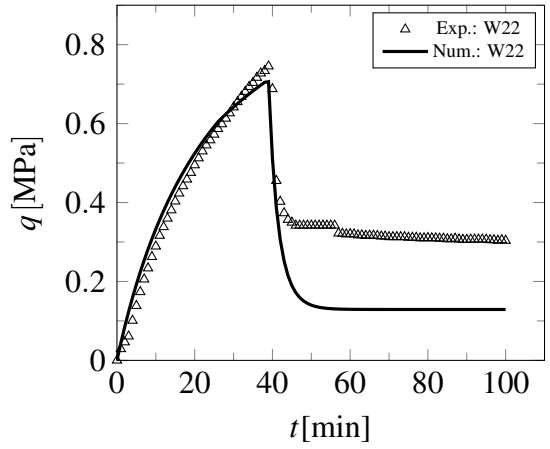

(e) Axial stress-strain results of W22

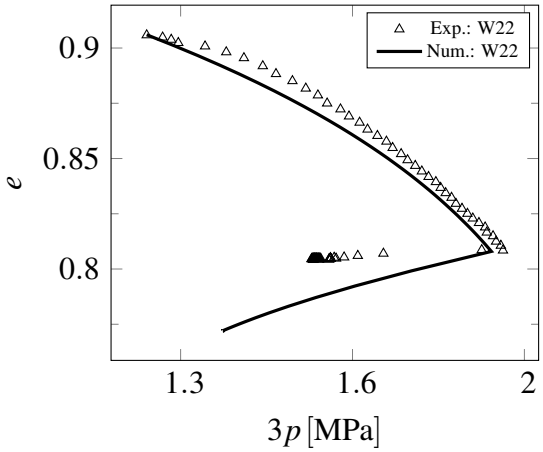

(f) Compression curves of W22

Figure 5.32: Numerical simulation results using the parameter set from Table 5.5 and comparison with experimental results

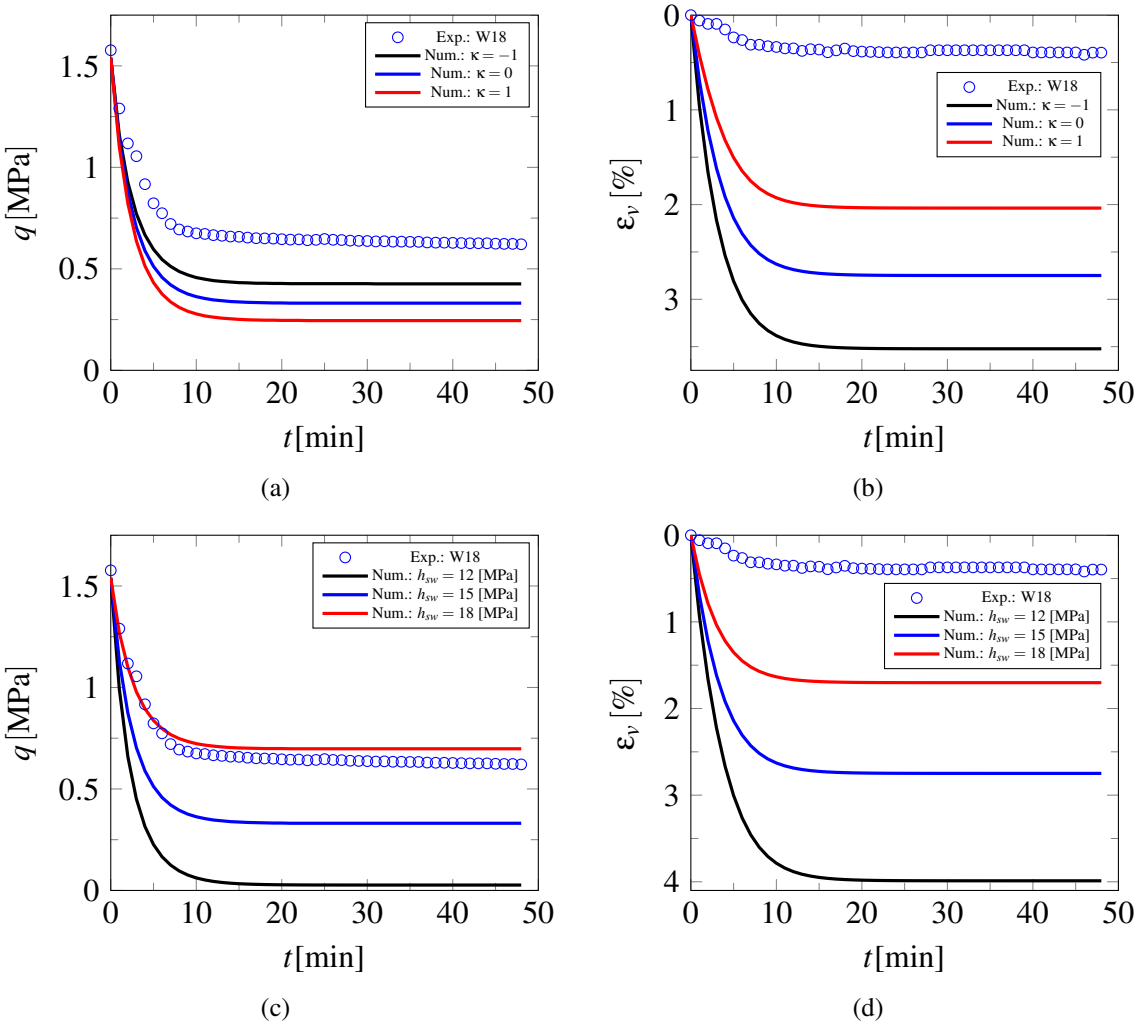

Figure 5.33: Parametric study of κ and h_{sw}, and the comparison with experimental results

volumetric strain will be predicted by the model. The deviatoric stress has effects on the stress strain behaviour of the material in the stress relaxation (or stiffness degradation) phase. However, good agreement with experimental data cannot be achieved by adjusting the parameter κ only. This support the idea mentioned before that the stiffness degradation is over-predicted. Parametric study of h_{sw} is summarized in Fig. 5.33c and Fig. 5.33d.

Therefore, it is possible to approach a good agreement with the experimental results using a parameter set of h_{sw} and κ. The results of numerical simulation with $h_{sw} = 18.5$ MPa and $\kappa = 2.4$ are presented in Fig. 5.34.

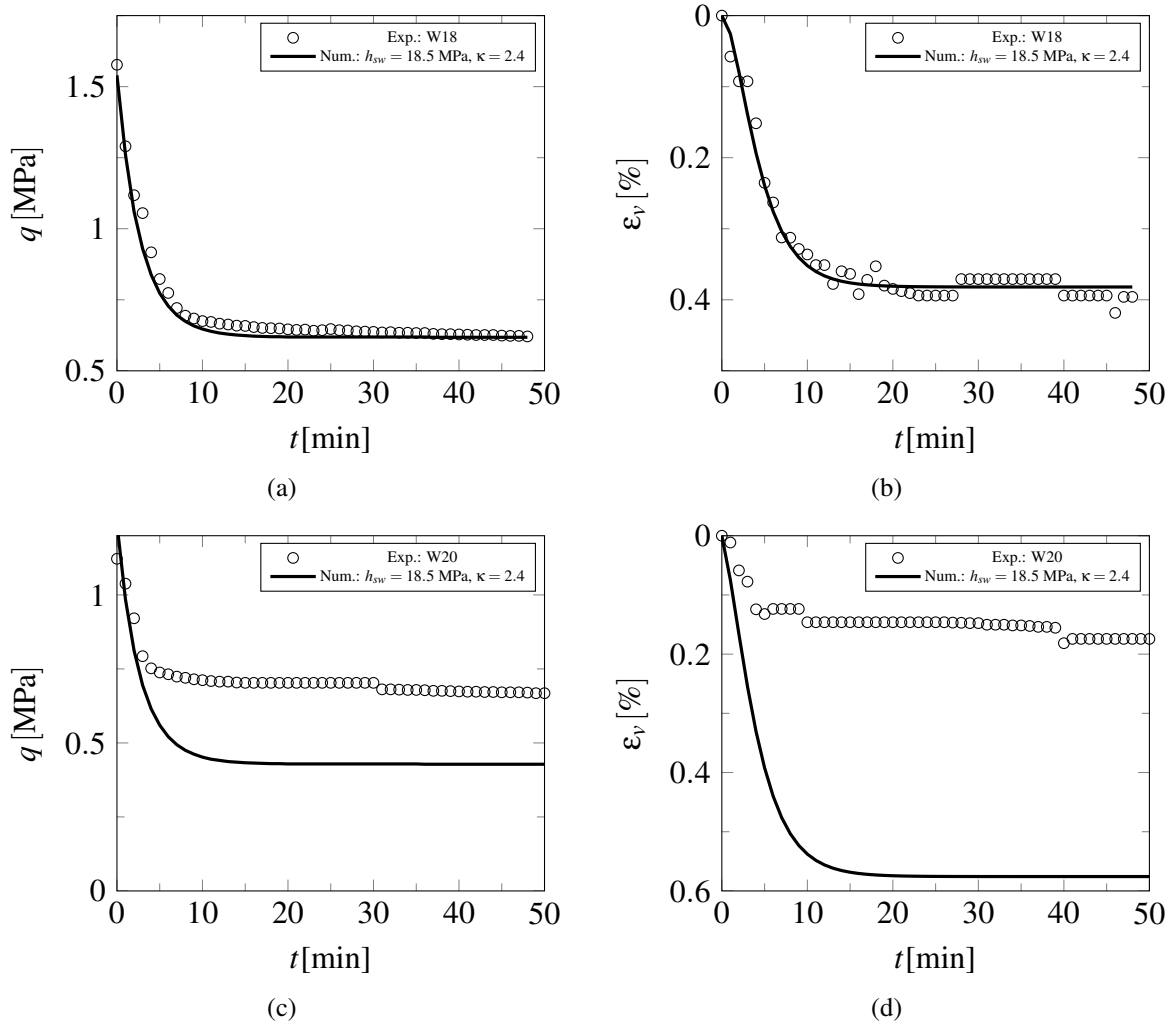

Figure 5.34: Stress relaxation simulation results of W18 and W20 with $h_{sw} = 18.5$ MPa, $\kappa = 2.4$

Based on the testing of different combination of h_{sw} and κ, the suggested parameter set is $h_{sw} = 20$ MPa and $\kappa = 2$. And the q-t and ε-t results of numerical simulation are summa-

rized in Fig. 5.35. As it can be seen in Fig. 5.35, it is difficult to find a unique parameter

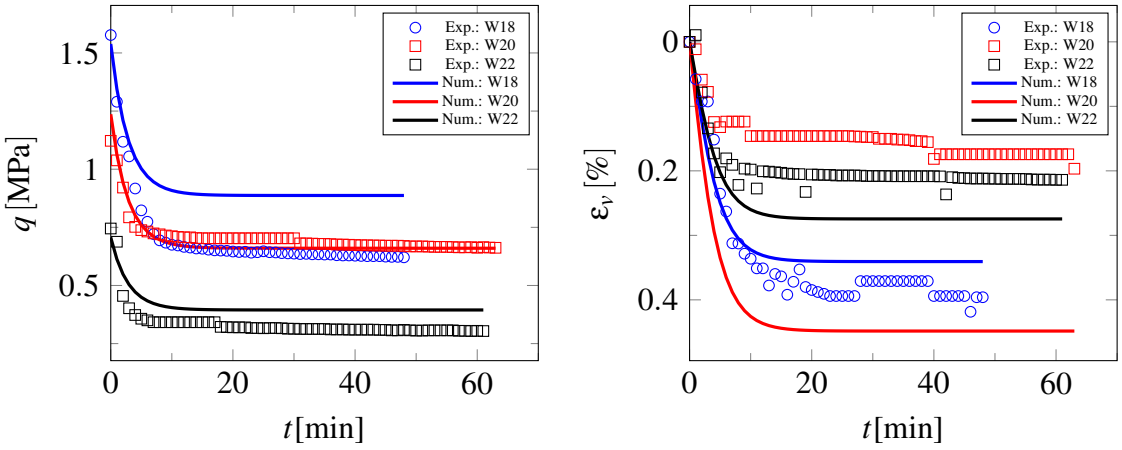

Figure 5.35: Stress relaxation simulation results of with $h_{sw} = 20$ MPa, $\kappa = 2$

set of h_{sw} and κ which is appropriate for all these three tests, W18, W20 and W22. According to the available experimental data, the parameter set for the extended version of constitutive model is tabulated as follow

Table 5.6: The proposed parameter set for shale quartzite sand with stiffness degradation

	φ_c [°]	h_{sd} [MPa]	h_{sw} [MPa]	n [-]	e_{i0} [-]	e_{c0} [-]	$\check{\alpha}$ [-]	c [min]	κ [-]
Dry	40	23.6	/	0.6	1.3	0.8	0.5	3	2
Saturated	40	/	20	0.6	1.3	0.8	0.5	3	2

The numerical simulation results have a good agreement with the experimental data, especially the numerical simulation of test W20 and W22. This means the $h_{sw} = 20$ MPa is more appropriate than the previous calibrated $h_{sw} = 15$ MPa. The main reason might be the oedometric compression data used for calibration leads a lower h_{sw}. In particular, as mentioned by Ovalle et al. [74], the settlement (or strain) from the oedometric compression test was measured after 1 hour strain stabilization, it is uncertain that whether an additional creep deformation is taken into account or not (see Fig. 5.37)

As illustrated in Fig. 5.37, the strain stabilization phase might lead additional settlement (vertical red line in the figure). The additional settlement could affect the calibration result of h_s, if the additional settlement is not small enough and cannot be neglected. The additional settlement of saturated material can be greater than the one of dry material, because of the appearance of water particle can move or rearrange more easily. This could be an explanation why the previous predicted $h_{sw} = 15$ MPa is not appropriate for the stress

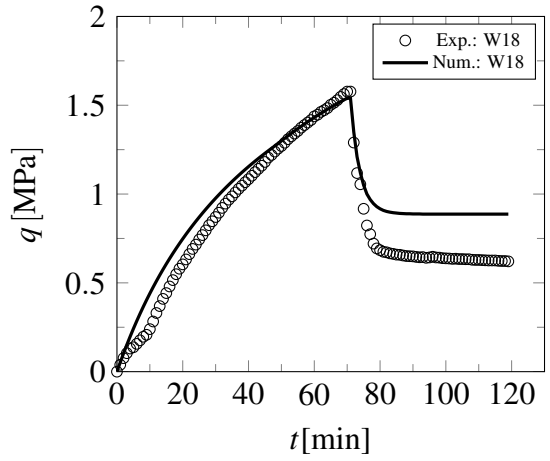

(a) Axial stress-strain results of W18

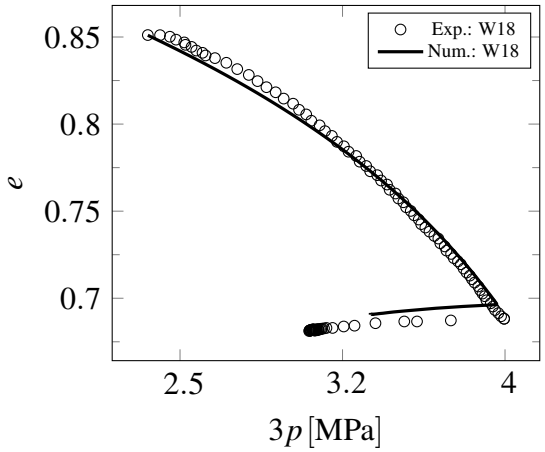

(b) Compression curves of W18

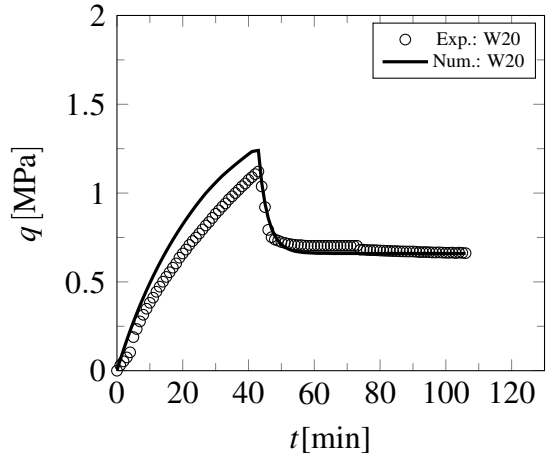

(c) Axial stress-strain results of W20

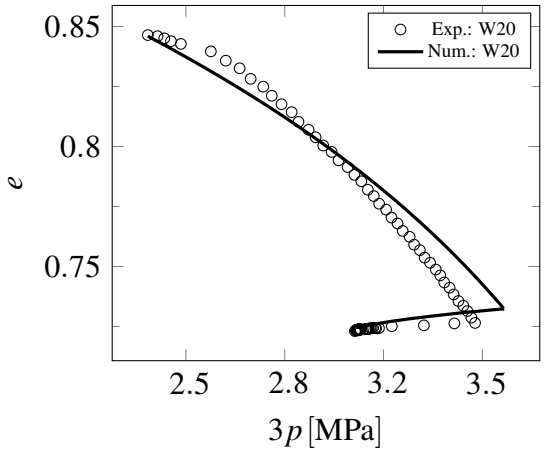

(d) Compression curves of W20

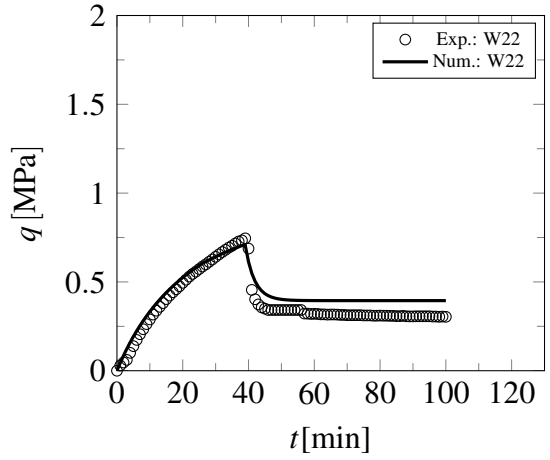

(e) Axial stress-strain results of W22

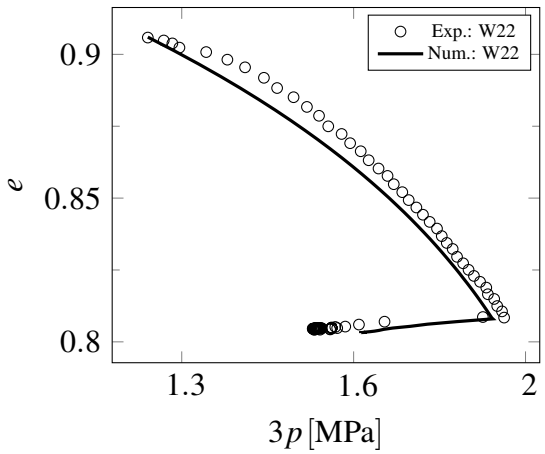

(f) Compression curves of W22

Figure 5.36: Numerical simulation results using the parameter set from Table 5.6

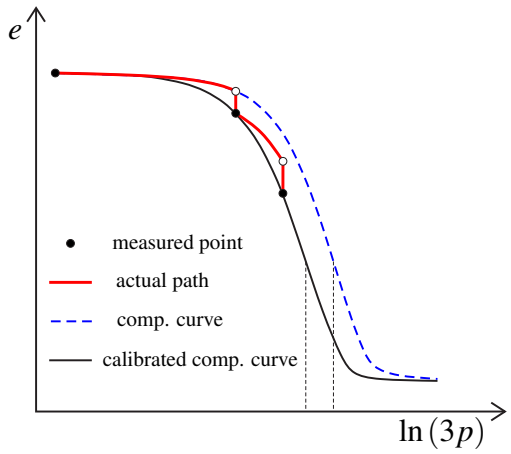

Figure 5.37: The effect of additional settlements on calibration of h_s

relaxation simulation. If possible, further experimental investigation using the same material to study the effects of additional settlement of strain stabilization phase is of great interest.

From the numerical simulation results shown in Fig. 5.24-Fig. 5.27, the parameter set suggested in Table 5.5 is appropriate for the dry and saturated material. While for the stiffness degradation simulation, numerical results using parameter set from Table 5.6 have better agreement with experimental investigation results. Note all these parameter sets in Table 5.5 and Table 5.6 are suggested based on the comprehensive study and analysis of the available experimental data. It is suggested to consider simple constitutive equation (Eq. (4.1) with considering constant h_s) and fewer parameters (6 parameters in total, see Table 5.5) for simulation of dry or saturated material, while for the complex stiffness degradation it is better to consider the comprehensive constitutive model (Eq. (5.12)) and 9 parameters (Table 5.6) to approach better agreements with experimental results during the transition from the dry to saturation.

In addition, the critical friction angle of the shale quartzite sand is $\varphi_c = 40^\circ$, which is out of the range (22-35°) for Quartz (suggested by Terzaghi et al. [86]), and greater than the value of most of the sands summarized in Sadrekarimi and Olson [79]. The main reason is the shale quartzite sand is not a natural sand which was rounded by natural factors. This sand is obtained from grinding of the quartzite shale rock as mentioned before. Therefore, the suggestion of $\varphi_c = 40^\circ$ for this angular and flat material is reasonable.

6 Summary and concluding remarks

In this thesis a hypoplastic constitutive model by Bauer is considered which takes into account the mechanical behaviour of weathered and moisture sensitive, coarse-grained granular materials under both dry and wet conditions with a single set of material parameters. The model describes a degradation of the incremental stiffness when the moisture content of the solid material increases. The degradation of the incremental stiffness is a time dependent process and influenced by the current pressure dependent relative density and the stress state. In this thesis the two density factors in the original version by Bauer are simplified, which results in a reduction of the number of material parameters required. For the so-called simplified constitutive model the relevant stiffness factor is derived from a consistency condition. Based on a parameter study the properties of the simplified model proposed is investigated. To investigate the performance of the model, the experimental data obtained with shale quartzite sand by Ovalle [73] and Ovalle et al. [74] are used in this study. For determining the constitutive parameters it turns out that the data available are not sufficient to use a direct calibration procedure. Thus, a specific calibration procedure is developed to estimate the missing data.

The following conclusions can be drawn: It is recommended to plane the experimental investigations with respect to the data required for a direct calibration procedure of the constitutive parameters required for the model used for prediction. If the direct calibrations of all parameters cannot be carried out due to the lack of experimental data, a specific calibration procedure is needed. In this context it can also be noted that for highly nonlinear equations the calibration of the parameters using back analysis or an optimization procedure can fail. A careful evaluation of the experimental data used for the calibration is also important in particular when shear banding takes place in the laboratory test. Thus, the calibration procedure cannot be automated for general cases. An individual adaptation is need which can be a challenging task.

A Appendix

A.1 Characteristics of compression law by Bauer (1996)

According to the compression equation by Bauer(1996), see Eq. (3.23), the derivation of void ratio can be derived as follows[1]:

$$\begin{aligned}
\frac{de_i}{dx} &= \frac{d}{dx}\left\{ e_{i0} \exp\left[-\left(\frac{3p}{h_s}\right)^n \right] \right\} \\
&= e_{i0} \frac{d}{dx}\left\{ \exp\left[-\left(\frac{3p}{h_s}\right)^n \right] \right\} \\
&= e_{i0} \exp\left[-\left(\frac{3p}{h_s}\right)^n \right] \frac{d}{dx}\left[-\left(\frac{3p}{h_s}\right)^n \right] \\
&= e_{i0} \exp\left[-\left(\frac{3p}{h_s}\right)^n \right] (-n) \left(\frac{3p}{h_s}\right)^{n-1} \frac{d}{dx}\left(\frac{3p}{h_s}\right) \\
&= e_{i0} \exp\left[-\left(\frac{3p}{h_s}\right)^n \right] (-n) \left(\frac{3p}{h_s}\right)^{n-1} \frac{3}{h_s}\frac{dp}{dx} \\
&= e_{i0} \exp\left[-\left(\frac{3p}{h_s}\right)^n \right] (-n) \left(\frac{3p}{h_s}\right)^{n-1} \frac{3p}{h_s}\frac{1}{p}\frac{dp}{dx} \\
&= e_{i0} \exp\left[-\left(\frac{3p}{h_s}\right)^n \right] (-n) \left(\frac{3p}{h_s}\right)^{n} \frac{1}{p}\frac{dp}{dx}
\end{aligned} \tag{A.1}$$

The compression equation can be rewritten as:

$$e_i = e_{i0} \exp\left[-\left(\frac{3p}{h_s}\right)^n \right] \quad \Rightarrow \quad e_{i0} \exp\left[-\left(\frac{3p}{h_s}\right)^n \right] = e_i$$

$$e_i = e_{i0} \exp\left[-\left(\frac{3p}{h_s}\right)^n \right] \quad \Rightarrow \quad \left(\frac{3p}{h_s}\right)^n = -\ln\left(\frac{e_i}{e_{i0}}\right)$$

[1] Considering x is the variable.

Therefore, the derivative of void ratio can be represented as:

$$\frac{de_i}{dx} = e_{i0} \exp\left[-\left(\frac{3p}{h_s}\right)^n\right](-n)\left(\frac{3p}{h_s}\right)^n \frac{1}{p}\frac{dp}{dx}$$

$$= e_i(-n)\left[-\ln\left(\frac{e_i}{e_{i0}}\right)\right]\frac{1}{p}\frac{dp}{dx}$$

$$= e_i n \ln\left(\frac{e_i}{e_{i0}}\right)\frac{1}{p}\frac{dp}{dx}$$

$$\rightsquigarrow \qquad \dot{e}_i = e_i n \ln\left(\frac{e_i}{e_{i0}}\right)\frac{\dot{p}}{p} \tag{A.2}$$

With respect different representation, i.e. $e \sim p$, $e \sim 3p$, $e \sim \ln(3p)$, the slope of the graphical representation can be derived explicitly according to Eq. (A.2).

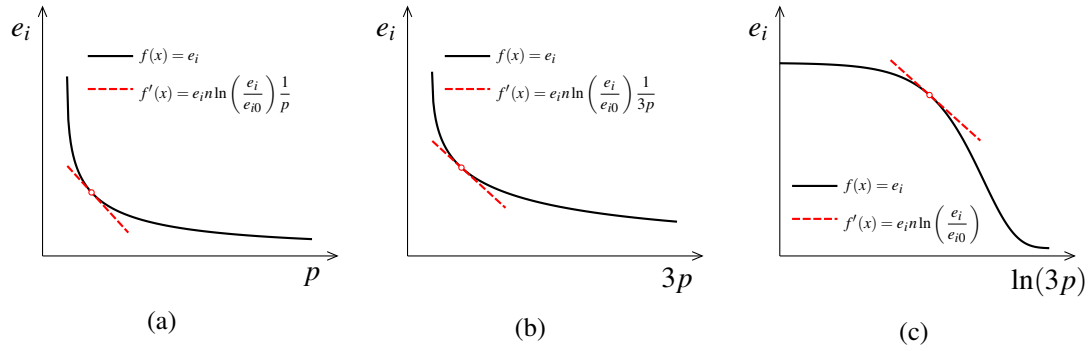

Figure A.1: Compression curve: (a)in normal representation as $e \sim p$; (b)in normal representation as $e \sim 3p$; (c)in semi-logarithmic representation as $e \sim \ln(3p)$.

Considering the maximum void ratio e_i is a function represented as $y = e_i$, with respect the $x = \ln(3p)$, the compression equation by Bauer (1996) can be expressed as $y = f(x)$ explicitly as:

$$f(x) = f(x_0) \exp\left\{-\left(\frac{\exp x}{h_s}\right)^n\right\} \tag{A.3}$$

Now using primes for derivatives $\frac{d}{dx}$ with respect to x, the first derivative is:

$$y' = y_0 \left\langle \exp\left\{-\left[\frac{\exp(x)}{h_s}\right]^n\right\}\right\rangle'$$

$$= y_0 \exp\left\{-\left[\frac{\exp(x)}{h_s}\right]^n\right\}(-n)\left[\frac{\exp(x)}{h_s}\right]^{n-1}\left[\frac{\exp(x)}{h_s}\right]'$$

$$= y_0 \exp\left\{-\left[\frac{\exp(x)}{h_s}\right]^n\right\}(-n)\left[\frac{\exp(x)}{h_s}\right]^n$$

$$= -yn\left[\frac{\exp(x)}{h_s}\right]^n \tag{A.4}$$

the second derivative is:

$$y'' = -y'n\left[\frac{\exp(x)}{h_s}\right]^n - y\left\{n\left[\frac{\exp(x)}{h_s}\right]^n\right\}'$$

$$= yn^2\left[\frac{\exp(x)}{h_s}\right]^{2n} - yn^2\left[\frac{\exp(x)}{h_s}\right]^n$$

$$= yn^2\left[\frac{\exp(x)}{h_s}\right]^n\left\{\left[\frac{\exp(x)}{h_s}\right]^n - 1\right\} \tag{A.5}$$

and then the curvature is:

$$\kappa = \frac{y''}{(1+y'^2)^{\frac{3}{2}}}$$

$$= \frac{yn^2\left[\frac{\exp(x)}{h_s}\right]^n\left\{\left[\frac{\exp(x)}{h_s}\right]^n - 1\right\}}{\left\{1+y^2n^2\left[\frac{\exp(x)}{h_s}\right]^{2n}\right\}^{\frac{3}{2}}} \tag{A.6}$$

A.2 Asymptotic behaviour of proportional loading paths

Based on the experimental investigation of sand using true triaxial apparatus, Goldscheider [21] discovered that proportional stretching starting from the stress free state, reached in a proportional stress path. For an arbitrary initial stress state different from zero, the same proportional stretching leads to a stress path which asymptotically approaches the same stress path starting from the stress free state. This finding is of great importance for developing and validation of constitutive models. The proportional paths under an axisymmetric condition ($D_{22} = D_{33}$ and $T_{22} = T_{33}$) is illustrated as in Fig. A.2.

As shown in Fig. A.2c, for undrained compression, $D_{22} = -D_{11}/2$, the corresponding stress path trends towards the critical stress surface. The proportional strain paths with $\mathrm{tr}(\mathbf{D}) = 0$ form the boundary of strain paths under loading conditions. It can be considered that the proportional stress paths function as attractors (Medicus [61]). Details of graphical representation of proportional paths can be referred to Gudehus and Mašín [23].

Considering the Goldscheider's findings as fundamental rules, Kolymbas [46] and Medicus et al. [62] proposed the concept of Barodesy, which allows a rather simple mathematical description. The asymptotic behaviour is also a property of hypoplastic models.

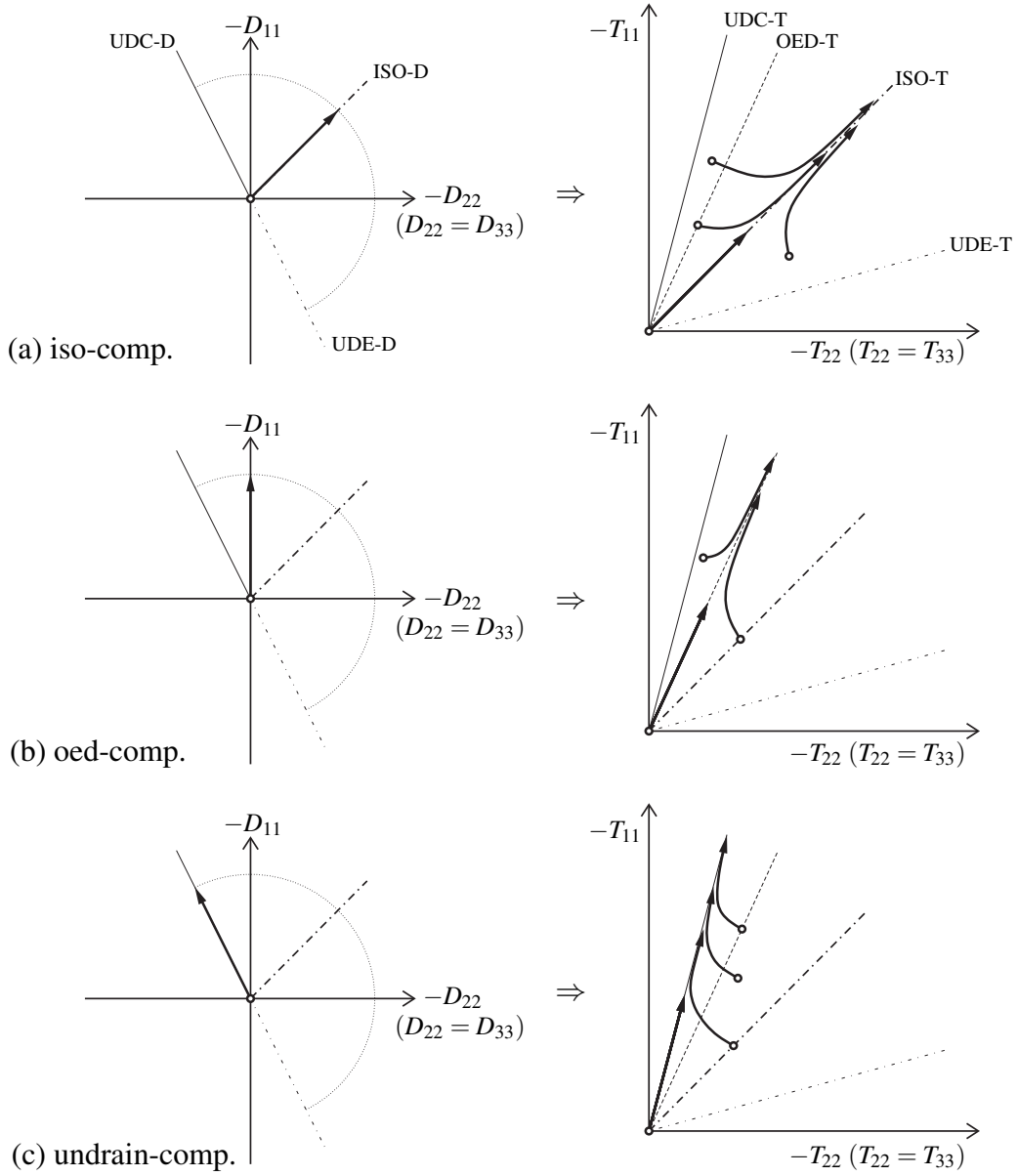

Figure A.2: Illustration of proportional paths and asymptotic behaviour under axisymmetric condition: (a) isotropic compression; (b) oedometric compression; (c) undrained compression.

A.3 Computer program HET for element tests

For the numerical simulation of element tests of the simplified hypoplastic model discussed in Chapter 4 a computer program was developed. The program HET (Hypoplastic Element Tests) is written in Python, MATLAB and LaTeX language. The codes for element tests are written in MATLAB. Moreover, the pre- and post-processing are designed by Python scripts. The report of the each simulation is generated by LaTeX.

For the HET program, the flowchart, the user interface and the input interface are presented in Fig. A.3, Fig. A.4 and Fig. A.5, respectively. The library of element tests is outlined in Section A.3.1. For a triaxial compression test and a specific set of parameters the report obtained from HET program is shown in Section A.3.2. The source code of HET program for triaxial element test is presented in Section A.3.3.

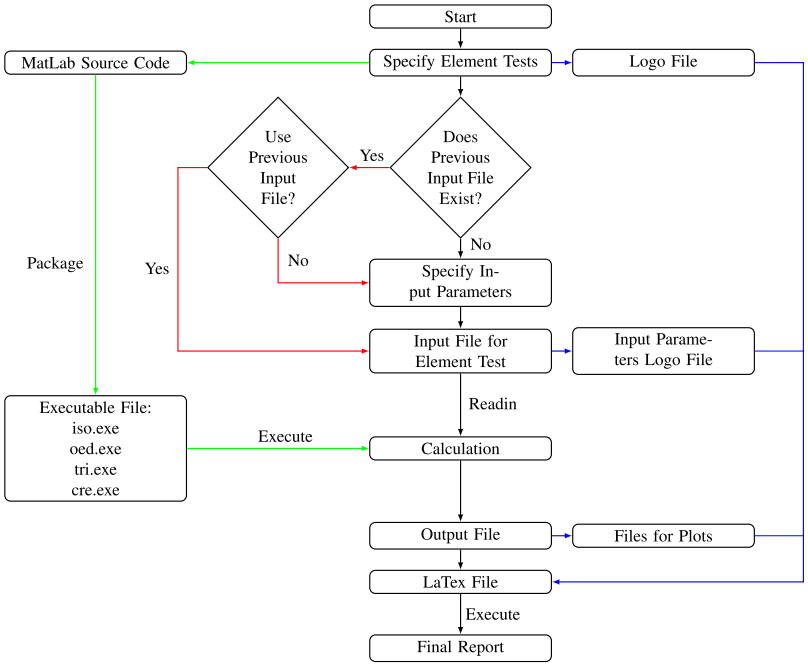

Figure A.3: Flowchart of HET

A.3.1 Library of element tests

The element test library of HET includes the following tests:

- Compression tests:
  - Isotropic compression test

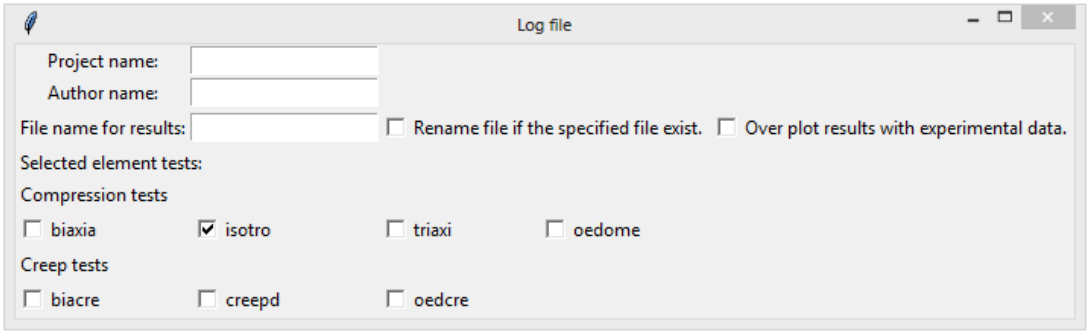

Figure A.4: Login interface of HET

  - Oedometric compression test
  - Triaxial compression test
  - Biaxial compression test
- Creep tests:
  - True-triaxial-creep test (including isotropic-creep test)
  - Oedometric-creep test
  - Biaxial-creep test

According to the general equation (Eq. (4.1)), the constitutive equation considered in HET is as follow:

$$\dot{\mathbf{T}} = f_s \left\{ c_1 \hat{a}^2 \mathbf{D} + c_2 \operatorname{tr}(\mathbf{D})\mathbf{I} + c_3 \operatorname{tr}\left(\hat{\mathbf{T}}\mathbf{D}\right)\hat{\mathbf{T}} + c_4 f_d \hat{a} \left(\hat{\mathbf{T}} + c_5 \hat{\mathbf{T}}^*\right) \|\mathbf{D}\| \right\} + c_6 \frac{\dot{h}_{st}}{h_{st}} \left\{ \tfrac{1}{3} \operatorname{tr}(\mathbf{T})\mathbf{I} + \kappa \mathbf{T}^* \right\} \quad \text{(A.7)}$$

with $c_1 \sim c_6$ are factors for switching on/off of individual terms. Considering the possibility of modification, the component $\operatorname{tr}(\mathbf{D})\mathbf{I}$ is added into the constitutive equation and the aforementioned component $\kappa\mathbf{T}^*$ is still kept in the general equation. For the simplified constitutive model used in this work, the factors and κ are set as: $c_1 = 1$, $c_2 = 0$, $c_3 = 1$, $c_4 = 1$, $c_5 = 1$ and $\kappa = 0$. $c_6 = 0$ for time-independent case (h_{sd} or h_{sw} is constant) and $c_6 = 1$ for time-dependent condition ($h_{st} \neq$ const.). Note that the strain controlled loading process is considered for ensuring the strain softening condition is included.

The MATLAB source code of each element tests is packaged into a standalone executable file using the following command. This is only an illustration how to package standalone executable file without MS-DOS Command Window under Windows Operation System. For other operation system like Linux is not covered here.

```
% Matlab compiler for standalone executable file without
% Command Window
% Input: filename, here is <het_v005_trirel>
```

```
% Output: het_v005_trirel.exe
mcc -e het_v005_trirel
% mcc: invokes the MATLAB Compiler.
% -e : Suppresses appearance of the MS-DOS Command Window
% when generating a standalone application.
% het_v005_trirel: filename without extension.
```

After finishing the packaging, an executable file with the same name as specified in the command line will be crated (here is het_v005_trirel.exe). With the corresponding version of the MCRInstaller.exe installed on the computer, the standalone executable file can be executed without running MATLAB or evening without installing MATLAB. Therefore, the HET program only requires Python language, MCRInstaller file, LaTeX installed on the computer.

designing user interface (see Fig. A.4), calling MATLAB standalone executable file for calculation, preparing simulation results and latex files, and finally generate calculation report (see the flowchart of HET in Fig. A.3). This basic programming work has significant importance for validation of constitutive model and for calibration of parameters, especially for the case that some necessary parameters are missing and iteration process should be considered.

In order to prevent to reach infinite stress for the case which the maximum strain is specified over the limit strain of the material, specify a maximum stress range ($\sigma_{11,max}$ in Fig. A.5) is helpful.

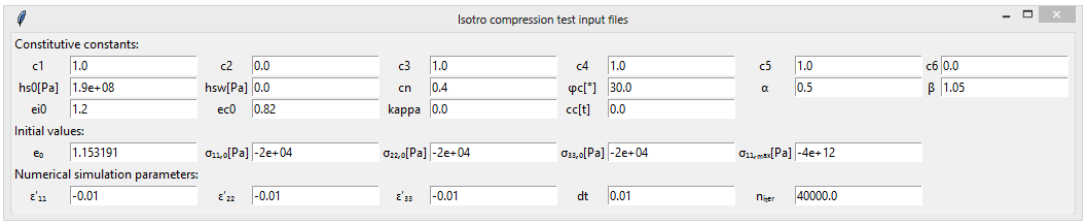

Figure A.5: Parameter input interface of HET

After parameter inputting process, the HET program calls the corresponding element test calculation file (here is the isotropic compression element test, het_iso.exe.). When the calculation has been done, HET program generate the data files according to a predefined file set for each element test, and generate the corresponding LaTeX files for the calculation report. In the report of HET, the results of stress and strain is represented with the sign convention of Soil Mechanics, in order to keep it simple for comparison with the experimental results, which in many literature the sign convention is considered the same as the one in Soil Mechanics.

A.3.2 Representation of the results

triaxi compression Linke Li

Program:	HET_v005; het_v005_triaxi.exe
Author:	Linke Li
Date:	Jan. 17, 2018
File no.:	17Jan181153

1 HET 2018

Based on the constitutive model proposed by Bauer (2009), a modified constitutive model used in the current version of HET is as follow:

$$\overset{\circ}{\mathbf{T}} = f_s\left\{c_1\hat{a}^2\overset{4}{\mathbf{I}}:\mathbf{D} + c_2\,\mathrm{tr}(\mathbf{D})\,\mathbf{I} + c_3\hat{\mathbf{T}}\otimes\hat{\mathbf{T}}:\mathbf{D} + c_4 f_d\hat{a}\left(\hat{\mathbf{T}} + c_5\hat{\mathbf{T}}^*\right)\|\mathbf{D}\|\right\} + c_6\frac{\dot{h}_{st}}{h_{st}}\left\{\frac{1}{3}\,\mathrm{tr}(\mathbf{T})\,\mathbf{I} + \kappa\mathbf{T}^*\right\} \tag{1}$$

$$\dot{h}_{st} = -\frac{1}{c}\{h_{st} - h_{sw}\} \tag{2}$$

here parameters $c_1 \sim c_6$ are factors for switching on or off the corresponding components of the equation. In the current version, the c_2 is set as $c_2 = 0$. c_1, c_3, c_4 and c_5 are set equal to 1. c_6 is the switch factor for the component related to stiffness degradation. For the calculation without stiffness degradation, $c_6 = 0$.

$\overset{\circ}{\mathbf{T}}$ is the effective objective stress rate tensor, which in conventional soil mechanics is written in the effective Cauchy stress form. $\overset{4}{\mathbf{I}}$ is the fourth order unit tensor. $\mathbf{D}$ is the strain rate tensor. $\hat{\mathbf{T}}$ is the normalised stress tensor, $\mathbf{T}^*$ and $\hat{\mathbf{T}}^*$ are the deviatoric quantities. $\hat{a}$, b_p, n_p and b_{sd} are constitutive parameters. In particular, the $\hat{a}$ is a factor related to critical behaviour of the material, b_p and n_p are parameters related mean pressure effect on solid hardness degradation, and b_{sd} is the one related the deviatoric stress effect on solid hardness degradation.

Using stress and strain components, the eq.(1) can be represented as:

$$\overset{\circ}{\sigma}_{ij} = f_s\left\{c_1\hat{a}^2\dot{\varepsilon}_{ij} + c_2\dot{\varepsilon}_{mm} + c_3\hat{\sigma}_{kl}\dot{\varepsilon}_{kl}\hat{\sigma}_{ij} + c_4 f_d\hat{a}\left(\hat{\sigma}_{ij} + c_5\hat{\sigma}^*_{ij}\right)\sqrt{\dot{\varepsilon}_{kl}\dot{\varepsilon}_{kl}}\right\} \tag{3}$$

herein,

$$\hat{a} = \frac{\sin\varphi_c}{3-\sin\varphi_c}\times\left[\sqrt{\frac{8/3 - 3\left(\hat{\sigma}^*_{kl}\hat{\sigma}^*_{kl}\right) + g'\left(\hat{\sigma}^*_{kl}\hat{\sigma}^*_{kl}\right)^{3/2}}{1 + g'\left(\hat{\sigma}^*_{kl}\hat{\sigma}^*_{kl}\right)^{1/2}}} - \sqrt{\hat{\sigma}^*_{kl}\hat{\sigma}^*_{kl}}\right] \quad \text{and} \quad g' = -3\frac{\hat{\sigma}^*_{kl}\hat{\sigma}^*_{lm}\hat{\sigma}^*_{mk}}{\left(\hat{\sigma}^*_{pq}\hat{\sigma}^*_{pq}\right)^{3/2}}$$

and

$$f_d = \left(\frac{e}{e_c}\right)^{\alpha} \tag{4}$$

$$f_s = \frac{f_e f_b}{\hat{\sigma}_{kl}\hat{\sigma}_{kl}} \tag{5}$$

wherein

$$f_e = \left(\frac{e_c}{e}\right)^{\beta} \quad \text{and} \quad f_b = \frac{1+e_i}{e_i}\frac{h_{st}^n}{nh_i}\{-\mathrm{tr}(\mathbf{T})\}^{1-n}\left(\frac{e_{i0}}{e_{c0}}\right)^{\beta}$$

$$h_i = 3c_1\hat{a}_i^2 + 9c_2 + c_3 - \sqrt{3}c_4\hat{a}_i\left(\frac{e_{i0}}{e_{c0}}\right)^{\alpha} \quad \text{and} \quad \hat{a}_i = \sqrt{\frac{8}{3}}\frac{\sin\varphi_c}{3-\sin\varphi_c}$$

2 Triaxial compression test without stiffness degradation

The triaxial compression test is actually true triaxial compression test with considering the lateral stresses keep constant. Then the boundary condition for the triaxial compression test is:

$$\dot{\sigma}_{22} = \dot{\sigma}_{33} = 0 \tag{6}$$

With prescribed initial stresses and vertical strain rate, the constitutive equations of triaxial compression are as follow:

$$\begin{aligned}\dot{\sigma}_{11} = f_s \{ & c_1 \hat{a}^2 \dot{\varepsilon}_{11} + c_2 (\dot{\varepsilon}_{11} + \dot{\varepsilon}_{22} + \dot{\varepsilon}_{33}) + c_3 (\hat{\sigma}_{11}\dot{\varepsilon}_{11} + \hat{\sigma}_{22}\dot{\varepsilon}_{22} + \hat{\sigma}_{33}\dot{\varepsilon}_{33}) \hat{\sigma}_{11} \\ & + c_4 f_d \hat{a} \left(\hat{\sigma}_{11} + c_5 \hat{\sigma}^*_{11}\right) \sqrt{\dot{\varepsilon}^2_{11} + \dot{\varepsilon}^2_{22} + \dot{\varepsilon}^2_{33}} \Big\}\end{aligned} \tag{7}$$

$$\begin{aligned}\dot{\sigma}_{22} = f_s \{ & c_1 \hat{a}^2 \dot{\varepsilon}_{22} + c_2 (\dot{\varepsilon}_{11} + \dot{\varepsilon}_{22} + \dot{\varepsilon}_{33}) + c_3 (\hat{\sigma}_{11}\dot{\varepsilon}_{11} + \hat{\sigma}_{22}\dot{\varepsilon}_{22} + \hat{\sigma}_{33}\dot{\varepsilon}_{33}) \hat{\sigma}_{22} \\ & + c_4 f_d \hat{a} \left(\hat{\sigma}_{22} + c_5 \hat{\sigma}^*_{22}\right) \sqrt{\dot{\varepsilon}^2_{11} + \dot{\varepsilon}^2_{22} + \dot{\varepsilon}^2_{33}} \Big\} = 0\end{aligned} \tag{8}$$

$$\begin{aligned}\dot{\sigma}_{33} = f_s \{ & c_1 \hat{a}^2 \dot{\varepsilon}_{33} + c_2 (\dot{\varepsilon}_{11} + \dot{\varepsilon}_{22} + \dot{\varepsilon}_{33}) + c_3 (\hat{\sigma}_{11}\dot{\varepsilon}_{11} + \hat{\sigma}_{22}\dot{\varepsilon}_{22} + \hat{\sigma}_{33}\dot{\varepsilon}_{33}) \hat{\sigma}_{33} \\ & + c_4 f_d \hat{a} \left(\hat{\sigma}_{33} + c_5 \hat{\sigma}^*_{33}\right) \sqrt{\dot{\varepsilon}^2_{11} + \dot{\varepsilon}^2_{22} + \dot{\varepsilon}^2_{33}} \Big\} = 0\end{aligned} \tag{9}$$

Since axial strain loading control is taken into account, only $\dot{\varepsilon}_{22}$ and $\dot{\varepsilon}_{33}$ are unknown quantities, the equation system of eq.(8) and (9), can be solved by numerical iteration method, such as Newton iteration method. The disadvantage of Newton iteration method is the initial guess of the unknown variables should be given. If the prediction of the unknown variables is not well done, the Newton iteration method might not able to reach a solution. However, at the beginning of the test, the strain rate are really small, a prediction of $\dot{\varepsilon}_{22}$ and $\dot{\varepsilon}_{33}$ as close to zero is a good choice.

3 Parameters

The constitutive parameters are as following:

Constitutive constants:

c_1	c_2	c_3	c_4	c_5	c_6	h_{sd} [MPa]	h_{sw} [MPa]	cn	φ_c [°]	α	β	e_{i0}	e_{c0}	c [s]	κ
1.0	0.0	1.0	1.0	1.0	0.0	190.0	/	0.4	30.0	0.7	1.0	1.3	0.7	/	/

Initial values

e_0	σ_{11} [MPa]	σ_{22} [MPa]	σ_{33} [MPa]	σ_{max} [MPa]
0.3	−0.1	−0.1	−0.1	−4.0e6

Numeric parameters

$\dot{\varepsilon}_{11}$	$\dot{\varepsilon}_{22}$	$\dot{\varepsilon}_{33}$	Δt	n
−0.01	−0.0001	−0.0001	0.008	3000.0

4 Results

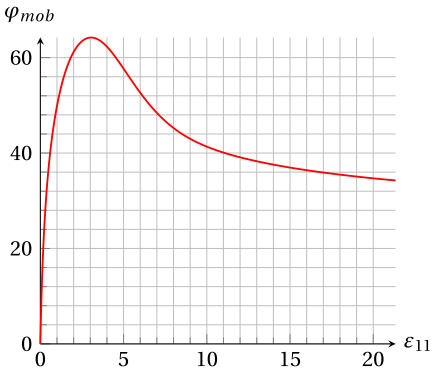

Fig. 1: φ_{mob} vs ε_{11}

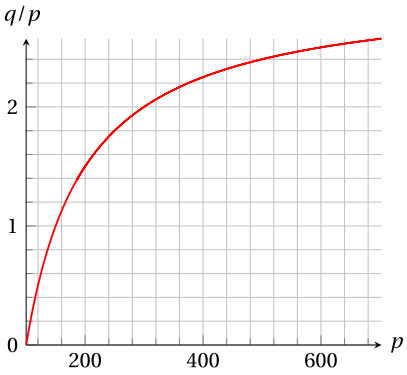

Fig. 2: q/p vs p

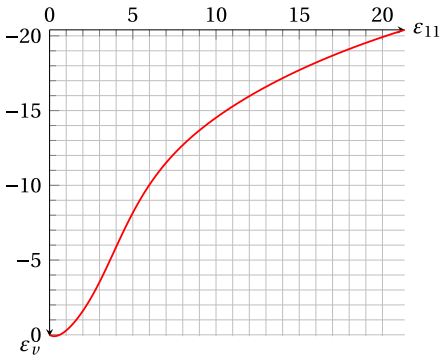

Fig. 3: ε_v vs ε_{11}

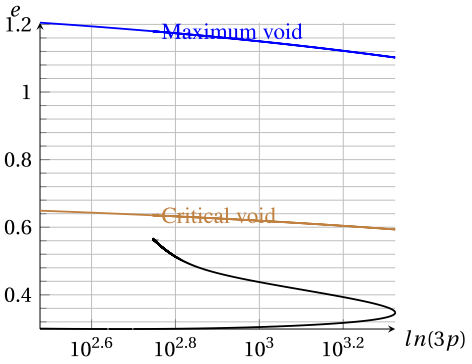

Fig. 4: e vs $ln(3p)$

Please note that for simplicity, the unit of stress in the results section is set as kPa, strain is in unit [%]. Stress and strain are in conventional soil mechanics form: positive for compression, negative for extension and strain is in engineering strain form.

5 Appendix

- **sign convention**:
  Please note that in *hypoplasticity*, the *compression* stress and strain are considered as *negative* terms. Here the strain is in *logarithmic strain* form. While in order to avoid confusion, the numerical simulation results are represented in the conventional soil mechanics form: compression as "*positive*", extension as "*negative*" and strain is in *engineering strain* form.
- relation between **logarithmic strain** and **engineering strain**:

$$\varepsilon_v^N = \ln(1+\varepsilon_v)$$

  with ε_v^N represents the logarithmic strain and ε_v stands for the engineering strain. While here the preceding strains are considered negative for compression.
- The files and relative directories are tabulated as follow:

Files	**Directory**
Input files:	
triaxi_con_inp.txt	C:\Users\student\Desktop\HET_v005\hypo_v005\MAT\triaxi
triaxi_inp_inp.txt	C:\Users\student\Desktop\HET_v005\hypo_v005\MAT\triaxi
triaxi_num_inp.txt	C:\Users\student\Desktop\HET_v005\hypo_v005\MAT\triaxi
Calculation file:	
het_v005_triaxi.exe	C:\Users\student\Desktop\HET_v005\hypo_v005\MAT\triaxi
Python script:	
het_main_v4.py	C:\Users\student\Desktop\HET_v005\hypo_v005\PYT
Result:	
hypo_v005_triaxi_all_17Dec181153.dat	C:\Users\student\Desktop\HET_v005\hypo_v005\calculations\ovalle18\v005ovalle

A.3.3 Source code of HET for triaxial compression test

```
%*****************************************************%
%--Subroutine name: het_v005_triaxi_sub ----------------***%
%--Programer:      Linke Li ----------------------------***%
%--Version:        16/01/2018--------------------------***%
%*****************************************************%
%--Description: This subroutine is desgined for       ***%
%  simulating triaxial compression with boundary      ***%
%  conditions:                                        ***%
%  ---------------------------------                  ***%
%  dot_sigma(2,2)=dot_sigma(3,3)=0                    ***%
%  ---------------------------------                  ***%
%  The known initial values are as follow:            ***%
%  sigma(1,1), sigma(2,2), sigma(3,3), dot_eps(1,1)   ***%
%  in the matrix form is:                             ***%
%  ---------------------------                        ***%
%  T(1,1),T(2,2),T(3,3),D(1,1) is known.              ***%
%  ---------------------------                        ***%
%  True triaxial compression is taken into account.   ***%
%  The degradation of hs is considered as two parts,  ***%
%  in particular, the mean pressure and the deviatoric***%
%   stress with the equation as following:            ***%
%  ---------------------------------------------      ***%
%  hsdot = -c6*(trTdot/trT)*(-trT/bp)^(np)*hs ...     ***%
%          -c7*bsd*(|Tdev_dot|*|Tdev|/trT^2)*hs;      ***%
%  ---------------------------------------------      ***%
%  Please note the c6 and c7 are swith on/off factor, ***%
%  which is only set as 1.0 or 0.0 for parameter study.**%
%*****************************************************%
%--Description:                                       ***%
%(1)Newton iteration method is used for calculating   ***%
%   d22,d33.                                          ***%
%(2)The analytical solution of stress rate is written ***%
%   explicitly. The analytical solution should be     ***%
%   updated if any modification of the constitutive   ***%
%   equations was made.                               ***%
%*****************************************************%
%--Updates:                                           ***%
%  --by L. Li, 27.04.2018                             ***%
% 1) Develop fuctions <DevMat_3(M)>, <EuNoMat_3(M)>   ***%
%    for calculate deviatoric part and the Euclidean  ***%
```

```
41 %     norm of a given matrix M.                                    ***%
42 %*****************************************************************%
43 function [Tdot,Dt,de,hsdot,a_hat,f_d,f_s] =
       het_v005_triaxi_sub(T,Dt,...
44     hs,cn,phi_c,et,e_i0,e_c0,alpha,beta,c1,c2,c3,c4,c5,c6,
         c7,bp,np,bsd)
45 phic_rad = deg2rad(phi_c);
46 sin_phic = sin(phic_rad);
47 trT = TracMatr(T);
48 p = -1/3*trT;
49 Tn_star = DeviNormMatr_3(T);
50 Tn = NormMatr_3(T);
51 %trDt = TracMatr(Dt);
52 e_i = e_i0*exp(-(-trT/hs)^cn);
53 e_c = e_c0*exp(-(-trT/hs)^cn);
54 %calculate Tn_star(kl)*Tn_star(kl):
55 s_ij_2 = m_ij_2(Tn_star);
56 %calculate Tn_star(kl)*Tn_star(lm)*Tn_star(mk):
57 s_ij_3 = m_ij_3(Tn_star);
58 %Calculate a_hat:
59 %   For the case of isotropic stress state, the g_hat %
60 %  (or cos(3*theta)) will become zero, then it should %
61 %  be manually set to equal one.                        %
62 if s_ij_2==0
63     g_ahat = 1;
64 else
65     g_ahat = -sqrt(6)*s_ij_3/(s_ij_2)^(3/2);
66 end
67 a_hat = sin_phic/(3-sin_phic)*(sqrt((8/3-3*s_ij_2+g_ahat*
       sqrt(3/2)*...
68     s_ij_2^(3/2))/(1+g_ahat*sqrt(3/2)*sqrt(s_ij_2)))-sqrt(
         s_ij_2));
69 %calculate f_e:
70 f_e = (e_c/et)^beta;
71 %calculate f_b:
72 a_hat_i = sqrt(8/3)*(sin_phic/(3-sin_phic));
73 %calculate h_i:
74 h_i = 3*c1*a_hat_i^2 + 9*c2 + c3 - c4*a_hat_i*sqrt(3)*(e_i/
       e_c)^alpha;
75 %calculate f_b:
76 f_b = (1 + e_i)/(e_i)*(hs^(cn))/(cn*h_i)*(3*p)^(1-cn)/(1+c6
       *(3*p/bp)^np)...
```

```
77      *(e_i/e_c)^(beta);
78  %calculate f_s:
79  s_hat_ij_2 = m_ij_2(Tn);
80  f_s_star = 1/(s_hat_ij_2);
81  f_s = f_e*f_s_star*f_b;
82  %calculate f_d:
83  f_d = (et/e_c)^alpha;
84  %Start the Newton-Iteration method for solving
85  % dot_sig(2,2)=dot_sig(3,3)=0%
86  x = [Dt(2,2); Dt(3,3)];
87  y = zeros(2,1);
88  dy = zeros(2,2);
89  %specify the dot_sig(2,2) as y(1):
90  y(1) = f_s*(c1*a_hat^2*x(1)+c2*(Dt(1,1)+x(1)+x(2))+...
91      c3*(Tn(1,1)*Dt(1,1)+Tn(2,2)*x(1)+Tn(3,3)*x(2))*Tn(2,2)
            +...
92      c4*f_d*a_hat*(Tn(2,2)+c5*(Tn(2,2)-1/3))*...
93      sqrt(Dt(1,1)^2+x(1)^2+x(2)^2));
94  %specify the dot_sig(3,3) as y(2):
95  y(2) = f_s*(c1*a_hat^2*x(2)+c2*(Dt(1,1)+x(1)+x(2))+...
96      c3*(Tn(1,1)*Dt(1,1)+Tn(2,2)*x(1)+Tn(3,3)*x(2))*Tn(3,3)
            +...
97      c4*f_d*a_hat*(Tn(3,3)+c5*(Tn(3,3)-1/3))*...
98      sqrt(Dt(1,1)^2+x(1)^2+x(2)^2));
99  %
100 dy(1,1) = f_s*(c1*a_hat^2+c2+c3*Tn(2,2)*Tn(2,2)+...
101     c4*f_d*a_hat*(Tn(2,2)+c5*(Tn(2,2)-1/3))*x(1)*...
102     power((Dt(1,1)^2+x(1)^2+x(2)^2),(-1/2)));
103 dy(1,2) = f_s*(c2+c3*Tn(3,3)*Tn(2,2)+...
104     c4*f_d*a_hat*(Tn(2,2)+c5*(Tn(2,2)-1/3))*x(2)*...
105     power((Dt(1,1)^2+x(1)^2+x(2)^2),(-1/2)));
106 %
107 dy(2,1) = f_s*(c2+c3*Tn(2,2)*Tn(3,3)+...
108     c4*f_d*a_hat*(Tn(3,3)+c5*(Tn(3,3)-1/3))*x(1)*...
109     power((Dt(1,1)^2+x(1)^2+x(2)^2),(-1/2)));
110 dy(2,2) = f_s*(c1*a_hat^2+c2+c3*Tn(3,3)*Tn(3,3)+...
111     c4*f_d*a_hat*(Tn(3,3)+c5*(Tn(3,3)-1/3))*x(2)*...
112     power((Dt(1,1)^2+x(1)^2+x(2)^2),(-1/2)));
113 %
114 NumIters = 1;
115 eps = 1;
116 while eps>1e-10 && NumIters<1000
```

```
117     % calculate strain rate increments
118     Dd = dy\y;
119     % update strain rate
120     x  = x - Dd;
121     % update functions
122     y(1) = f_s*(c1*a_hat^2*x(1)+c2*(Dt(1,1)+x(1)+x(2))+...
123          c3*(Tn(1,1)*Dt(1,1)+Tn(2,2)*x(1)+Tn(3,3)*x(2))*Tn
                (2,2)+...
124          c4*f_d*a_hat*(Tn(2,2)+c5*(Tn(2,2)-1/3))*...
125          sqrt(Dt(1,1)^2+x(1)^2+x(2)^2));
126     y(2) = f_s*(c1*a_hat^2*x(2)+c2*(Dt(1,1)+x(1)+x(2))+...
127          c3*(Tn(1,1)*Dt(1,1)+Tn(2,2)*x(1)+Tn(3,3)*x(2))*Tn
                (3,3)+...
128          c4*f_d*a_hat*(Tn(3,3)+c5*(Tn(3,3)-1/3))*...
129          sqrt(Dt(1,1)^2+x(1)^2+x(2)^2));
130     dy(1,1) = f_s*(c1*a_hat^2+c2+c3*Tn(2,2)*Tn(2,2)+...
131          c4*f_d*a_hat*(Tn(2,2)+c5*(Tn(2,2)-1/3))*x(1)*...
132          power((Dt(1,1)^2+x(1)^2+x(2)^2),(-1/2)));
133     dy(1,2) = f_s*(c2+c3*Tn(3,3)*Tn(2,2)+...
134          c4*f_d*a_hat*(Tn(2,2)+c5*(Tn(2,2)-1/3))*x(2)*...
135          power((Dt(1,1)^2+x(1)^2+x(2)^2),(-1/2)));
136     dy(2,1) = f_s*(c2+c3*Tn(2,2)*Tn(3,3)+...
137          c4*f_d*a_hat*(Tn(3,3)+c5*(Tn(3,3)-1/3))*x(1)*...
138          power((Dt(1,1)^2+x(1)^2+x(2)^2),(-1/2)));
139     dy(2,2) = f_s*(c1*a_hat^2+c2+c3*Tn(3,3)*Tn(3,3)+...
140          c4*f_d*a_hat*(Tn(3,3)+c5*(Tn(3,3)-1/3))*x(2)*...
141          power((Dt(1,1)^2+x(1)^2+x(2)^2),(-1/2)));
142     % update total error
143     eps=abs(y(1))+abs(y(2));                %error
144     % update iteration step
145     NumIters=NumIters+1;
146 end
147 Dt(2,2) = x(1);
148 Dt(3,3) = x(2);
149 trDt = TracMatr(Dt);
150 %calculate Tdot matric:
151 Tdot = zeros(3,3);
152 Tdot(1,1) = f_s*(c1*a_hat^2*Dt(1,1)+c2*(Dt(1,1)+Dt(2,2)+Dt
        (3,3))+...
153      c3*(Tn(1,1)*Dt(1,1)+Tn(2,2)*Dt(2,2)+Tn(3,3)*Dt(3,3))*Tn
            (1,1)+...
154      c4*f_d*a_hat*(Tn(1,1)+c5*(Tn(1,1)-1/3))*...
```

```
155       sqrt(Dt(1,1)^2+Dt(2,2)^2+Dt(3,3)^2));
156 Tdot(2,2) = f_s*(c1*a_hat^2*Dt(2,2)+c2*(Dt(1,1)+Dt(2,2)+Dt
      (3,3))+...
157       c3*(Tn(1,1)*Dt(1,1)+Tn(2,2)*Dt(2,2)+Tn(3,3)*Dt(3,3))*Tn
            (2,2)+...
158       c4*f_d*a_hat*(Tn(2,2)+c5*(Tn(2,2)-1/3))*...
159       sqrt(Dt(1,1)^2+Dt(2,2)^2+Dt(3,3)^2));
160 Tdot(3,3) = f_s*(c1*a_hat^2*Dt(3,3)+c2*(Dt(1,1)+Dt(2,2)+Dt
      (3,3))+...
161       c3*(Tn(1,1)*Dt(1,1)+Tn(2,2)*Dt(2,2)+Tn(3,3)*Dt(3,3))*Tn
            (3,3)+...
162       c4*f_d*a_hat*(Tn(3,3)+c5*(Tn(3,3)-1/3))*...
163       sqrt(Dt(1,1)^2+Dt(2,2)^2+Dt(3,3)^2));
164 %calculate rate of void ratio:
165 de = (1+et)*trDt;
166 %calculate the rate of hs:
167 trTdot = TracMatr(Tdot);
168 Tdev_dot = DevMat_3(Tdot);
169 Tdev = DevMat_3(T);
170 NormTdev_dot = EuNoMat_3(Tdev_dot);
171 NormTdev = EuNoMat_3(Tdev);
172 hsdot = -c6*(trTdot/trT)*(-trT/bp)^(np)*hs ...
173           - c7*bsd*(NormTdev_dot*NormTdev/trT^2)*hs;
```

A.4 Parameter $\hat{a}_o$ for oedometric tests

As it is defined according to the Eq. (2.20), the function $\hat{a}$ which related to limitation condition is repeated here:

$$\hat{a} = \frac{\sin\varphi_c}{3-\sin\varphi_c}\left\{\sqrt{\frac{8/3-3\|\hat{\mathbf{T}}^*\|^2+\sqrt{3/2}\|\hat{\mathbf{T}}^*\|^3\cos 3\theta}{1+\sqrt{3/2}\|\hat{\mathbf{T}}^*\|\cos 3\theta}}-\|\hat{\mathbf{T}}^*\|\right\} \tag{A.8}$$

with

$$\|\hat{\mathbf{T}}^*\| = \left\{\mathrm{tr}\left(\hat{\mathbf{T}}^{*2}\right)\right\}^{1/2} \tag{A.9}$$

and $\cos 3\theta$, a quantity related to Lode angle with the definition:

$$\cos 3\theta = -\frac{\sqrt{6}\,\mathrm{tr}\left(\hat{\mathbf{T}}^{*3}\right)}{\left\{\mathrm{tr}\left(\hat{\mathbf{T}}^{*2}\right)\right\}^{3/2}} \tag{A.10}$$

Take a axisymmetric oedoemtric condition as an example, considering $T_{22} = T_{33} = KT_{11}$, the normalized stress tensor and the deviator can be written in the matrix representation

$$\left[\hat{\mathbf{T}}\right] = \frac{1}{1+2K}\begin{bmatrix}1 & 0 & 0\\ 0 & K & 0\\ 0 & 0 & K\end{bmatrix} \tag{A.11}$$

and

$$\left[\hat{\mathbf{T}}^*\right] = \frac{1-K}{3(1+2K)}\begin{bmatrix}2 & 0 & 0\\ 0 & -1 & 0\\ 0 & 0 & -1\end{bmatrix} \tag{A.12}$$

respectively.

Thus, the Euclidian norm of stress deviator tensor is:

$$\|\hat{\mathbf{T}}^*\| = \sqrt{\mathrm{tr}\left(\hat{\mathbf{T}}^{*2}\right)} = \sqrt{\hat{\mathrm{T}}_{ij}\hat{\mathrm{T}}_{ij}} \tag{A.13}$$

In particular, $\|\hat{\mathbf{T}}^*\|$ is

$$\|\hat{\mathbf{T}}^*\| = \sqrt{\frac{4(1-K)^2}{9(1+2K)^2}+\frac{2(1-K)^2}{9(1+2K)^2}} = \sqrt{\frac{2}{3}}\frac{1-K}{1+2K} \tag{A.14}$$

and

$$\|\hat{\mathbf{T}}^*\|^2 = \frac{2}{3}\left(\frac{1-K}{1+2K}\right)^2 \tag{A.15}$$

$$\|\hat{\mathbf{T}}^*\|^3 = \sqrt{\frac{8}{27}}\left(\frac{1-K}{1+2K}\right)^3 \tag{A.16}$$

For the $\cos 3\theta$:

$$\cos 3\theta = -\sqrt{6}\frac{\mathrm{tr}\left(\hat{\mathbf{T}}^{*3}\right)}{\left\{\mathrm{tr}\left(\hat{\mathbf{T}}^{*2}\right)\right\}^{3/2}} = -\sqrt{6}\frac{\dfrac{6\left(1-K\right)^3}{27\left(1+2K\right)^3}}{\sqrt{\dfrac{8}{27}}\dfrac{\left(1-K\right)^3}{\left(1+2K\right)^3}} = -1 \tag{A.17}$$

Set $A = 8/3 - 3\|\hat{\mathbf{T}}^*\|^2 + \sqrt{3/2}\|\hat{\mathbf{T}}^*\|^3\cos 3\theta$, then A can be derived based on the aforementioned equations:

$$\begin{aligned} A &= \frac{8}{3} - 3\times\frac{2}{3}\left(\frac{1-K}{1+2K}\right)^2 + \sqrt{\frac{3}{2}}\times\sqrt{\frac{8}{27}}\left(\frac{1-K}{1+2K}\right)^3\times(-1) \\ &= \frac{8}{3} - 2\left(\frac{1-K}{1+2K}\right)^2 - \frac{2}{3}\left(\frac{1-K}{1+2K}\right)^3 \end{aligned}$$

Substitute $B = (1-K)/(1+2K)$ into A:

$$\begin{aligned} A &= \frac{2}{3}\left(4 - 3B^2 - B^3\right) \\ &= \frac{2}{3}\left(4 - 4B + 4B - 4B^2 + B^2 - B^3\right) \\ &= \frac{2}{3}\left\{4\left(1-B\right) + 4B\left(1-B\right) + B^2\left(1-B\right)\right\} \\ &= \frac{2}{3}\left(1-B\right)\left(4 + 4B + B^2\right) \\ &= \frac{2}{3}\left(1-B\right)\left(2+B\right)^2 \end{aligned}$$

Set $C = 1 + \sqrt{3/2}\|\hat{\mathbf{T}}^*\|\cos 3\theta$, then C can be represented as:

$$\begin{aligned} C &= 1 + \sqrt{\frac{3}{2}}\times\sqrt{\frac{2}{3}}B\times(-1) \\ &= 1 - B \end{aligned}$$

Thus, the $\hat{a}_o$ can be written as:

$$\begin{aligned} \hat{a}_o &= \frac{\sin\varphi_c}{3-\sin\varphi_c}\left\{\sqrt{\frac{2}{3}\frac{\left(1-B\right)\left(2+B\right)^2}{\left(1-B\right)}} - \sqrt{\frac{2}{3}}B\right\} \\ &= \frac{\sin\varphi_c}{3-\sin\varphi_c}\left\{\sqrt{\frac{2}{3}}\left(2+B\right) - \sqrt{\frac{2}{3}}B\right\} \\ &= \sqrt{\frac{8}{3}}\frac{\sin\varphi_c}{3-\sin\varphi_c} \end{aligned}$$

For the isotropic compression, $\|\hat{\mathbf{T}}^*\| = 0$ and $\cos 3\theta = -1$ can lead the $\hat{a}$ to end up with the same result of $\hat{a}$ for oedometer compression: $\hat{a}_i = \hat{a}_o = \sqrt{8/3}\sin\varphi_c/(3-\sin\varphi_c)$, with subscript "$i$" represents isotropic compression and the one "o" stands for oedometer compression.

A.5 Summary of experimental tests used

Table A.1: XRD results of a sample finer than 0.08 mm (I) from Ovalle et al. [74]

Components	Quartz	Albite	Sodium aluminium silicate
Chemical formula	SiO_2	$NaAlSi_3O_8$	$Na_6Al_6Si_{10}O_{32}$
Percentage	64	26	10

Table A.2: XRD results of a sample finer than 0.08 mm (II) from Ovalle [73]

Chemical element	O	Si	Al	Fe	K	Na	Mg	S	Ti
Percentage of mass	48.6	24.6	10.9	8.4	3.8	2.0	1.2	0.4	0.2

Table A.3: Summary of isotropic compression tests

Test No.	Initial state		$T_{22,max}$ [MPa]	Test conditions
	void ratio	$T_{22,0}$ [MPa]		
D1	0.955	-0.236	-0.8	Dry
W2	0.967	-0.224	-0.8	Dry, 1 h creep at $T_{22,max}$, saturated

Table A.4: Summary of oedometric compression tests

Test No.	Initial state		$T_{v,max}$ [MPa]	Test conditions
	void ratio	T_v [kPa]		
D3	1.066	-4.617	-0.4	Dry
D4	1.015	-4.606	-0.6	Dry
D5	0.995	-4.584	-0.85	Dry
D6	1.014	-4.592	-2.1	Dry
D7	0.990	-4.624	-2.1	Dry
S8	1.035	-4.628	-0.4	Saturated/Initially wetted
S9	1.029	-4.628	-0.85	Saturated
S10	1.051	-4.615	-2.1	Saturated
W11	1.008	-4.606	-2.1	Wetted at $T_v = 0.4$ MPa
W12	1.009	-4.618	-0.4	Wetted at $T_v = 0.4$ MPa
W13	1.000	-4.611	-0.85	Wetted at $T_v = 0.85$ MPa
W14	1.003	-4.610	-2.1	Wetted at $T_v = 1.5$ MPa

Table A.5: Summary of triaxial compression tests

Test No.	Initial state		T_{22} [MPa]	Test conditions
	void ratio	$T_{22,0}$ [kPa]		
D15	0.933	-236	-0.8	Dry
W16	0.929	-12	-0.8	Dry, wetted after isotropic consolidation
W17	0.935	-30	-0.8	Dry, wetted after isotropic consolidation
W18	0.945	-10	-0.8	Dry, wetted at $\varepsilon_{11} = 12\%$
W19	0.903	-10	-0.8	Dry, wetted at $\varepsilon_{11} = 10\%$
W20	0.948	-22	-0.8	Dry, wetted at $\varepsilon_{11} = 8\%$
D21	0.949	-13	-0.4	Dry
W22	0.957	-9	-0.4	Dry, wetted at $\varepsilon_{11} = 7\%$

A.6 Input data for parameter study

Table A.6: Parameter set for analysis of the model performance

Variable	Constitutive parameters						Initial state			
	φ_c [°]	h_{sd} [MPa]	n [-]	e_{i0} [-]	e_{c0} [-]	α [-]	T_{11} [MPa]	T_{22} [MPa]	T_{33} [MPa]	e_0 [-]
φ_c	**35**	22.4	0.64	1.2	0.9	0.5	-0.1	-0.1	-0.1	0.6 / 1.0
	37	22.4	0.64	1.2	0.9	0.5	-0.1	-0.1	-0.1	0.6 / 1.0
	40	22.4	0.64	1.2	0.9	0.5	-0.1	-0.1	-0.1	0.6 / 1.0
	42	22.4	0.64	1.2	0.9	0.5	-0.1	-0.1	-0.1	0.6 / 1.0
h_s	37	**15**	0.64	1.2	0.9	0.5	-0.1	-0.1	-0.1	0.6 / 1.0
	37	**18**	0.64	1.2	0.9	0.5	-0.1	-0.1	-0.1	0.6 / 1.0
	37	**22.4**	0.64	1.2	0.9	0.5	-0.1	-0.1	-0.1	0.6 / 1.0
	37	**25**	0.64	1.2	0.9	0.5	-0.1	-0.1	-0.1	0.6 / 1.0
n	37	22.4	**0.4**	1.2	0.9	0.5	-0.1	-0.1	-0.1	0.6 / 1.0
	37	22.4	**0.5**	1.2	0.9	0.5	-0.1	-0.1	-0.1	0.6 / 1.0
	37	22.4	**0.64**	1.2	0.9	0.5	-0.1	-0.1	-0.1	0.6 / 1.0
	37	22.4	**0.7**	1.2	0.9	0.5	-0.1	-0.1	-0.1	0.6 / 1.0
e_{i0}	37	22.4	0.64	**1.1**	0.9	0.5	-0.1	-0.1	-0.1	0.6 / 1.0
	37	22.4	0.64	**1.2**	0.9	0.5	-0.1	-0.1	-0.1	0.6 / 1.0
	37	22.4	0.64	**1.3**	0.9	0.5	-0.1	-0.1	-0.1	0.6 / 1.0
	37	22.4	0.64	**1.4**	0.9	0.5	-0.1	-0.1	-0.1	0.6 / 1.0
e_{c0}	37	22.4	0.64	1.2	**0.7**	0.5	-0.1	-0.1	-0.1	0.6 / 1.0
	37	22.4	0.64	1.2	**0.8**	0.5	-0.1	-0.1	-0.1	0.6 / 1.0
	37	22.4	0.64	1.2	**0.9**	0.5	-0.1	-0.1	-0.1	0.6 / 1.0
	37	22.4	0.64	1.2	**1.0**	0.5	-0.1	-0.1	-0.1	0.6 / 1.0
α	37	22.4	0.64	1.2	0.9	**0.1**	-0.1	-0.1	-0.1	0.6 / 1.0
	37	22.4	0.64	1.2	0.9	**0.3**	-0.1	-0.1	-0.1	0.6 / 1.0
	37	22.4	0.64	1.2	0.9	**0.5**	-0.1	-0.1	-0.1	0.6 / 1.0
	37	22.4	0.64	1.2	0.9	**0.7**	-0.1	-0.1	-0.1	0.6 / 1.0

List of Figures

List of Tables

References

[1] E. E. Alonso and R. Cardoso. Behaviour of materials for earth and rockfill dams: Perspective from unsaturated soil mechanics. In E. Bauer, S. Semprich, and G. Zenz, editors, *Long term behaviour of dams: Proceedings of the 2nd international conference*, pages 1–38, Graz, 2009. Graz University of Technology.

[2] E. E. Alonso and R. Cardoso. Behavior of materials for earth and rockfill dams: Perspective from unsaturated soil mechanics. *Frontiers of Architecture and Civil Engineering in China*, 4(1):1–39, 2010. doi: 10.1007/s11709-010-0013-6.

[3] E. E. Alonso, A. Gens, and A. Josa. A constitutive model for partially saturated soils. *Géotechnique*, 40(3):405–430, 1990. doi: 10.1680/geot.1990.40.3.405.

[4] F. N. Altuhafi and M. R. Coop. Changes to particle characteristics associated with the compression of sands. *Géotechnique*, 61(6):459–471, 2011. doi: 10.1680/geot.9.P.114.

[5] K. E. Anaraki. Hypoplasticity investigated: parameter determination and numerical simulation. Master thesis, Delft University of Technology, 2008.

[6] E. Bauer. Calibration of a comprehensive hypoplastic model for granular materials. *Soils and Foundations*, 36(1):13–26, 1996. doi: 10.3208/sandf.36.13.

[7] E. Bauer. Conditions for embedding Casagrande's critical states into hypoplasticity. *Mechanics of Cohesive-frictional Materials*, 5(2):125–148, 2000. doi: 10.1002/(SICI)1099-1484(200002)5:2<125::AID-CFM85>3.0.CO;2-0.

[8] E. Bauer. Hypoplastic modelling of moisture-sensitive weathered rockfill materials. *Acta Geotechnica*, 4(4):261, 2009. doi: 10.1007/s11440-009-0099-y.

[9] E. Bauer. *Introduction to tensor analysis*. Institute of Applied Mechanics, Graz University of Technology, Graz, 2014.

[10] E. Bauer. *Simulation of the influence of grain damage on the evolution of shear strain localization*, pages 231–244. Springer International Publishing, Cham, 2016. ISBN 978-3-319-28241-1. doi: 10.1007/978-3-319-28241-1_16.

[11] E. Bauer, Z. Z. Fu, and S. H. Liu. Influence of pressure and density on the rheological properties of rockfills. *Frontiers of Structural and Civil Engineering*, 6(1):25–34, 2012. doi: 10.1007/s11709-012-0143-0.

[12] E. Bauer, L. K. Li, and M. Khosravi. Modelling grain damage under plane strain compression using a micro-polar continuum. In E. Papamichos, P. Papanastasiou, E. Pasternak, and A. Dyskin, editors, *Bifurcation and Degradation of Geomaterials with Engineering Applications*, pages 539–546, Cham, 2017. Springer International Publishing. ISBN 978-3-319-56397-8. doi: 10.1007/978-3-319-56397-8_67.

[13] E. Bauer, S. Safikhani, and L. K. Li. Numerical simulation of the effect of grain fragmentation on the evolution of microstructure quantities. *Meccanica*, 2018. Reviewing.

[14] K. Been, M. G. Jefferies, and J. Hachey. The critical state of sands. *Géotechnique*, 41(3):365–381, 1991. doi: 10.1680/geot.1991.41.3.365.

[15] R. Butterfield. A natural compression law for soils (an advance on $e - \log p'$). *Géotechnique'*, 29(4):469–480, 1979. doi: 10.1680/geot.1979.29.4.469.

[16] J. P. Carter, W. S. Kaggwa, I. W. Johnston, E. A. Novello, M. Fahey, and G. A. Chapman. Triaxial testing of North Rankin calcarenite. In Jewell & Khorshid, editor, *Engineering fro Calcareous Sediments*, volume 1, pages 515–530, Perth, 1988.

[17] N. C. Consoli, M. D. Casagrande, and M. R. Coop. Effect of fiber reinforcement on the isotropic compression behavior of a sand. *Journal of Geotechnical and Geoenvironmental Engineering*, 131(11):1434–1436, 2005. doi: 10.1061/(ASCE) 1090-0241(2005)131:11(1434).

[18] M. R. Coop. The mechanics of uncemented carbonate sands. *Géotechnique*, 40(4): 607–626, 1990. doi: 10.1680/geot.1990.40.4.607.

[19] M. R. Coop and J. H. Atkinson. The mechanics of cemented carbonate sands. *Géotechnique*, 43(1):53–67, 1993. doi: 10.1680/geot.1993.43.1.53.

[20] Z. Z. Fu, S. S. Chen, and S. H. Liu. Hypoplastic constitutive modelling of the wetting induced creep of rockfill materials. *Science China Technological Sciences*, 55(7):2066–2082, 2012. doi: 10.1007/s11431-012-4835-4.

[21] M. Goldscheider. Grenzbedingung und Fließregel von Sand. *Mechanics Research Communications*, 3:463–468, 1967.

[22] G. Gudehus. A comprehensive constitutive equation for granular materials. *Soils and Foundations*, 36(1):1–12, 1996. doi: 10.3208/sandf.36.1.

[23] G. Gudehus and D. Mašín. Graphical representation of constitutive equations. *Géotechnique*, 59(2):147–151, 2009. doi: 10.1680/geot.2007.00155.

[24] G. Gudehus, M. Goldscheider, and H. Winter. *Mechanical properties of sand and clay and numerical integration methods: some sources of errors and bounds of accuracy*, chapter 3, pages 121–150. Finite elements in geomechanics. Wiley, 1977.

[25] X. G. Guo, C. Peng, W. Wu, and Y. Q. Wang. A hypoplastic constitutive model for debris materials. *Acta Geotechnica*, 11(6):1217–1229, 2016. doi: 10.1007/s11440-016-0494-0.

[26] I. Herle. *Hypoplastizität und Granulometrie einfacher KorngerÃijste*. Phd thesis, Institut für Bodenmechanik und Felsmechanik der Universität Fridericiana in Karlsruhe, Karlsruhe, 1997.

[27] I. Herle and G. Gudehus. Determination of parameters of a hypoplastic constitutive model from properties of grain assemblies. *Mechanics of Cohesive-frictional Materials*, 4(5):461–486, 1999. doi: 10.1002/(SICI)1099-1484(199909)4:5<461::AID-CFM71>3.0.CO;2-P.

[28] I. Herle and D. Kolymbas. Hypoplasticity for soils with low friction angles. *Computers and Geotechnics*, 31(5):365–373, 2004. ISSN 0266-352X. doi: https://doi.org/10.1016/j.compgeo.2004.04.002.

[29] K. Holestöl, B. Kjaernsli, and I. Torblaa. Compression of tunnel spoil at Venemo Dam. 2:490–494, 1965.

[30] G. W. Howson. On design of rockfill dams. *Transactions of the American Society of Civil Engineers*, 104:42, 1939.

[31] W. X. Huang. *Hypoplastic modelling of shear localisation in granular materials*. Phd thesis, Technische Universität Graz, Graz, 2000.

[32] W. X. Huang, K. Nübel, and E. Bauer. Polar extension of a hypoplastic model for granular materials with shear localization. *Mechanics of Materials*, 34(9):563–576, 2002. doi: https://doi.org/10.1016/S0167-6636(02)00163-1.

[33] K. Ishihara. Liquefaction and flow failure during earthquakes. *Géotechnique*, 43 (3):351–451, 1993. doi: 10.1680/geot.1993.43.3.351.

[34] J. E. B. Jennings. Discussion. In *Proceedings of 3rd Asian Regional Confecence on Soil Mechanics and Foundation Engineering*, volume 2, pages 102–104, Haifa, 1967.

[35] J. E. B. Jennings and J. B. Burland. Limitations to the use of effective stresses in partly saturated soils. *Géotechnique*, 12(2):125–144, 1962. doi: 10.1680/geot.1962.12.2.125.

[36] H. Karimpour and P. V. Lade. Time effects relate to crushing in sand. *Journal of Geotechnical and Geoenvironmental Engineering*, 136(9):1209–1219, 2010. doi: 10.1061/(ASCE)GT.1943-5606.0000335.

[37] H. Karimpour and P. V. Lade. Creep behavior in Virginia Beach sand. *Canadian Geotechnical Journal*, 50(11):1159–1178, 2013. doi: 10.1139/cgj-2012-0467.

[38] K. Kast. *Mechanisches Verhalten von Granitschüttungen*. Phd thesis, Institut für Bodenmechanik und Felsmechanik der Universität Fridericiana in Karlsruhe, Karlsruhe, 1992.

[39] K. Kast, A. Blinde, and J. Brauns. Verdichtungs-, Verformungs- und Sättigungsverhalten von Schüttungen in Abhängigkeit von der geologischen Gesteinsentfestigung. In K. H. Heitfeld, editor, *Ingenieurgeologische Probleme im Grenzbereich zwischen Locker- und Festgesteinen*, pages 237–254. Springer-Verlag Berlin Heidelberg, 1985. ISBN 978-3-642-70452-9. doi: 10.1007/978-3-642-70452-9.

[40] D. Kolymbas. A rate-dependent constitutive equation for soils. *Mechanics Research Communications*, 4(6):367–372, 1977.

[41] D. Kolymbas. A generalized hypoelastic constitutive law. In Publications Committee of XI ICSMFE, editor, *Proceeding of the Eleventh International Conference on Soil Mechanics and Foundation Engineering*, volume 5, page 2626, San Francisco, 1985. A.A. Balkema.

[42] D. Kolymbas. *Eine konstitutive Theorie für Böden und andere Körnige Stoffe*. Habilitation thesis, Veröffentlichungen des Institutes für Bodenmechanik und Felsmechanik der Universität Fridericiana in Karlsruhe, 1988.

[43] D. Kolymbas. An outline of hypoplasticity. *Archive of Applied Mechanics*, 61(3): 143–151, 1991.

[44] D. Kolymbas. *Introduction to Hypoplasticity*. Number 1 in Advances in Geotechnical engineering and tunnelling. A. A. Balkema, Rotterdam, 2000.

[45] D. Kolymbas. Sand as an archetypical natural solid. In D. Kolymbas and G. Viggiani, editors, *Mechanics of Natural Solids*, volume 1, pages 1–26, Horton, 2009. Springer-Verlag Berlin Heidelberg.

[46] D. Kolymbas. Barodesy: a new hypoplastic approach. *International Journal for Numerical and Analytical Methods in Geomechanics*, 36(9):1220–1240, 2012. doi: 10.1002/nag.1051.

[47] D. Kolymbas and E. Bauer. Soft oedometer– a new testing device and its application for the calibration of hypoplastic constitutive laws. *Geotechnical Testing Journal*, 16(2):263–270, 1993. ISSN 0149-6115. doi: 10.1520/GTJ10044J.

[48] D. Kolymbas and G. Medicus. Genealogy of hypoplasticity and barodesy. *International Journal for Numerical and Analytical Methods in Geomechanics*, 40(18): 2532–2550, 2016. doi: 10.1002/nag.2546.

[49] P. V. Lade. *Experimental study and analysis of creep and stress relaxation in granular materials*. doi: 10.1061/40917(236)15.

[50] P. V. Lade and P. A. Bopp. Relative density effects on drained sand behavior at high pressures. *Soils and Foundations*, 45(1):1–13, 2005.

[51] K. J. Laidler. *Chemical kinetics*. HarperCollins, 3rd edition, 1987. ISBN 8131709728.

[52] Imre Laufer. Grain crushing and high-pressure oedometer tests simulated with the discrete element method. *Granular Matter*, 17(3):389–412, 2015. ISSN 1434-7636. doi: 10.1007/s10035-015-0559-z.

[53] K. L. Lee and H. B. Seed. Drained strength characteristics of sands. *Journal of the Soil Mechanics and Foundations Division*, 93(6):117–141, 1967.

[54] K. L. Lee, H. B. Seed, and P. Dunlop. Effect of moisture on the strength of a clean sand. *Journal of the Soil Mechanics and Foundations Division*, 93(SM6):17–40, 1967.

[55] G. A. Leonards and A. G. Altschaeffl. Discussion. *Journal of the Soil Mechanics and Foundations Division*, 97(SM1):269–271, 1971.

[56] L. K. Li, Z. J. Wang, S. H. Liu, and E. Bauer. Calibration and performance of two different constitutive models for rockfill materials. *Water Science and Engineering*, 9(3):227–239, 2016. doi: https://doi.org/10.1016/j.wse.2016.11.005.

[57] J. Lin, W. Wu, and R. I. Borja. Micropolar hypoplasticity for persistent shear band in heterogeneous granular materials. *Computer Methods in Applied Mechanics and Engineering*, 289:24–43, 2015. doi: 10.1016/j.cma.2015.02.005.

[58] S. López-Querol and M. R. Coop. Drained cyclic behaviour of loose Dogs Bay sand. *Géotechnique*, 62(4):281–289, 2012. doi: 10.1680/geot.8.P.105.

[59] D. Mašín. A hypoplastic constitutive model for clays. *International Journal for Numerical and Analytical Methods in Geomechanics*, 29(4):311–336, 2005. doi: 10.1002/nag.416.

[60] G. R. McDowell, M. D. Bolton, and D. Robertson. The fractal crushing of granular materials. *Journal of the Mechanics and Physics of Solids*, 44(12):2079–2101, 1996. doi: https://doi.org/10.1016/S0022-5096(96)00058-0.

[61] G. Medicus. *Barodesy and its application for clay*. Phd thesis, Universität Innsbruck, Innsbruck, 2014.

[62] G. Medicus, W. Fellin, and D. Kolymbas. Barodesy for clay. *Géotechnique Letters*, 2(4):173–180, 2012. doi: 10.1680/geolett.12.00037.

[63] G. Mesri and B. Vardhanabhuti. Compression of granular materials. *Canadian Geotechnical Journal*, 46(4):369–392, 2009. doi: 10.1139/T08-123.

[64] N. Miura and T. Yamanouchi. Effect of water on the behavior of a quartz-rich sand under high stresses. *Soils and Foundations*, 15(4):23–34, 1975. doi: 10.3208/sandf1972.15.4_23.

[65] D. Muir Wood. *Soil behaviour and critical state soil mechanics*. Cambridge University Press, 1991.

[66] D. Muir Wood. *Soil Mechanics: a one-dimensional introduction*. Cambridge University Press, 2009. ISBN 978-0-521-51773-7.

[67] W. Mun and J. S. McCartney. Roles of particle breakage and drainage in the isotropic compression of sand to high pressures. *Journal of Geotechnical and Geoenvironmental Engineering*, 143(10):04017071–14, 2017. doi: 10.1061/(ASCE)GT.1943-5606.0001770.

[68] Y. Nakata, Y. Kato, M. Hyodo, A. F. L. Hyde, and H. Murata. One-dimensional compression behaviour of uniformly graded sand related to single particle crushing strength. *Soils and Foundations*, 41(2):39–51, 2001. doi: 10.3208/sandf.41.2_39.

[69] A. Niemunis and I. Herle. Hypoplastic model for cohesionless soils with elastic strain range. *Mechanics of Cohesive-frictional Materials*, 2(4):279–299, 1997. doi: 10.1002/(SICI)1099-1484(199710)2:4<279::AID-CFM29>3.0.CO;2-8.

[70] E. S. Nobari and J. M. Duncan. *Effect of reservoir filling on stresses and movements in earth and rockfill dams: a report of an investigation*. Number 186 pages in Contract report - U.S. Army Engineer Waterways Experiment Station ;S-72-2. Waterways Experiment Station, Vicksburg, Miss., 1972.

[71] L. A. Oldecop and E. E. Alonso. A model for rockfill compressibility. *Géotechnique*, 51(2):127–139, 2001. doi: 10.1680/geot.2001.51.2.127.

[72] L. A. Oldecop and E. E. Alonso. Theoretical investigation of the time-dependent behaviour of rockfill. *Géotechnique*, 57(3):289–301, 2007. doi: 10.1680/geot.2007.57.3.289.

[73] C. Ovalle. *Contribution à l'étude de la rupture des grains dans les matériaux granulaires*. Phd thesis, Ecole Centrale de Nantes, Nantes, 2013.

[74] C. Ovalle, C. Dano, P. Y. Hicher, and M. Cisternas. Experimental framework for evaluating the mechanical behavior of dry and wet crushable granular materials based on the particle breakage ratio. *Canadian Geotechnical Journal*, 52(5):587–598, 2015. doi: 10.1139/cgj-2014-0079.

[75] C. Peng, X. G. Guo, W. Wu, and Y. Q. Wang. Unified modelling of granular media with Smoothed Particle Hydrodynamics. *Acta Geotechnica*, 11(6):1231–1247, 2016. doi: 10.1007/s11440-016-0496-y.

[76] J. M. Pestana and A. J. Whittle. Compression model for cohesionless soils. *Géotechnique*, 45(4):611–631, 1995. doi: 10.1680/geot.1995.45.4.611.

[77] N. T. V. Phuong, A. Rohe, R. B. J. Brinkgreve, and A. F. van Tol. Hypoplastic model for crushable sand. *Soils and Foundations*, 58(3):615–626, 2018. doi: https://doi.org/10.1016/j.sandf.2018.02.022.

[78] K. H. Roscoe, A. N. Schofield, and C. P. Wroth. On the yielding of soils. *Géotechnique*, 8(1):22–53, 1958. doi: 10.1680/geot.1958.8.1.22.

[79] A. Sadrekarimi and S. M. Olson. Critical state friction angle of sands. *Géotechnique*, 61(9):771–783, 2011. doi: 10.1680/geot.9.P.090.

[80] J. H. Schmertmann. The mechanical aging of soils. *Journal of Geotechnical Engineering*, 117(9):1288–1330, 1991. doi: 10.1061/(ASCE)0733-9410(1991)117:9(1288).

[81] A. Schofield and P. Wroth. *Critical state soil mechanics*. McGraw-Hill, London, 1968.

[82] G. F. Sowers, R. C. Williams, and T. S. Wallace. Compressibility of broken rock and the settlement. In *Proceedings of the 6th International Conference on Soil Mechanics and Foundation Engineering*, volume 2, pages 561–565, Montreal, 1965.

[83] J. Tejchman and E. Bauer. Numerical simulation of shear band formation with a polar hypoplastic constitutive model. *Computers and Geotechnics*, 19(3):221–244, 1996. doi: https://doi.org/10.1016/0266-352X(96)00004-3.

[84] J. Tejchman and W. Wu. Numerical simulation of shear band formation with a hypoplastic constitutive model. *Computers and Geotechnics*, 18(1):71–84, 1996. doi: https://doi.org/10.1016/0266-352X(95)00018-6.

[85] K. Terzaghi. *Erdbaumechanik auf bodenphysikalischer Grundlage*. Leipzig and Wien, 1925.

[86] K. Terzaghi, R. B. Peck, and G. Mesri. *Soil mechanics in engineering practice*. Wiley, London, 3rd edition, 1996.

[87] C. Truesdell and W. Noll. The non-linear field theories of mechanics. In S. Flügge, editor, *Encyclopedia of Physics*, volume III. Springer-Verlag Berlin Heidelberg, 1965. ISBN 978-3-642-46017-3.

[88] A. S. Vesić and G. W. Clough. Behavior of granular materials under high stresses. *Journal of the Soil Mechanics and Foundations Division*, 94(3):661–688, 1968.

[89] P.-A. von Wolffersdorff. A hypoplastic relation for granular materials with a predefined limit state surface. *Mechanics of Cohesive-frictional Materials*, 1(3):251–271. doi: 10.1002/(SICI)1099-1484(199607)1:3<251::AID-CFM13>3.0.CO;2-3.

[90] C. C. Wang. A new representation theorem for isotropic functions: An answer to Professor G. F. Smith's criticism of my papers on representations for isotropic functions. *Archive for Rational Mechanics and Analysis*, 36(3):166–197, January 1970. ISSN 1432-0673. doi: 10.1007/BF00272241.

[91] S. Wang. *Numerical simulation of soil creep with hypoplasticity*. Phd thesis, Universität für Bodenkultur Wien, Vienna, 2017.

[92] S. Wang, W. Wu, C. Peng, X. Z. He, and D. S. Cui. Numerical integration and FE implementation of a hypoplastic constitutive model. *Acta Geotechnica*, 13(6): 1265–1281, 2018. doi: 10.1007/s11440-018-0684-z.

[93] S. Wang, W. Wu, Z. Y. Yin, C. Peng, and X. Z. He. Modelling the time-dependent behaviour of granular material with hypoplasticity. *International Journal for Numerical and Analytical Methods in Geomechanics*, 42(12):1331–1345, 2018. doi: 10.1002/nag.2793.

[94] X. T. Wang. *An updated hypoplastic model, its implementation and its application in tunnelling*. Phd thesis, Universität für Bodenkultur Wien, Vienna, 2009.

[95] W. Wu. *Hypoplastizität als mathematisches Modell zum mechanischen Verhalten granularer Stoffe*. Phd thesis, Institut für Bodenmechanik und Felsmechanik der Universität Fridericiana in Karlsruhe, Karlsruhe, 1992.

[96] W. Wu and E. Bauer. A hypoplastic model for barotropy and pyknotropy of granular soils. In D. Kolymbas, editor, *Modern approaches to plasticity*, pages 225–245, Amsterdam, 1993. Elsevier Science.

[97] W. Wu and E. Bauer. A simple hypoplastic constitutive model for sand. *International Journal for Numerical and Analytical Methods in Geomechanics*, 18(12): 833–862, 1994. doi: 10.1002/nag.1610181203.

[98] W. Wu and D. Kolymbas. *Hypoplasticity then and now*, pages 57–105. Springer Berlin Heidelberg, Berlin, Heidelberg, 2000. ISBN 978-3-642-57018-6.

[99] G. F. Xu, W. Wu, and J. L. Qi. Modeling the viscous behavior of frozen soil with hypoplasticity. *International Journal for Numerical and Analytical Methods in Geomechanics*, 40(15):2061–2075, 2016. doi: 10.1002/nag.2516.

[100] J. A. Yamamuro, P. A. Bopp, and P. V. Lade. One-dimensional compression of sands at high pressures. *Journal of Geotechnical Engineering*, 122(2):147–154, 1996. doi: 10.1061/(ASCE)0733-9410(1996)122:2(147).